

ABSTRACT

Title of Document: INTERACTION OF LASERS WITH ATOMIC CLUSTERS AND STRUCTURED PLASMAS

John Patrick Palaastro, Ph. D, 2007

Directed By: Professor Thomas M. Antonsen Jr., Physics

We examine the interaction of intense, short laser pulses with atomic clusters and structured plasmas, namely preformed plasma channels. In examining the laser pulse interaction with atomic clusters we focus on the optical response of an individual cluster when irradiated by a laser. Our analysis of the laser pulse interaction with plasma channels focuses on the mode structure of a laser pulse propagating within the channel. We then present a novel application of these channels: quasi-phased match acceleration of electrons.

The optical properties of a gas of laser pulse exploded clusters are determined by the time-evolving polarizabilities of individual clusters. In turn, the polarizability of an individual cluster is determined by the time evolution of individual electrons within the cluster's electrostatic potential. We calculate the linear cluster polarizability using the Vlasov equation. A quasi-static equilibrium is calculated from a bi-maxwellian distribution that models both the hot and cold electrons, using inputs from a particle-in-cell simulation [Taguchi, T. *et al.*, Phys. Rev. Lett., 2004.

92(20)]. We then perturb the system to first order in field and integrate the response of individual electrons to the self consistent field following unperturbed orbits. The dipole spectrum depicts strong absorption at frequencies much smaller than $\omega_p/\sqrt{2}$. This enhanced absorption results from a beating of the laser field with electron orbital motion.

The properties of pulse propagation within plasma are determined by the structure of the plasma. The preformed plasma channel provides a guiding structure for laser pulses unbound by the intensity thresholds of standard wave guides. In particular, the corrugated plasma channel [Layer *et al.* Phys. Rev. Lett. (2007)] allows for the guiding of subluminal spatial harmonics. These spatial harmonics can be phase matched to high energy electrons, making the corrugated plasma channel ideal for the acceleration of electrons. We present a simple analytic model of pulse propagation in a corrugated plasma channel and examine the laser-electron beam interaction. Simulations show accelerating gradients of several hundred MeV/cm for laser powers much lower than required by standard laser wakefield schemes.

INTERACTION OF LASERS WITH ATOMIC CLUSTERS AND STRUCTURED
PLASMAS

By

John Patrick Palastro

Dissertation submitted to the Faculty of the Graduate School of the
University of Maryland, College Park, in partial fulfillment
of the requirements for the degree of
Doctor of Philosophy
2007

Advisory Committee:

Professor Thomas M. Antonsen Jr., Chair
Senior Research Scientist Parvez Guzdar
Professor Adil Hassam
Assistant Professor Thomas Murphy
Professor Patrick O'Shea

© Copyright by
John Palastro
2007

Dedication

Dedicated to my parents.

Acknowledgements

I'd like to acknowledge anyone who might be offended that I forgot to acknowledge them in the following text; I acknowledge that I can be forgetful.

Throughout the time I spent in his group, Professor Antonsen has had the patience to deal with me through both successful and unsuccessful projects—no easy task, especially during the unsuccessful projects. At times it really seemed odd that he was paying me, and not the other way around. He provided guidance, knowledge, and technique, and I repayed him with factor of 2 errors, coding bugs, and noise dominated results; I jest. His door was always open and he was always willing to help me sort through my harebrained ideas, and for this I am grateful.

Howard Milchberg deserves acknowledgement for reminding me that physics is really an experimental science. He was always willing to discuss new ideas and potential experiments, and provided physical insight where I would often overlook it.

I'd like to thank my committee for taking the time out of their busy schedules to read this dissertation and listen to my defense: Parvez Guzdar, Adil Hassam, Thomas Murphy, and Patrick O'Shea.

The entire staff of the physics department and IREAP deserves praise for making graduate school as smooth as possible in spite of the daunting bureaucracy behind it all. In particular, I'd like to mention Jane Hessian, Linda O'Hara, Mohini Kaul, Janice Shoonover, and Nancy Boone.

As for my colleagues: Jim Cooley provided helpful discussions when I'd be stuck on a problem. Jianzhou Wu would never cease to amaze me with the random bits of wisdom he would impart. Ayush Gupta provided the counterpoint in physics

and life discussions that helped me refine my thinking; I've never enjoyed playing devil's advocate so much. Sepehr Morshed helped me make the transition from my focus on clusters to plasma based accelerators. Both of us starting in a new field, we were able to correct each others mistakes and learn from scratch without feeling self conscious. Andrew York provided the conceptualization that I would often times overlook staring at equations. He was invaluable in getting me to use my physics intuition. Scott Fletcher would always have a plasma physics problem available if I ever got frustrated with what I was working on. These discussions were a great for broadening my knowledge of plasma physics.

I'd like to thank my friends, those I haven't mentioned already, for helping me get through graduate school, listening to me complain, and helping me forget about work when I needed: Erik Gans, Matthew Hoeft, Shawn Mcpoland, Jon Miller, Jon Nett, Jason Ortmeier, Andrew Pomerance, Adam Sefkow, Tommy Willis.

And last but not least, my family deserves mention, of course, for their loving support: my parents for reminding me that I needed to get out of school eventually and that I wasn't making any money. It sounds sarcastic, I realize, but it really was a motivating factor. And my sister and brother-in-law for actually being interested in what I was doing.

Table of Contents

Dedication.....	ii
Acknowledgements.....	iii
Table of Contents.....	v
List of Figures.....	vi
1 Introduction.....	1
1.1 From Gas to Clusters to Guiding Plasma Structures.....	1
1.2 Applications of Clustered Plasmas and Plasma Channels.....	4
1.3 Characterization of a Laser-Plasma System.....	9
1.4 Summary of Research.....	11
1.4.1 Summary of Cluster Research.....	12
1.4.2 Summary of Plasma Channel and Electron Acceleration Research.....	15
2 Dielectric Properties of Laser Exploded Clusters.....	21
2.1 Introduction.....	21
2.2 Equilibrium Configuration.....	27
2.3 Linear Perturbation.....	32
2.3.1 Linear System.....	32
2.3.2 Trajectories.....	34
2.3.3 Algorithm.....	36
2.4 Results.....	39
2.4.1 Cold Cluster Limit.....	40
2.4.2 Sharp Ion Profile with Single Temperature Electrons.....	42
2.4.3 Diffuse Ions with Simple Temperature Electrons.....	47
2.4.4 Linear Cluster Polarizability Throughout Evolution.....	49
2.5 Summary and Conclusions.....	51
2.6 Appendix: Temperature Dependence of RMS Orbital Radius.....	53
3 Pulse Propagation and Electron Acceleration in Corrugated Plasma Channels.....	68
3.1 Introduction.....	68
3.2 Laser Pulse Propagation in the Corrugated Plasma Waveguide.....	73
3.3 Scaling Law and Comparison to Other Schemes.....	78
3.4 Beam Dynamics.....	82
3.4.1 Equations of Motion.....	82
3.4.2 Scaling Law Validation.....	84
3.4.3 Transverse Dynamics.....	89
3.4.4 Space Charge Estimation.....	95
3.5 Summary and Conclusions.....	97
3.6 Appendix.....	100
3.6.1 Non-Linear and Relativistic Plasma Effects.....	100
3.6.2 Pulse Power Leakage from Plasma Channel.....	104
3.6.3 Unstable Spot Size Oscillations.....	106
4 Summary and Conclusions.....	120
Bibliography.....	123

List of Figures

Fig 2.1 Comparison of electron density extracted from the PIC simulation (dotted line) and the result of our equilibrium calculation with parameters (T_c, T_h) and (n_c, n_h) extracted from the PIC simulation (solid line) on the left axis. The inset shows the same comparison on a vertical log-scale. The corresponding electrostatic potential is plotted on the right scale.

Fig 2.1 Three sample electron trajectories. The cluster radius here is 19 nm.

Fig 2.3 The two ion charge density profiles extracted from a PIC code for use in our calculation. The sharp ion density profile (solid) has a very steep gradient at the cluster boundary. The diffuse ion density profile (dotted) trails off smoothly as it approaches the calculation boundary.

Fig 2.4 Comparison of the real (top graphs) and imaginary (bottom graphs) components of the polarizability spectra from our time-domain kinetic calculation (solid line) and frequency domain fluid calculation (dotted line). A small temperature, $T_e=51$ eV, was used in the kinetic calculation. (a) A smoothing factor of $n = .0057w_p(0)$ is used; (b) the smoothing factor is $n = .057w_p(0)$.

Fig 2.5 Comparison of the imaginary component of the polarizability spectra from our time-domain kinetic calculation with frozen particles (solid line), and frequency domain fluid calculation (dotted line). In both cases a smoothing factor of $n = .0057w_p(0)$ is used. The number of electrons used was 2^7 and the grid spacing was reduced by a factor 5 to eliminate noise associated with fixed particle location.

Fig 2.6 Real, Fig. 2.6(a), and imaginary, Fig. 2.6(b), polarizability spectra resulting from the sharp ion profile. Each spectrum has a vertical offset of $20(a^2/2)$ and corresponds to a different electron temperature as labeled on the right. The arrow demarcates where a cold-cluster dielectric resonance would be expected.

Fig 2.7 Contours of electron radial (left) and angular (right) frequencies in the energy-angular momentum plane. 800 nm represents a contour level of 0.11. The top graphs are at 1.3 keV and the bottoms graphs at 26 keV. The equilibrium distribution function is plotted on the left to elucidate where the electrons are concentrated.

Fig 2.8 Resonant electron bands in the energy-angular momentum plane for the sharp ion profile and $T_e=1.3$ keV. (a) Bands determined by the condition $w = nw_r - w_q \pm .02w_p$, where w corresponds to a wavelength of 800 nm.

The width $.02w_p$ is chosen for illustrative purposes. (b) Bands determined by the condition $w = nw_r + w_q \pm .02w_p$, where $w = v/c$. The speckles are a numerical artifact.

Fig 2.9 Real, Fig. 2.9(a), and imaginary, Fig. 2.9(b), polarizability spectra resulting from the diffuse ion profile. Each spectrum has a vertical offset of $20(a^2/2)$ and corresponds to a different electron temperature as labeled on the right. The arrow demarcates where a cold-cluster dielectric resonance would be expected.

Fig 2.10 Resonant electron bands in the energy-angular momentum plane for the diffuse ion profile with $T_e=1.3$ keV. (a) Bands determined by the condition $w = nw_r - w_q \pm .02w_p$, where $w = v/c$ corresponds to a wavelength of 800 nm. The width $.02w_p$ is chosen for illustrative purposes. (b) Bands determined by the condition $w = nw_r + w_q \pm .02w_p$, where $w = v/c$. The speckles are a numerical artifact.

Fig 2.11 Comparison of the imaginary component of the polarizability resulting from the sharp (dotted) and diffuse (solid) ion profile at two different temperatures. The top picture has $T_e=1.3$ keV and the bottom $T_e=26$ keV.

Fig 2.12 (a) On the left axis, the intensity profile (solid) used in irradiating the cluster in the PIC simulation. On the right axis (log scale), hot and cold electron temperatures extracted from the PIC simulation as a function of time (dotted) right axis. (b) On the left axis (log scale), the fraction of hot electrons extracted from the PIC simulation as a function of time (solid). On the right axis, the RMS electron radius of the cluster (dotted).

Fig 2.13 Real, Fig. 2.13(a), and imaginary, Fig. 2.13(b), polarizability spectra at different times through the cluster evolution as labeled on the right. Each spectrum has a vertical offset of $10(a^2/2)$. The spectra were smoothed by a factor $n = .018w_p$. The arrow demarcates where a cold-cluster dielectric resonance would be expected.

Fig 3.1 Proposed setup for direct acceleration of electrons by a femtosecond laser pulse in a corrugated plasma waveguide. 3.1(a) A radially-modulated Nd:YAG laser pulse focused by an axicon onto a gas jet creates a spark several centimeters long with micron-scale structure. The spark expands into Fig 3.1(b) a plasma waveguide with axial modulations, allowing fine velocity control of guided radiation [15]. Fig 3.1(c) A radially polarized femtosecond laser pulse and a relativistic electron beam are injected into this waveguide.

Fig 3.2(a) The relative amplitude of the spatial harmonics as a function of the phase modulation amplitude. Fig 3.2(b) The phase velocity for different spatial harmonics as a function of modulation wavelength. Fig3.2(c) The local laser phase

velocity as a function of axial distance. Fig3.2(d) Energy contribution of different spatial harmonics for an electron initially phase matched to the $n = 1$ spatial harmonic.

Fig 3.3 Comparison of energy gain predicted by our scaling law with numerical results obtained by integrating the fully relativistic electron equations of motion. Fig3.3(a) The slow wave phase velocity is matched to the initial electron velocity; Fig3.3(b) the slow wave velocity is set to c .

Fig 3.4 Electron axial momentum distributions for different initial electron beam widths after 1.8 cm of propagation (the extent of a physical plasma waveguide).

Fig 3.5 Comparison of electron beam Gaussian widths with axial field profile.

Fig 3.6 Schematic of the transverse forces for small radii as a function of axial distance. The arrows represent the magnitude of the radial force. Because electrons are distributed uniformly in the axial direction, the quasi-phase matched force and ponderomotive force add to provide an overall focusing of the electron beam for small radii.

Fig 3.7 Averaged final (after 1.8 cm of propagation) axial momentum (color scale) as a function of initial position (x_o, z_o) .

Fig 3.8 Averaged final (after 1.8 cm of propagation) axial momentum (color scale) as a function of final position (z_f, x_f) , (the axial distance traveled by the leading electron has been subtracted out).

Fig 3.9 Final electron density as a function of final position (z_f, x_f) . The electrons are accelerated into the slow wave fronts resulting in bunching.

Fig 3.10 The envelope of the transverse vector potential propagating in the axially modulated channel at different times in a frame moving at c . Results were obtained using the WAKE simulation [74].

Fig 3.11(a) A sample density profile allowing for one quasi-bound mode and also limiting the loss of pulse power to outgoing waves. Solutions to Eq. (44) for our model density profile in Eq. (45) accurately represent the show density profile. Fig 3.11(b) k_{\perp}^2 corresponding to the density profile shown in Fig 3.11(a).

Introduction

1.1 From Gas to Clusters to Guiding Plasma Structures

When high pressure gas passes through a nozzle it rapidly expands and cools and begins to form atomic aggregates called clusters [1]. These aggregates, held together by the inter-atomic van der Waal's forces, consist of hundreds to millions of atoms. Locally each cluster is at solid density, but the average atomic density is the same as a tenuous gas. The local solid density of the clusters allows efficient absorption of laser light, while the low average density allows for long pulse propagation distances before the pulse energy has been depleted [2]. This makes the clustered gas ideal for forming an initial background plasma.

After the clusters have been formed, a high intensity short laser pulse irradiates the clustered gas. This interaction will be the focus of section 2. The clusters are field ionized in the leading edge of the pulse [3]; these seed electrons then result in a cascading collisional ionization of the cluster. Once ionized, the cluster electrons begin to absorb energy through a collisionless process described in section 2 [4-7]. The high energy electrons then begin to expand and pull the ions along with them via their electrostatic attraction. Eventually the individual cluster plasma has expanded into its neighbors, the local nature of the clusters is lost, and a background plasma has formed.

The formation of the background plasma from the cluster gas depends on the properties of the initial irradiating pulse. In initial experiments the heating pulse

simply passed through the clustered gas, resulting in a non-uniform heating profile along the propagation axis due to diffraction, ionization induced refraction, and energy depletion of the pulse in the plasma [3,8,9]. In later experiments an axicon lens was placed in front of the heating laser before the pulse entered the plasma channel [10]. The axicon, which projects the radial intensity profile of the laser onto the propagation axis, allowed for a uniform axial heating profile of the clustered gas.

Both experiments used the radial variation of the intensity profile to generate a differential ionization and heating profile across (transverse to the propagation direction) the clustered gas. The clusters towards the center of the laser path were ionized and heated more effectively. Specifically, an intensity dependent heating threshold for clusters (discussed in section 2) results in a substantial difference in the heating at the center of the laser spot than at the periphery [4-6]. As the clusters disassemble, the background plasma has a hot, dense core and a cooler, low density periphery. The plasma then undergoes hydrodynamic expansion and a shock wave propagates radially outward from the center of the plasma [11]. The expansion results in a channeled plasma structure with a density depression at the center—the preformed plasma channel.

The density depression at the center of the plasma provides a negative radial gradient in the index of refraction of the plasma. Light refracts off of regions of low index of refraction (high plasma density), and thus the preformed plasma channel can be used to overcome the natural diffraction of laser pulses in uniform dielectric media. This process is similar to standard metallic waveguides in which the dielectric constant in the center of the waveguide is smaller than the effective dielectric

constant of the metallic conducting walls (the dielectric constant at a perfectly conducting wall is effectively negative infinity). In addition to its potential for limiting diffraction, the plasma waveguide is not intensity limited by dielectric breakdown as with metal. These properties make the plasma waveguide a natural dielectric medium for guiding high intensity laser pulses over large distances ($\sim 1 \text{ cm}$) [11-13].

The demonstration of guiding in the axial uniform plasma waveguide has generated studies and creation of more complex plasma guiding structures [14,15]. Here the focus is on the axially modulated plasma waveguide [15]. In creating the axially modulated plasma waveguide the heating laser, before passing through the axicon, passes through a diffractive optic, which imposes radial modulations onto the intensity profile. The axicon then projects the radial modulations onto the propagation axis resulting in an axially periodic heating of the clustered gas. The resulting plasma structure has an axially periodic index of refraction, while maintaining the guiding properties as before. The periodic index of refraction of the plasma channel provides the guided laser with a novel property: spatial oscillations of the local phase velocity. Applications of the axially modulated channel will be discussed in section 1.2, while guiding in this structure and the application to electron acceleration will be discussed in section 3.

Before the advent of atomic clusters, plasma channel formation schemes used gas for formation of the background plasma [11]. The gas density required for efficient collisional ionization far exceeds the average clustered gas density required [8,10]; the local solid density of clusters allows for efficient collisional ionization.

Clustered gases thus allow for the formation of channels at much lower minimum electron densities: $1 \times 10^{18} \text{ cm}^{-3}$ compared to $5 \times 10^{18} \text{ cm}^{-3}$ for unclustered gas [10]. The importance of low minimum electron densities is discussed in section 1.2. In addition the inefficient absorption of energy by tenuous gas and plasma required the use of long pulse, high energy lasers for channel formation: $\sim 300 \text{ mJ}$ compared to $\sim 30 \text{ mJ}$ for clustered gas [10]. In fact, clusters absorb less energy in the presence of long pulses [6,10].

1.2 Applications of Clustered Plasmas and Plasma Channels

Both the clustered plasma and plasma channel provide unique dielectric media that have the potential for use in a variety of applications. Clustered plasmas have been demonstrated as a source of high harmonic conversion, x-rays, high energy ions and fusion neutrons as well as providing self-focusing and spectral wavenumber shifts [6,17-30]. For high harmonic conversion in clusters, electrons bound to the ions via the anharmonic electrostatic potential are driven at the laser frequency [16-18]. This driving gives rise to dipole radiation of the cluster at harmonics of the laser frequency. The radiating frequency is steady throughout the evolution of the cluster, as the driven electrons oscillate at harmonics of the driving frequency. The amplitude of the radiation changes, however, as it is determined by the properties of the electrostatic potential.

X-rays are primarily generated via three processes in clusters: photorecombination, dielectronic recombination, and impact induced spontaneous emission [19,20]. In photorecombination an electron becomes recaptured by an ion

and emits its excess energy as a photon. The x-ray power emitted via this process tends to be small especially after electron temperatures surpass atomic binding energies [21]; high energy electrons move too fast to be recaptured by the ions. Dielectronic recombination occurs when an electron is recaptured by an ion and the excess energy promotes a bound electron to an excited state. In a second step, the excited state then undergoes radiative decay, emitting an x-ray. In impact induced emission x-rays are generated from the spontaneous emission of an ion that had been excited from a lower state via electron impact. The amount of power emitted into x-rays via dielectronic recombination and impact induced emission, the two dominant emission processes, depends on the cluster size [20].

During the disintegration of a cluster, the ions can gain enough kinetic energy to overcome the nuclear force, allowing for fusion reactions (especially for hydrogen clusters) [6,22,23]. Depending on the cluster parameters, two mechanisms result in ion energies required for fusion. Coulomb explosion occurs when the laser is able to rapidly strip the cluster of a large portion of its electrons, the remaining ions then explode due to their own space-charge repulsion [24,25]. All of the electrostatic energy from the large charge imbalance is transferred to ion kinetic energy. During the quasi-neutral cluster expansion, electrons are resonantly heated via a collisionless absorption process (described in section 2) [4]. The electrons then expand while at the same time transferring their energy to the ions via their coulombic attraction. At some radius the electron and ion charge are equal; the electric field (acceleration) is at a maximum. If this electric field is large enough, the ions at this radius can be accelerated past the layer of ions in front of them. This results in a high energy

outward expanding shell of ions [6]. The fusion reaction takes place when a high energy shell of ions from the expansion of one cluster intersects the ion shell of a neighboring cluster. High energy neutrons are created in the process.

Self focusing in clusters arises from the differential heating of clusters from the radial intensity profile of the laser pulse [6]. Clusters close to the peak of the laser heat and expand faster than those on the periphery. The clusters close to towards the center of the laser, thus, have a larger radius, generating a larger dielectric constant (as we will see in section 2). The negative gradient in the dielectric constant provides the self-focusing. The expansion of the clusters also results in the spectral redshift of the clusters as the dielectric constant increases as the cluster's effective radius increases [26].

The guiding properties of plasma channels allows for long interaction lengths required for high-intensity short pulse applications. The plasma channel has already been examined and used for laser-wakefield acceleration, and has been proposed for use in x-ray generation for x-ray lasers, terahertz (THZ) generation, and direct electron acceleration [31-39]. In laser wakefield acceleration, a ultrahigh intensity laser propagates down a preformed plasma channel. The large electric field amplitude of the laser provides a ponderomotive force that expels electrons from the path of the laser pulse. (The ponderomotive force acts as an effective pressure, pushing charged particles from regions of high field to low field). Behind the pulse, the electrons, having been displaced, undergo plasma oscillations. The corresponding electrostatic field can then accelerate a relativistic beam of electrons along its phase fronts. The plasma channel removes the diffractive limitation on the length of the

accelerating structure, providing a higher energy electron beam. Furthermore, the phase velocity of the plasma wave is equal to the group velocity of the displacing laser. If the plasma density is too high, the group velocity may be too low to result in phase matching between the plasma wave and electron beam over desired acceleration distances. Use of the clustered gas for formation of the background plasma results in lower plasma densities (higher group velocities) and may be useful in extending the interaction length.

For x-ray laser schemes, a low intensity pulse is guided through a preformed plasma channel that has not been fully ionized [37]. The guided modes intensity is low enough that the average ionization level of the preformed channel remains constant. The plasma channel electrons gain energy from the pulse through inverse bremsstrahlung heating, in which an electron gains energy when passing through the electric field due to an ion. The heated electrons then pump excited states of the neutral atoms by transferring energy to the atoms during collisions. An initial spontaneously emitted photon causes the stimulated emission of an excited atom which in turn causes yet another stimulated emission and so on. The atoms are continually pumped and depleted in this manner, resulting in the coherent production of x-rays. Use of a plasma channel allows for efficient absorption of the guided pulse without diffraction limitations as well as guiding the x-rays throughout the gain process.

The properties of an axially periodic plasma channel can be used to convert energy from the guided laser into THZ radiation modes [38]. The lowest frequency of the plasma waveguide is determined by the plasma density of the channel. For

generation of low frequency modes (i.e. THZ), low density plasma channels are required, making clustered plasmas an ideal formation media. To generate THZ radiation, a guided laser drives ponderomotive currents in the corrugated plasma channel. The current propagates with the laser pulse at the group velocity, which in a plasma channel is strictly subluminal. In an uncorrugated guiding structure the current cannot efficiently generate radiation due to the strictly super-luminal phase velocity; phase matching between the current and the waveguide modes cannot be achieved. In the corrugated waveguide the periodicity of the structure results in a shift to the wave number of the waveguide modes, allowing for subluminal phase velocities. The radiation and current can then be phase matched and efficient conversion of power from the laser into THZ radiation is possible.

The application of corrugated plasma channels to direct acceleration of electrons will be examined in detail in section 3. To accelerate electrons, a high intensity short laser pulse copropagates with a high energy electron beam down a preformed plasma channel. In axially uniform channels, phase slippage from the electron beam's subluminal velocity and the guided mode's superluminal phase velocity limits acceleration over arbitrary distances. In axial periodic channels, the guided mode acquires a periodic phase modulation. This phase modulation is equivalent to the guided mode being composed of several spatial harmonics each with their own phase velocity. With the right choice of laser beam and plasma parameters, the phase velocity of a spatial harmonic can be subluminal. This allows for quasi-phase matching between the electron beam and guided mode, greatly extending the interaction length. Because the electron beam copropagates with the pulse, a

reduction in the group velocity can also extend the interaction length, increasing the energy gain of the electron beam. Reduction of the group velocity requires lower electron densities, which again makes clusters an ideal medium for channel formation.

1.3 Characterization of a Laser-Plasma System

The study of laser-plasma interactions spans a wide range of both plasma and laser parameters. The subset of this parameter space our laser and plasma belong to determines how to proceed analyzing the system. Typically a laser-plasma system of interest can be well characterized by the ratio of the laser frequency to the plasma frequency, the ratio of the laser wavelength to the size of the plasma, and the laser intensity. Parameters such as collision frequency, plasma temperature, and pulse length do, however, play a role in the interaction, but are not fundamental to the interaction.

The ratio of the plasma frequency, defined as $\omega_p = \sqrt{4\pi e^2 n / m}$ where e is the unit of charge for our plasma specie, n is the density of that specie, and m is the mass of that specie, to the laser frequency, ω , determines how well the electric field of the laser can penetrate the plasma. For a tenuous plasma, $\omega_p / \omega \ll 1$, and the laser can propagate freely with only a slight adjustment to its wavelength. In this situation the plasma behaves as a poor conductor and is unable to respond quickly enough to neutralize the electric field. However, if the laser pulse encounters a region of dense plasma $\omega_p / \omega \gg 1$ it separates into a reflected pulse and an evanescent pulse that is

absorbed in a small region, $\sim c/\omega_p$, at the plasma surface. The dense plasma acts as good conductor and is able to rapidly shield the incoming electric field.

The ratio of the laser wavelength, λ , to the plasma size, a , determines the importance of magnetic fields in considering the dispersion of the laser. For small plasma systems, $a/\lambda \ll 1$, and the magnetic field can be neglected. Over large distances the laser may propagate as an electromagnetic wave, but on the scale of the plasma it is essentially uniform. The near uniformity of the laser electric field results in a small magnetic field through Faraday's law, providing an essentially electrostatic plasma response. When the plasma system is large, $a/\lambda \gg 1$, the laser behaves strictly as an electromagnetic wave.

The laser intensity determines the role of ionization, the energy scale, and dynamics of the plasma. For low intensity lasers $I \approx 1 \times 10^{14} \text{ W/cm}^2$ if the plasma is not pre-ionized, ionization dynamics must be considered. For dense plasmas, ionization can deplete the pulse energy and lead to refraction of the laser as the dielectric contribution from gas and plasma compete. Also for low intensities the magnetic contribution of the Lorentz force can be neglected (if the plasma temperature is subrelativistic); the plasma current is determined solely by local oscillations in the laser electric field. (The response may not be local, however, in the presence of sharp density interfaces.) In the high intensity regime $I \approx 1 \times 10^{16} \text{ W/cm}^2$ ionization only affects the leading edge of the pulse and the energy lost via ionization is generally small enough to be neglected. The plasma is still non-relativistic, but the electric field strength is large enough to produce a non-linear force on the plasma: the ponderomotive force. The force, which results from fast oscillations across electric

field gradients, is time independent in the frame of the laser pulse and pushes plasma from regions of high electric field into regions of low electric field. For ultra-high intensity lasers $I \approx 1 \times 10^{18} \text{ W / cm}^2$ the velocity of the plasma particles as they oscillate in the local electric field can approach c . In this situation the magnetic field must be accounted for and the plasma must be treated relativistically. The force on the plasma particles becomes highly non-linear and the motion complex.

Here the focus is on the interaction of high intensity, $\sim 1 \times 10^{16} \text{ W / cm}^2$, short pulse $\sim 100 \text{ fs}$ lasers with two types of plasmas: ionized atomic clusters and preformed plasma channels. The interaction of the laser with these two types of dielectric media takes place on two disparate frequency and size scales. The central plasma frequency of an ionized cluster ($2 \times 10^{16} \text{ Rad Hz}$) exceeds the laser frequency ($2 \times 10^{15} \text{ Rad Hz}$) and the radius of a typical atomic cluster (10 nm) is much smaller than a typical laser wavelength (800 nm). On the other hand, the plasma frequency of the plasma channel ($2 \times 10^{14} \text{ Rad Hz}$) is everywhere smaller than the laser frequency, and the features ($10 \mu\text{m}$) on the plasma channel are larger than the laser wavelength.

1.4 Summary of Research

This dissertation is divided into two sections. The first section will discuss the dielectric properties of laser exploded clusters; the second section discusses the propagation of lasers and acceleration of electrons in a corrugated plasma waveguide.

1.4.1 Summary of Cluster Research

An ionized cluster consists of an ion core surrounded by electrons. The electrons are bound to the ion core via their electrostatic attraction and orbit the ion core. The shape of the electrostatic potential well, and hence the electron motion, depend on the cluster's charge imbalance and the electron temperature, both of which change as the cluster evolves. When the electrons are displaced by an external force, in this case an applied laser electric field, the cluster behaves like a dipole oscillator. The cluster has a natural dipole oscillation frequency, $\omega = \omega_p / \sqrt{2}$, associated with the bulk response of the electrons to the laser field. Due to the high electron density (nearly solid) of the cluster this frequency is much larger than typical laser frequencies ($\lambda \sim 800\text{nm}$). Here we develop a model of the laser-cluster dipole interaction and demonstrate that the cluster does in fact respond at its natural oscillation frequency. More importantly, we find that cluster has a dipole response at much lower frequencies comparable to actual laser frequencies. This low frequency response is due to a beating of the laser field with the electron orbital motion. We also find that the spectral shift, amplitude, and spectral width of the natural and low frequency dipole response are temperature dependent.

The linear polarizability spectra for a cluster at different temperatures and at different times throughout its evolution are found. The coupled two dimensional (2D) Vlasov-Poisson system of equations is used. The Vlasov equation determines the evolution of the phase space distribution of the cluster plasma, while the Poisson equation determines the cluster's electrostatic potential. To lowest order, the cluster is assumed to be in a circularly symmetric quasi-static equilibrium consisting of two

electron species at different temperatures (hot and cold) and ions. The equilibrium electron distribution function is determined from the equilibrium Vlasov equation and is dependent on the two electron temperatures, the cluster's electrostatic potential, the fraction of electrons at each temperature, and the total electron charge. The cluster ions are assumed to have zero velocity; their inertia makes them essentially immovable on the time scale of the electron motion. The electron temperature, charge imbalance, two temperatures, and ion density profile are extracted from a PIC simulation [4]. The Poisson equation is then solved to find the cluster's equilibrium electrostatic potential.

The Vlasov equation is then linearized to first order in the electric field to find the cluster's dipole response. The electric field perturbation represents the presence of a linearly polarized laser electric field; the cluster is in the electrostatic limit and the magnetic field can be ignored. This provides two coupled integro-differential equations that determine the first order electron distribution function and first order correction to the cluster's electrostatic field. The electron density corresponding to the first order field correction provides the cluster's dipole moment.

A df algorithm is used to solve the integro-differential equation numerically [39]. Specifically, the evolution of the electron distribution function is determined by an ensemble average of equilibrium electron orbits integrated through the first order potential. Numerically each electron represents a region of 4D phase space (two velocity, two spatial) weighted by the value of equilibrium distribution function determined by its initial condition. At each time step the distribution function provides the electron density, which is used to find the first order potential which then

is used to determine the distribution function at the next time step. The time dependent dipole moment is found from the electron density at each time step. At the end of the calculation, the time dependent dipole moment is Fourier transformed to provide the polarizability spectrum. The perturbing electric field is applied as an impulse so that the entire linear frequency response of the specified cluster equilibrium can be recovered in one simulation.

Three types of cluster equilibrium are explored. The first equilibrium consisted of a uniform ion core; the polarizability structure as a function of temperature is examined. The uniform ion core represents an assembled cluster and was extracted from the PIC simulation before passage of the laser pulse [4]. Exploring the temperature dependence is somewhat artificial (the electron temperature for a given equilibrium is fixed) and is only used to provide insight into the polarizability structure. It is found that the cluster responds at the dielectric resonant frequency predicted by cold plasma theory—the collective electron dipole oscillation of the cluster. The cluster also responds at lower frequencies not predicted by cold plasma theory. The low frequency response results from the beating of electron orbital motion with the laser frequency, and provides a collisionless heating mechanism for the cluster. This response is of interest because it occurs at frequencies comparable to actual laser frequencies. The low frequency response grows in amplitude as the temperature is increased; more electrons can reach regions of high electric field outside the cluster with increasing temperature. The dielectric resonant frequency drops in amplitude with increasing temperature due to a more diffuse electron density profile.

The second equilibrium explored is a diffuse ion profile extracted 300 fs after passage of the laser pulse. For the diffuse ion profile, the standard dielectric response is not nearly as prominent, and the low frequency response drops in amplitude as the temperature is increased. The absence of a strong standard dielectric response is a direct result of the diffuse charge; the cluster vacuum-interface is no longer a well defined boundary. The drop in low frequency response with increasing temperature arises from the electrons with large radii orbits experiencing a reduced electric field outside the cluster due to the diffuse charge profile.

The linear polarizability at different times throughout the cluster evolution was also explored, using temporally local equilibrium determined from the PIC simulation [4]. The standard dielectric resonance is found to have a non-monotonic, time dependent spectral shift due to the interplay between warm plasma dispersion and diffusivity of the ion and electron density profiles as the cluster expands. The resonant peak is also shown to significantly broaden due to the expansion of the density profile as the cluster heats. The low frequency response increases in amplitude throughout the cluster evolution as the fraction and energy of hot electrons increases as the cluster becomes heated by the laser.

1.4.1 Summary of Plasma Channel and Electron Acceleration Research

Preformed plasma channels provide a guiding structure for laser pulses without the intensity limitations of standard waveguides—a property required by a variety of applications. In particular, it has been proposed by Serafim *et al.* [40] that an electron beam can be accelerated by a laser guided in a preformed plasma channel.

The energy gain of electrons is severely limited, however, by the fact that the phase velocity of the guided laser pulse is always greater than c in plasma and thus always greater than the electron beam velocity. Here we show that this limitation can be overcome if the plasma channel has axial periodic density modulations like those produced by Layer *et al.*[15]. We examine the propagation of a laser pulse in the axially modulated plasma channel, and show that the guided pulse is composed of spatial Fourier harmonics due to the presence of the axial corrugations. For the right channel and laser parameters, the spatial Fourier harmonics can have phase velocities smaller than c and equal to the electron beam velocity, allowing for phase matching. We find that, for the same parameters, our acceleration scheme provides energy gains several orders of magnitude higher than previously proposed schemes. The focusing and defocusing of the electron beam due to the laser electromagnetic field is also explored.

The propagation of a radially polarized laser pulse and direct acceleration of electrons in corrugated plasma channels is explored. The propagation of the pulse is modeled using the slowly varying envelope equation. This approximation to the wave equation assumes that variations in the laser's envelope occur on time scales much longer than the laser period. In the case of plasma channels, this assumption is valid when the plasma frequency is much smaller than the laser frequency. The slowly varying envelope equation neglects terms in the wave equation contributing to group velocity dispersion (GVD). One effect of GVD, integral to electron acceleration, is the subluminal group velocity. This effect is explicitly accounted for by replacing c , the speed of light, by c_g , the group velocity, in the wave equation.

The response of the background plasma is treated in the linear non-relativistic regime; the plasma responds only to the local oscillations of the laser electric field. A plasma density profile is used that models the experimentally created channels [15], and also allows for analytic solutions to the slowly varying envelope equation. The plasma profile consists of a constant background density that is axially modulated in addition to a quadratic radial dependence. In the case where the radial profile is also modulated, oscillation of the laser spot size can become unstable and leakage from the channel may become important (the model density profile may no longer valid) [41]. The monotonic nature of the model density profile precludes side leakage of laser power from the channel. The ramifications of this approximation are examined using WKB theory for a simplified leaky channel.

An analytic solution for the field structure of the guided mode in the corrugated plasma channel is found. The field is found to have a wavenumber shift due to the presence of the background plasma and the finite spot size of the laser. In addition the field obtains a periodic phase modulation due to the presence of the axially periodic density profile. The periodic phase modulation is viewed as a sum of spatial harmonics each with their own relative amplitude and phase velocity. For all but the fundamental laser spatial harmonic, it is found that subluminal phase velocities (slow waves) are realizable for density modulation periods commensurate with experimental results [15].

In treating the background plasma in the linear non-relativistic limit, the pondermotive force of the laser on the background plasma is ignored. This non-linear effect, which can lead to Raman scattering, can degrade the quality of the laser

pulse during propagation. It was previously suggested that small angle Raman side scattering can be suppressed through use of leaky plasma channels [42]. Electric field non-linearities and non-slowly varying effects can also lead to Raman forward scattering. Here the WAKE simulation is used to demonstrate that Raman forward scattering has a negligible effect on the laser pulse, and that the stable propagation is due to the low amplitude of the laser field, not the presence of axial structure.

With the analytic solution for the laser field, a scaling law for the energy gain for a direct accelerated electron beam is derived. In finding the scaling law, the beam is assumed to start at nearly c on axis with zero transverse momentum. The electron beam is phase matched to the largest amplitude spatial harmonic of the laser that can support a subluminal phase velocity (this is referred to as quasi-phase matching). The maximum time for energy gain is set to the pulse length dephasing time (duration it takes an electron at c to outrun the laser). The scaling law predicts, for the same parameters, energy gains several orders of magnitude higher than previously proposed acceleration schemes [43-45].

To validate the scaling law and examine electron dynamics, the fully relativistic electron equations of motion are integrated in the presence of the guided mode's electromagnetic field. The transverse and longitudinal space charge fields of the electron beam are neglected. Expressions are derived for upper limits on the beam density that determine when the transverse and longitudinal space charge fields become non-negligible.

For high initial electron energies, $\mathbf{g}_o = 1000$ where \mathbf{g}_o is the relativistic factor, the energy gain of ideal electron orbits from the simulations is shown to agree well

with theoretical predictions. For low energies, $g_o = 30$, the electron energy oscillates due to phasing and dephasing with the electric field. At intermediate energies, $g_o = 100$, for parameters corresponding to experiment, it is found that allowing electrons to catch up to the slow wave results in higher energies than starting the electron phase matched to the slow wave. A simple Hamiltonian model capturing this effect is presented.

The final axial momentum distribution functions are examined for different initial Gaussian electron beam widths. When all the electrons start on axis, the distribution function displays a high energy peak at the theoretically expected energy gain. It is found, however, that increasing the electron beam radius leads to an increasing degradation of this peak; it nearly disappears for realistic beam widths. This effect is shown to be the result of transverse electron dynamics, and not the drop off of the accelerating field for increased radius.

Two forces are identified as contributors to the electron's transverse dynamics: the focusing/defocusing force of the quasi-phase matched spatial harmonic and the ponderomotive force due to the phase mismatched fundamental laser mode. The transverse quasi-phase matched force is phase dependent; at relativistic velocities an equal number of electrons are focused as defocused. The ponderomotive force to the fundamental laser mode, which tends to be smaller in amplitude, is phase dependent and provides an overall focusing of the entire electron beam for small radii. In addition, the quasi-phase matched force is 90° out of phase with accelerating field; electrons in the maximum accelerating phase feel little transverse force.

The electron beam is found to undergo a net outward radial flow as it propagates with the pulse. Electrons initially in the defocusing phase are pushed outward until they reach a radius where the ponderomotive force is directed outward. The increased outward force causes these electrons to be expelled from the beam. Some electrons initially in the focusing phase will eventually slip into the defocusing phase and undergo the same process. It is proposed that smaller electron beam radii may reduce this effect at the expense of accelerating gradient.

Section 2: Dielectric Properties of Laser Exploded Clusters

2.1 Introduction

A cluster is an aggregate of 10^2 - 10^7 atoms held together by van der Waals forces. Clusters form when high pressure gas passes through a nozzle, and the gas undergoes rapid expansion and cooling [1]. A gas of clusters makes an ideal system for coupling energy from a laser field to the cluster gas medium, while allowing long propagation distances [2]. This is because the laser matter interaction occurs at the local solid density of the cluster, yielding strong absorption, while the average density of the medium is low, allowing for propagation. This energy coupling has led to the experimental observation of several unique optical properties, such as x-ray generation, harmonic conversion, and self-focusing [16-18, 26-28]. Laser irradiated cluster gases have been considered as a source of these phenomena in a variety of applications, including medical imaging, plasma based accelerators, and radiation sources [8,46,47]. The laser intensities required for use of these applications can couple so much energy to an individual cluster that it explodes. Exploding clusters have, thus, been explored extensively in the past decade.

A gas of exploding clusters represents a novel, time dependent, nonlinear optical medium [26]. The processes of harmonic generation [17,18], spectral wavenumber shifts [26], and self focusing [27] have all been shown to occur in cluster gases. The optical properties of the cluster gas are characterized by the polarization density $\vec{P} = 4\mathbf{p}n_{cl} \langle \vec{p} \rangle$, where n_{cl} is the number density of clusters and

$\langle \bar{p} \rangle$ represents the local ensemble average of the dipole moments of the individual clusters. Here we assume that the cluster radius is smaller than the radiation wavelengths of interest and that the cluster density is low enough such that the inter-cluster spacing is much greater than the cluster radius and, as a result, interaction between clusters occurs through the mean field. The explosion of the clusters occurs on a time scale determined by the inertia of the ions, while the dipole moment is determined mainly by the rapid motion of the cluster electrons. It is thus possible to characterize the dipole moment in terms of a frequency dependent polarizability $\mathbf{g}(\mathbf{w}, t)$ that evolves slowly in time. Here the local Fourier transforms of the laser electric field and the dipole moment are related by $\bar{p} = \mathbf{g}(\mathbf{w}, t) \bar{E}$. We then define the bulk dielectric constant for a gas of clusters as the sum total of individual cluster contributions.

$$\mathbf{e}_{bulk} = 1 + 4\mathbf{p}n_{cl} \langle \mathbf{g}(\mathbf{w}) \rangle. \quad (1)$$

The bulk dielectric constant provides the connection to the macroscopic phenomena that can determine how best to utilize the cluster in the aforementioned applications.

The simplest model that can be used to describe the cluster polarizability is that of a uniform density, cold plasma [48]. In this case the cluster can be characterized as a sphere of radius a with local dielectric constant $\mathbf{e} = 1 - \mathbf{w}_p^2 / \mathbf{w}(\mathbf{w} - i\mathbf{n})$, where $\mathbf{w}_p^2 = 4\mathbf{p}e^2n_e / m_e$, n_e is the electron density, e is the unit of charge, \mathbf{n} is the electron-ion collision frequency, and m_e is the electron mass. In the presence of an external field, $\bar{E}(t) = \text{Re}[E(t)e^{i\mathbf{q}}] \hat{x}$, one can determine the potential outside the cluster ($r > a$) to be [49]

$$\bar{f}_1(r, \mathbf{q}, \boldsymbol{\omega}) = -\text{Re} \left[\left(r + \frac{a^3 \mathbf{e}(\boldsymbol{\omega}) - 1}{r^2 \mathbf{e}(\boldsymbol{\omega}) + 2} \right) \bar{E}(\boldsymbol{\omega}) e^{i\mathbf{q}} \right] \quad (2)$$

where the over-line on f_1 and E denotes a temporal Fourier transform. The polarizability of the cluster is defined as the ratio of dipole moment to the electric field. This ratio can be extracted from the dependence of potential on radius as given in Eq. (2). In particular, the portion of the potential that varies as r^{-2} gives

$$\mathbf{g}(\boldsymbol{\omega}) = a^3 \left(\frac{\mathbf{e}(\boldsymbol{\omega}) - 1}{\mathbf{e}(\boldsymbol{\omega}) + 2} \right). \quad (3)$$

If we substitute the cold plasma dielectric constant into Eq. (3), and neglect for the moment collisions, we find that the cluster has a dielectric resonance when

$\boldsymbol{\omega} = \boldsymbol{\omega}_p / \sqrt{3}$ [48]. This resonance can be excited by a laser field of prescribed frequency in two ways during the course of cluster heating and explosion. First, as the cluster atoms are being ionized, the electron density will rise in time and pass through the resonance before the cluster has had a chance to expand. Since the cluster atoms are initially at solid density, the electron density quickly exceeds the critical density by a large margin, $\boldsymbol{\omega}_p \approx 10\boldsymbol{\omega}$. Second, after the cluster has been heated, and expands, the radius will increase and the density will drop. If the cluster remains a solid, uniform sphere it will pass again through a resonance as it expands. With collisions included, the resonance acquires a nonzero width. However, for predicted values of the collision rate the resonance is narrow enough that strong heating would only be observed for a short duration of time. In experiments, it is observed that heating occurs throughout the laser pulse and thus, the uniform density model needs to be modified so as to be consistent with experiments. In addition to

the excitation of the cluster resonance by the laser heating pulse at frequency ω , the cluster resonance can be excited by nonlinear signals at harmonics of ω [17,18,50]. Thus, general knowledge of the frequency dependent polarizability is of interest [51].

It is worth noting that the uniform density model makes two significant simplifying assumptions: uniform ion density, and zero electron temperature. The first approximation results in a simple analytic formula for the dipole moment due to the uniformity of the dielectric constant within the cluster. However, the assumption of a sharp boundary results in a polarizability that in the absence of collisions is real except for a narrow range of frequencies around the resonance. Consequently, according to this model absorption only occurs during a brief time when the cluster is in resonance. This simplification was corrected by a fully hydrodynamic model of the cluster that was introduced by Milchberg [52]. The model was the first to introduce spatial variation in the cluster ion density, but assumed the electrons responded to the laser as a cold fluid. This model coupled a 1D Lagrangian fluid code to a laser field governed by $\nabla \cdot \mathbf{e}(r, t) \vec{E} = 0$. Here the dielectric constant is modeled as $\epsilon(r) = 1 - \omega_p^2(r) / \omega(\omega - i\eta(r)) + \Lambda(r)$, where $\epsilon(r)$ contains the dielectric response of the neutral cluster atoms. The radial variation in the ion density profile and dielectric constant allows for continuous absorption of laser energy at the location of the plasma resonance, $\omega \sim \omega_p(r, t)$. Thus, a cluster can absorb energy throughout the laser pulse, up until the time that the maximum cluster electron density is below the critical density. We note that the uniform density model is still useful, and that agreement between the uniform density model and the nonuniform density

calculations can be achieved by artificially increasing the collision frequency and decreasing the ion mass in the uniform density model [3].

The second approximation made in the uniform dielectric model is that the plasma is cold. Consequently, the cluster electron response to the internal electric field is local in space. While this may be a good approximation initially, as the cluster heats up it is likely to fail. Furthermore, for sufficiently large laser intensities, $\sim 1 \times 10^{15}$ W/cm², a population of energetic electrons is produced. These electrons have sufficiently high speed such that they travel a distance comparable to the cluster size in one laser period. Their response to the internal field is necessarily nonlocal, and cannot be described accurately by a fluid theory.

Kinetic treatments of cluster explosion require solving for individual electron trajectories. Several particle-in-cell (PIC) simulations have been developed to model the interaction of clusters with intense laser pulses. Many of these simulations have focused on clusters irradiated with very high laser intensities, on the order of 10^{17} W/cm². In this regime most of the electrons are expelled from the cluster core early in the laser pulse [25]. The cluster expansion then manifests as an ion core explosion due to its own space-charge repulsion. Here we will mainly discuss a more moderate intensity regime, 10^{15} - 10^{17} W/cm², paralleling the results of the PIC code developed by Taguchi *et al.* [4].

Simulations conducted by Taguchi *et al.* [4] and Gupta *et al.* [3] indicate that the cluster can resonantly absorb energy through an electron transit time resonance. These simulations show an absorption process related to that proposed by Brunel for the case of sharp density gradients [53]. Electrons are extracted from the cluster by

the laser electric field. The emission of these electrons is limited by their space charge potential. In the next half of the cycle, the laser field switches direction, and the extracted electrons are accelerated back towards the cluster by both the space-charge and laser field. The electrons then return to the cluster core having gained energy from the field.

Within the cluster the electric field remains small because it is shielded by the large dielectric response of the overdense plasma. The electrons then pass through the cluster and can emerge in phase with the laser. If when passing through the cluster, the electrons maintain the proper phase with respect to the field, they can continue to be accelerated to very high energies. A simple scaling argument shows that a critical intensity exists for the onset of the transit time resonance:

$$I^4 / D^2 = (\pi c / 2) (m_e c^2 / e)^2 = 1.36 \times 10^{10} \text{ W},$$

where D is the cluster diameter, λ is the laser wavelength and I the laser intensity. PIC simulations demonstrate that the heating process leads to a two-temperature electron distribution function [5]. The energetic electrons have orbits that lie primarily in a low density halo that surrounds the cluster core. The response of these ‘halo’ electrons is important in determining the cluster polarizability.

While PIC codes in principle provide a complete description of the cluster explosion process, including the generation of an oscillating dipole moment in response to the applied laser electric field, they do not lend themselves to calculating the propagation of a laser pulse through a gas of clusters. To understand the propagation through a gas of exploding clusters it is useful to have an expression for or tabulation of the dielectric constant of the gas that is of the form of Eq. (1). The

goal of this section is to present calculations of the frequency dependent cluster polarizability $\mathbf{g}(\mathbf{w},t)$ that includes the effects of non-uniform cluster density and energetic cluster electrons, and would be useful to the study of laser propagation. Our approach will be to assume that the ion density profile is fixed and that the cluster electrons are in a quasi-equilibrium state. We will then perform a linear perturbation analysis of this state to obtain the frequency dependent polarizability. More specifically, the cluster will be described by the coupled Vlasov-Poisson system. Parameters that determine the equilibrium configuration will be taken from the results of a PIC simulation, and the resulting equilibrium electron density and electrostatic potential will be compared with the PIC results.

In Sections 2.2 and 2.3 we present our kinetic model of the equilibrium cluster system and perturbation to that system, respectively. Section 2.2 also includes a discussion of the algorithm used in solving our kinetic model for the cluster polarizability. In Section 2.4 we present the results of our kinetic calculation. Polarizabilities from an assembled ion core with varying electron temperature, diffuse ion profile with varying electron temperature, and polarizabilities at different times during the cluster evolution with the equilibrium determined by our PIC simulation [4] are presented. Section 2.5 contains our conclusions.

2.2 Equilibrium Configuration

To examine the interaction of the two populations of electrons with the laser field we invoke a coupled 2-D Vlasov-Poisson system of equations. We consider the problem in two dimensions rather than three so that a) we can directly compare

results with our PIC modeling which is primarily two-dimensional and b) the resulting integrals are simplified. The system can be expressed as:

$$\frac{\partial f_s}{\partial t} + \bar{v} \cdot \bar{\nabla} f_s - \frac{q_s}{m_s} \bar{\nabla} \mathbf{f} \cdot \frac{\partial f_s}{\partial \bar{v}} = 0, \quad (4)$$

and

$$\nabla^2 \mathbf{f} = 4\mathbf{p} \sum_s q_s \int f_s d^2v, \quad (5)$$

where \mathbf{f} is the electrostatic potential, $f_s = f_s(\bar{x}, \bar{v}, t)$ is the distribution function for a specie s , q_s is the charge of that specie, and m_s the mass. For the clusters under consideration the wavelength (λ) of the laser electric field is much longer than the cluster radius (a), and thus the cluster response can be treated in the electrostatic limit ($a/\lambda \ll 1$). In this case the connection between the system, Eqs. (4) and (5), and the time dependent laser electric field is made through the application of the boundary condition to Eq. (5) that the gradient of \mathbf{f} match to a uniform electric field as $|\bar{x}| \rightarrow \infty$.

We imagine the system can be described as two parts: a circularly symmetric equilibrium, and a self-consistent dipole response to the perturbing laser electric field, $\bar{E}(t) = \text{Re}[E_r(t)e^{iq}] \hat{x}$. The total potential and electron distribution function are written as the sum of their equilibrium and perturbed contributions.

$$\mathbf{f}(r, \mathbf{q}, t) = \mathbf{f}_o(r) + \text{Re}[\mathbf{f}_1(r, t)e^{iq}], \quad (6)$$

and

$$f_e(r, \mathbf{q}, \bar{v}, t) = f_o(r, \bar{v}) + \text{Re}[f_1(r, \bar{v}, t)e^{iq}]. \quad (7)$$

Here, f_o and f_1 are the equilibrium quantities, while f_{o1} and f_{l1} are self consistent responses to the perturbing laser electric field. The equilibrium quantities are considered to be independent of time on the time scale of the laser period. The time variation in the perturbed quantities arises from the cluster's response to the perturbing laser electric field. The angular dependence in the perturbed quantities ensures that the total perturbed electric field, $E_1 = -\nabla f_1$, matches the perturbing electric field, $\bar{E}(t)$, for large $|\bar{x}|$.

The ions are treated as a fixed distribution of charge due to their relatively large inertia. The distribution function is taken to be cold with a spatial density $n_{ion}(r)$.

$$f_{ion}(r, \bar{v}) = n_{ion}(r) \mathbf{d}^2(\bar{v}). \quad (8)$$

In effect, we are specifying the ion density profile, which is assumed to be fixed. Our subsequent analysis thus focuses on the electrons.

We first consider the circularly symmetric equilibrium. Substitution of Eqs. (6) and (7) into Eq. (4), and keeping only lowest order terms in the potential, yields:

$$\bar{v} \cdot \bar{\nabla} f_o - \frac{q}{m} \bar{\nabla} f_o \cdot \frac{\partial f_o}{\partial \bar{v}} = 0, \quad (9)$$

for the equilibrium electron distribution function. The formal solution to Eq. (9) allows that f_o can be any function of the constants of motion: in this case, the equilibrium energy and angular momentum. Electron distributions from PIC simulations show that the distributions functions are well characterized by an isotropic bi-Maxwellian distribution [5]. To capture this effect, we include two independent electron populations distinguished by their densities at zero potential

(n_c, n_h) and their temperatures (T_c, T_h) . The equilibrium electron distribution function is then

$$f_o(r, v) = \frac{n_c m}{2\mathbf{p}T_c} e^{-H_o/T_c} + \frac{n_h m}{2\mathbf{p}T_h} e^{-H_o/T_h}, \text{ for } \mathbf{f}_o(0) < H_o < 0, \quad (10)$$

where $H_o = H_o(r, v) = mv^2/2 + q\mathbf{f}_o(r)$ is the total energy of an electron in the equilibrium potential. Here the subscript c refers to the low temperature core electrons, which are mostly shielded from the laser field, and the subscript h to the hot electrons which are more directly exposed to the laser field. The distribution function is taken to be zero for energies greater than zero, and we assume the equilibrium potential vanishes at the calculation boundary. We are, therefore, only considering particles that are confined to the equilibrium potential.

Substituting the equilibrium distribution functions Eqs. (8) and (10) into the equilibrium version of the Poisson equation (5) we obtain

$$\nabla_r^2 \mathbf{f}_o(r) = -4\mathbf{p}[q_i n_{ion}(r) - n_c e^{q_e \mathbf{f}_o(r)/T_c} - n_h e^{q_e \mathbf{f}_o(r)/T_h}]. \quad (11)$$

where q_i and q_e are ion and electron charge respectively. Here we have neglected the corrections to the density due to the distribution function cutoff at zero energy. The correction tends to be small as for most clusters the depth of the equilibrium potential well $\mathbf{f}_o(0)$ tends to far exceed the typical temperatures.

The equilibrium quantities are independent of θ , and thus the derivative of \mathbf{f}_o is set to zero at the origin. This also ensures that the potential is deepest at the cluster center. As already mentioned, the potential \mathbf{f}_o is set to zero at the computational boundary ($r = L$). The equilibrium electric field, $E_o = -\nabla \mathbf{f}_o$, is fixed at the boundary by maintaining a charge imbalance defined by

$$\int_0^L [(1-\mathbf{a})Zn_{ion}(r) - n_c(r) - n_h(r)] \mathcal{H}^2 r \simeq 0, \quad (12)$$

where $0 < \mathbf{a} < 1$, is chosen to best match the results from our PIC simulation for the parameters used in generating Fig. 2.1, unless otherwise stated. For all other calculations, the imbalance was fixed as the temperature varied. For a given T_c and T_h , then, we determine the values of n_c and n_h by the condition above for the charge imbalance and by setting the desired fraction of hot electrons. Equations (6-8) and the above conditions provide a closed set of equations for describing the equilibrium cluster plasma.

Figure 2.1 shows the equilibrium potential, on the right vertical axis, and electron density, on the left vertical axis, calculated from our model (solid) for a 38 nm cluster. The ion density was extracted from the PIC simulation of Taguchi *et al.* at 300 fs [4]. The applied field in the PIC simulation was a 100 fs full width at half maximum Gaussian pulse with a wavelength of 800 nm, and intensity of 5×10^{15} W/cm². By 125 fs after the peak of the laser pulse, the heated electrons consisted of two species one at $T_c=300$ eV and the other at $T_h=6.4$ keV, which contributed 10% of the total electron population. For comparison the electron density from the PIC code has been plotted (dotted). The agreement between the PIC density and that of our model extends to even the halo region. The inset shows the electron density for both on a log scale. As mentioned, the potential depth exceeds the value of the temperature. The good agreement seen here shows that it is reasonable to model the equilibrium as being stationary on time scales short compared with the expansion time of the ions. Our analysis of the perturbations of this equilibrium are contained in the next section.

2.3 Linear Perturbation

We now consider the linear response of the cluster to a finite duration laser electric field $\vec{E}(t) = \text{Re}[E_r(t)e^{iq}] \hat{x}$ imposed at the system boundary. The imposed laser field drives a time dependent perturbation in the cluster potential. This results in the electron density changing to shield out the laser field from the cluster core. The cluster continues to evolve self consistently in this manner under the time evolution of the laser field.

2.3.1. Linear System

The equation describing the time evolution of the first order distribution function for electrons is found by substitution of Eqs. (6) and (7) into Eq. (4) and linearizing. We find that:

$$\frac{df_1}{dt} - q[\bar{v}(t) \cdot \nabla f_1(r, \mathbf{q}, t)] \frac{df_o}{dE} = 0 . \quad (13)$$

Here the time derivative is taken following equilibrium electron orbits, and thus $\bar{v}(t)$ is understood to be the motion resulting from the equilibrium potential, ϕ_o . The first order potential is the solution to the Poisson equation with the first order density as the source.

$$\nabla^2 f_1(r, \mathbf{q}, t) = -4\pi q \int d^3v f_1(r, \mathbf{q}, \vec{v}, t) . \quad (14)$$

The system boundary ($r = L$) is far enough away that the cluster will appear as a dipole oscillator, with the x-component of the dipole moment, p_x , defined as

$$p_x(t) = \int_0^{2p} \int_0^L r \cos(\mathbf{q}) n_1(r, \mathbf{q}, t) d^2r, \quad (15)$$

where n_1 is the first order electron density perturbation. For large r , the general electrostatic potential due to a dipole can be written $\mathbf{f}_1(r, \mathbf{q}, t) = \text{Re}[\mathbf{f}_1(r, t)e^{iq}]$, where $\mathbf{f}_1(r, t)$ satisfies

$$\mathbf{f}_1(r, t) = -rE_r(t) + \frac{p(t)}{r}. \quad (16)$$

We eliminate the unknown quantity $p(t)$ by differentiating Eq. (16) with respect to r , and combining the result with (16), arriving at our condition on the potential at the simulation boundary.

$$\left[\frac{d\mathbf{f}_1(r, t)}{dr} + \frac{\mathbf{f}_1(r, t)}{r} \right] \Big|_{r=L} = -2E_r(t). \quad (17)$$

In addition we require $\mathbf{f}_1(r=0, t) = 0$, which is consistent with the angular dependence e^{iq} .

In frequency space, the dipole moment can be expressed as the linear response of a medium to an electric field:

$$\bar{p}_x(\mathbf{w}) = \bar{\mathbf{g}}(\mathbf{w})\bar{E}_r(\mathbf{w}). \quad (18)$$

where $\bar{\mathbf{g}}$ is the polarizability of the cluster and the overline denotes that the quantities are temporal Fourier transforms. By applying a laser field as an impulse to the cluster at $t=0$, the entire dipole spectrum can be recovered. That is, we apply an impulsive electric field, measure the time dependent dipole response, Fourier transform this response, and form the ratio of $\bar{p}(\mathbf{w})$ to $\bar{E}_r(\mathbf{w})$. For numerical purposes, our applied laser field takes the form:

$$E_r(t) = A_o \frac{t}{2\mathbf{p}} \frac{1}{t^2 + (t/2)^2}, \quad (19)$$

where in the limit that $t \rightarrow 0$, $E_r(t) \rightarrow A_o \mathbf{d}(t)$, and A_o is an arbitrary multiplicative factor. For nonzero values of t , $\bar{E}_r(\mathbf{w}) = A_o \exp[-|\mathbf{w}|t]$ and we include this factor in the calculation of the polarizability. In our calculations we set $\tau \sim .01$ fs.

2.3.2 Trajectories

We now focus on the solution of Eq. (13). Integration of this equation is carried out along the trajectories of electrons in the unperturbed field given in terms of the equilibrium potential. For any electron in our system we can express its equilibrium Hamiltonian as

$$H_o = \frac{p_r^2}{2m} + \frac{\ell^2}{2mr^2} + q\mathbf{f}_o(r), \quad (20)$$

where p_r and ℓ are the radial and angular momentum respectively. The equilibrium Hamiltonian is conserved as it exhibits no explicit time dependence. The potential depends only on radius, and thus the angular momentum of electrons in the equilibrium cluster potential is also conserved. The equation for the radial motion can then be written:

$$\ddot{r} = -\frac{q}{m} \frac{\partial}{\partial r} \mathbf{f}_o + \frac{\ell^2}{m^2 r^3}. \quad (21)$$

These equations represent a central force problem [54].

Electron depletion early in the cluster evolution leaves a net positive charge in the cluster core. An electrostatic potential, ϕ_o , then attracts the electrons. Electrons

with energy less than zero ($f_o(0) < H_o < 0$) are confined to the cluster potential, and thus undergo periodic motion. The electrons, however, have some initial angular momentum, which acts as an additional effective potential [the second term in Eq. (21)]. The effective potential ($\sim 1/r^2$) repels the electrons as they approach the cluster center setting up a minimum orbital radius. The minimum and maximum electron orbital radii are the roots of $H_o - qf_o(r) - \ell^2 / 2mr^2 = 0$. We can define the frequency of electron oscillation between these two radii as the radial bounce frequency, given by

$$\mathbf{w}_r = \mathbf{p} \left[\int_{r_{\min}}^{r_{\max}} m \frac{dr}{p_r} \right]^{-1}, \quad (22)$$

where $p_r(r, H_o, \ell)$ is obtained by solving Eq. (21) with H_o , ℓ , and $r(0)$ given. A rotational frequency can also be defined as the time it takes an electron to rotate by 2 radians:

$$\mathbf{w}_q = \frac{\mathbf{w}_r}{\mathbf{p}} \left[\int_{r_{\min}}^{r_{\max}} dr \frac{m\ell}{p_r r^2} \right]. \quad (23)$$

These frequencies will be important in understanding the interaction between the laser field and the halo electrons. In particular there will be strong interaction when the field frequency equals the sum of integer multiples of the radial and rotational frequencies. This effect can lead to an enhancement in the dipole moment at laser frequencies lower than typical cold plasma resonant dielectric frequency. Figure 2.2 shows three example trajectories of electrons as they revolve around the cluster center.

2.3.3 Algorithm

In order to calculate how the perturbed cluster distribution function, f_1 , and potential, \mathbf{f}_1 , evolve in time, we utilize a \mathbf{df} algorithm [39]. The distribution f_1 is represented as a set of particles that follow in phase space the equilibrium trajectories and have weights that vary in time calculated according to Eq. (13). At every time step the particle contributions to \bar{J}_1 , the first order electron current density, are computed on a radial grid. The e^{iq} dependence of all first order quantities, limits calculations to a radial grid. The quantity \bar{J}_1 is then used to find the perturbed density through the continuity equation, and from the first order density we find the perturbed potential. The potential is then used in Eq. (13) that updates the distribution function. The calculation continues until we reach a maximum time determined by the desired spectral width of the dipole spectrum.

Particles are distributed as follows: N_A particles are initially distributed randomly with a uniform distribution in (x, y) and (v_x, v_y) satisfying $\sqrt{x^2 + y^2} < L$, and $v_x^2 + v_y^2 < v_{\max}^2 = -2q\mathbf{f}(0) / m$. Particles are given equal weight, proportional to the area in velocity space that they represent $\mathbf{p}v_{\max}^2 / N_A$. The particles that satisfy $\mathbf{f}_o(0) < H_o < 0$ are confined by the cluster potential and are tracked, whereas particles with $H_o > 0$ are counted in N_A (to give the correct weighting) but are not tracked. For the rest of this section we will refer to particles that are trapped by the cluster potential and satisfying $\mathbf{f}_o(0) < H_o < 0$ as A particles.

The particles with $H_o > 0$ were included in the equilibrium distribution function, but do not contribute strongly to the equilibrium density. However, the effect of eliminating these particles must be considered in the perturbation because of the infinite gradient in the distribution function at the energy at $E=H_o=0$. To do this, we randomly distribute N_B particles in (x, y) , and set the magnitude of their velocity to be $|v| = \sqrt{2q_e f_o(r) / m_e}$. A random angle, Θ , is then chosen to determine (v_x, v_y) , where $v_x = |v| \cos(\Theta)$ and $v_y = |v| \sin(\Theta)$. These particles lie on the boundary in energy between being trapped by and escaping from the cluster. For the rest of this section we refer to particles with $H_o = 0$, as B particles.

The velocity $\bar{v}(t)$ and position $(r(t), \mathbf{q}(t))$ for each particle is found by solving Hamilton's equations. For ease of calculation, and to overcome the inherent numerical difficulties associated with the $\sim 1/r^2$ effective potential, we solve explicitly for $(x(t), y(t))$ and $(v_x(t), v_y(t))$. The potential $f_o(r)$ is interpolated onto a Cartesian grid $f_o(x, y)$. The Cartesian orbits $(x(t), y(t))$, $(v_x(t), v_y(t))$ are then transformed back to cylindrical coordinates for use in later computation. Particles that reach the calculation boundary are made to undergo specular reflection. The reflection provides an energy clamping to particles that have achieved energies $H_o > 0$ through numerical noise. The reflection should not affect the orbit significantly, as the condition that $f_o(0) < H_o \leq 0$ limits the maximum orbital radius to L , the length of the calculation box.

For A and B particles respectively, the contribution to the first order distribution function [the time integral of Eq. (13)] at each time step is:

$$f_{i,A}(t) = q \int_0^t \bar{v}_i(t') \cdot \nabla \mathbf{f}_1(r_i(t'), t') e^{iq\phi(t')} dt' \frac{df_o}{dE} \Big|_{E=E_i} \quad (24)$$

$$f_{i,B}(t) = -q \int_0^t \bar{v}_i(t') \cdot \nabla \mathbf{f}_1(r_i(t'), t') e^{iq\phi(t')} dt' \frac{f_o(0)}{q\mathbf{f}_o(0)} \quad (25)$$

where the index i distinguishes the particle, and the factor of $\mathbf{f}_o(0)$ in the B particle equation ensures $\int_0^{v_{\max}} f_o(0) d^2v = 1$, and $v_{\max} = \sqrt{2q\mathbf{f}_o(0) / m_e}$. The integrand represents one electron's contribution to electrostatic heating as it moves through the first order potential on its equilibrium trajectory. The integral is then weighted by the likelihood of a particle possessing the equilibrium energy E_i . The total distribution function is then written as the ensemble average of the individual particle contributions:

$$f_1(r, \mathbf{q}, \bar{v}, t) = e^{iq\phi} [N_A^{-1} \sum_{i=1}^{N_A} g_i f_{i,A}(t) + N_B^{-1} \sum_{i=1}^{N_B} g_i f_{i,B}(t)], \quad (26)$$

where the function $g_i = g_i(r - r_i, v - \bar{v}_i)$ determines how each particle's contribution is

distributed in phase space and satisfies $\int_0^{v_{\max}} \int_0^L g_i d^2r d^2v = \mathbf{p} L^2 q \mathbf{f}_o(0) / m_e$. In a similar

manner, we can construct the current density \bar{J}_1 .

$$\bar{J}_1(r, \mathbf{q}, t) = q_e \mathbf{f}_o(0) e^{iq\phi} \left[\sum_{j=A,B} N_j^{-1} \sum_{i=1}^{N_j} \bar{v}_i(t) f_{i,j}(t) h_1(r - r_i) \right], \quad (27)$$

where $q\mathbf{f}_o(0)h_1(r - r_i)$ is the velocity integral of g_i . With the current density specified, the first order potential can be determined. We solve:

$$\nabla^2 \frac{\partial \mathbf{f}_1(r, \mathbf{q}, t)}{\partial t} = 4p\nabla \cdot \bar{\mathbf{J}}_1(r, \mathbf{q}, t) . \quad (28)$$

We use $\bar{\mathbf{J}}_1$ as opposed to the electron density n_1 because this results in a less noisy potential in the low temperature limit. Specifically, in the zero temperature limit the distribution function defined by Eq. (24) appears to diverge due to the factor df_0 / dE . However, the density is finite because of the cancellation of contributions from particles with velocities of equal magnitude but opposite direction. This cancellation is broken at small temperature because of the differing time histories for particles tracing orbits in opposite directions. The difference at small temperature is proportional to the Laplacian of the potential. Thus, correctly calculating the density requires higher order accuracy in radial grid size in calculating the electric field in Eq. (24) than does calculating the current density. Should we want to know the perturbed density we can find it once the potential has been determined. Specifically,

$$n_1(r, \mathbf{q}, t) = \frac{1}{4pe} \nabla^2 \mathbf{f}_1(r, \mathbf{q}, t). \quad (29)$$

The dipole moment $p_x(t)$ is then found by employing Eq. (15). A fast Fourier transform is then used to find $\bar{p}_x(\mathbf{w})$.

2.4 Results

For our studies on the cluster dipole spectrum, we consider a cluster with a 38 nm diameter and an initial center plasma density of $1.4 \times 10^{23} \text{ cm}^{-3}$. The maximum computation radius is set to 80 nm, and we evolve 200,000 particles. We consider two ion density profiles, $n_{ion}(r)$, extracted from the previously mentioned PIC

simulation (Fig. 2.3). The PIC simulation consisted of a 38 nm Argon cluster with a charge state of $Z_i=8$ and an initial center electron plasma density of $1.4 \times 10^{23} \text{ cm}^{-3}$. The cluster was irradiated with an 800 nm wavelength laser pulse of peak intensity $5 \times 10^{15} \text{ W/cm}^2$ and a full width half maximum of 100 fs. The first ion density is taken before passage of the laser pulse, and has a sharp density gradient at the cluster radius. We will refer to this density profile as the sharp ion density profile. The second density occurs at 300 fs, which is 130fs after the peak of the laser pulse. This density profile will be referred to as the diffuse ion density profile. Both of these profiles are plotted in Fig. 2.3. For each density profile, we consider single and dual temperature electron distributions, and examine the variation in the dipole spectra with temperature.

2.4.1 Cold Cluster Limit

To validate the kinetic calculation, we compare the results to a cold fluid calculation of the polarizabilities using the Poisson equation in the frequency domain

$$\nabla \cdot \mathbf{e}(r, \mathbf{w}) \nabla \mathbf{f}_1 = 0 \quad , \quad (30)$$

where $\mathbf{e}(r, \mathbf{w}) = 1 - \mathbf{w}_p^2(r) / \mathbf{w}^2$ and $\mathbf{w}_p^2(r)$ is obtained by solving for the single species electron density at $T_c = 51 \text{ eV}$ in Eq. (11) with the sharp ion density profile. We have set $\epsilon = .006$ in Eq. (12) to achieve the sharpest electron profile cutoff while maintaining the condition $\mathbf{f}_o / \mathbf{f}_o' > \Delta r$, where Δr is the radial step size. A complex frequency with an imaginary component $\text{Im}[\mathbf{w}] = -\mathbf{n}$ was used to smooth the spectrum in both the kinetic and cold fluid cases. In the time domain kinetic case,

smoothing is achieved by multiplying the dipole moment, $p_x(t)$, by the factor $\exp[-\mathbf{n}t]$ before using the FFT to find $\bar{p}_x(\mathbf{w})$. Figure 2.4 shows the resulting cluster polarizabilities normalized to $a^2/2$, the polarizability of a rod of radius a in the limit $\mathbf{e} \rightarrow \infty$. In Fig. 2.4(a) a value of $\mathbf{n} = .0057\mathbf{w}_p(0) = 1.2 \times 10^{14} \text{ Rad/s}$ was used, while in Fig. 2.4(b) $\mathbf{n} = .057\mathbf{w}_p(0) = 1.2 \times 10^{15} \text{ Rad/s}$. From here forward $\mathbf{w}_p = \mathbf{w}_p(0)$ unless otherwise stated.

Figure 2.4(b) shows that at higher damping rates the kinetic and fluid calculations predict the same spectrum with the characteristic resonance at $\mathbf{w}_p / \sqrt{2}$. Figure 2.4(a) shows, however, that even at low temperatures the kinetic model, solid line, has structure not predicted by the cold plasma theory, dotted line. This additional low-temperature structure can result from several effects including finite grid size, finite particle number, and nonzero temperature effects, such as Tonks-Dattner resonances.

To eliminate nonzero temperature effects, we fix $(\bar{x}_i(t), \bar{v}_i(t)) = (\bar{x}_i(0), \bar{v}_i(0))$ in Eq. (24) and otherwise integrate the equations as previously described. Freezing the particle orbits eliminates any cluster response due to finite-temperature. When this is done, we find that the response of the kinetic code is strongly affected by the finite number of particles and finite resolution due to the fact that the particles locations are fixed. In order to minimize this effect we use 2^7 electrons and reduce the spatial step by a factor of 5. Figure 2.5 shows the results compared with the fluid calculation, where in both cases $\mathbf{n} = .0057\mathbf{w}_p = 1.2 \times 10^{14} \text{ Rad/s}$ was used. The results of our

kinetic calculation are in good agreement with the cold-fluid theory, and we can proceed with the kinetic calculation with confidence.

2.4.2 Sharp Ion Profile with Single Temperature Electrons

We first consider the results of the sharp ion profile with a single temperature electron distribution. Again we use an equilibrium charge imbalance factor $\beta = .006$. Figures 2.6(a) and 2.6(b) show the real and imaginary components of the polarizability spectrum resulting from our calculation for electron temperatures ranging from 1.3 keV to 26 keV. The zero line of each spectrum is offset by $20(a^2/2)$. The arrows demarcate where we would expect a resonance in the uniform density, cold cluster approximation.

The dielectric resonance peaks appearing in Fig. 2.6(b) show a temperature dependent red shift from the value of the resonant frequency expected based on the cold plasma, uniform density model. Two effects contribute to this shift: the presence of a diffuse equilibrium electron density profile and the nonzero temperature correction to the electron plasma wave frequency. These effects tend to offset one another. The diffuse profile leads to a lowering of the resonant frequency due to the spatial localization of the mode in the lower density periphery of the cluster, while the nonzero temperature corrections to the plasma wave frequency, at least for small temperatures, tend to increase the resonance frequency. At $T_e=1.3$ keV the spectrum has a redshift of about $.05 \omega_p$; the temperature correction, which we estimate to be $d\omega/\omega_p = 3/(k_d a)^2$, where $k_d = \sqrt{4\pi e^2 n_e / T}$, is insignificant at this temperature and the redshift is due to the diffuse electron density profile. The redshift then decreases

as the temperature correction becomes more prominent, and reaches zero at $T_e=9.7$ keV where the two effects have balanced. The shift then increases again to $.1 \omega_p$ at 26 keV. The increase in temperature has led to an increasingly diffuse electron density (see the Appendix), which begins to overshadow the temperature corrections to the plasma dispersion. Accompanying the shift in frequency of the resonance, there is also a noticeable temperature dependent broadening of the peaks, with an almost indiscernible peak at 13 keV. This broadening is due to the combination of the wave particle resonances that occur for particles orbiting the cluster and the creation of the diffuse electron density profile.

A new feature, an enhancement of both the real and imaginary parts of the polarizability, appears in the spectrum at low frequencies, $\omega \sim .05 \omega_p$ for temperatures greater than 1.3 keV. This enhancement grows larger and extends to higher frequencies as the temperature is increased from 1.3 keV to 26 keV. This low frequency feature is not predicted by the cold plasma approximation. Neither is it explained by assuming the cluster electrons respond adiabatically to the exciting field. To see this we rewrite Eq. (13)

$$\frac{df_1}{dt} = -q \left[\frac{d\mathbf{f}_1}{dt} - \frac{\partial \mathbf{f}_1}{\partial t} \right] \frac{\partial f_o}{\partial E}, \quad (31)$$

and integrate over time assuming a harmonic time dependence for the potential

$$f_1(r, \mathbf{q}, t) = -\text{Re} \left\{ q \left[\mathbf{f}_1(r, t) e^{iq} + i\omega \int_{-\infty}^t \mathbf{f}_1(r(t'), t') e^{iq(t')} dt' \right] \frac{\partial f_o}{\partial E} \right\}, \quad (32)$$

where the integral is taken over an unperturbed orbit (r and θ vary in time due to their evolution in the equilibrium potential ϕ_o). Because θ varies with polar angle as $e^{i\theta}$, the integrand will oscillate rapidly in time as the electrons revolve around the cluster.

As frequency goes to zero the contribution of the integral can then be considered negligible except for particles whose radial and rotation frequencies satisfy the resonance condition

$$\mathbf{w} = n\mathbf{w}_r \pm \mathbf{w}_q, \quad (33)$$

where the radial and angular rotation frequencies are defined in Eqs. (22) and (23), and n is an integer. If we ignore the contribution of these electrons (and the integral) we arrive at the adiabatic approximation. In this approximation the perturbed electron density is given by

$$n_1(r, \mathbf{q}) = \text{Re} \left[k_d^2(r) \mathbf{f}_1(r) e^{iq} \right] \quad (34)$$

where k_d is the inverse Debye length for electrons, with $k_d(r) = \sqrt{4\pi e^2 n_e(r) / T}$, and n_e being the equilibrium electron density profile. As a result, the Poisson equation in this limit becomes

$$[\nabla^2 - \sum_s k_{d,s}^2(r)] \mathbf{f}_1(r) e^{iq} = 0. \quad (35)$$

For the sharp ion profile we can treat the radial dependence of the Debye length as approximately uniform in the cluster $r < a$. We then find the solution for the potential outside the cluster to be

$$\bar{\mathbf{f}}_1(r, \mathbf{q}, \mathbf{w}) = \left[-r + \frac{a^2}{r} \left(\frac{1-\mathbf{y}}{1+\mathbf{y}} \right) \right] \bar{E}_r(\mathbf{w}) e^{iq}, \quad (36)$$

where $0 < \mathbf{y} \equiv I_1(k_d a) / [a k_d I_1'(k_d a)] < 1$. Comparing Eqs. (16) and (36) we find the polarizability to be given by $\mathbf{g} = a^2 (1-\mathbf{y}) / (1+\mathbf{y})$. At low temperatures $k_d a \rightarrow \infty$, $\mathbf{y} \rightarrow 0$ and the polarizability $\mathbf{g} \rightarrow a^2$ the value for high dielectric constant cylinders.

At high temperatures $k_a a \rightarrow 0$, $\mathbf{y} \rightarrow 1$, and the polarizability $\mathbf{g} \rightarrow 0$. Thus, the observed increase in the polarizability cannot be described by the adiabatic approximation.

To explain the additional structure in the polarizability we must consider the second term in Eq. (32), which represents, at low frequency, the contribution to the perturbed density of particles whose equilibrium motion is resonant with the wave frequency. The equilibrium orbits, up to their phases, can be characterized by the energy and the angular momentum H_o and ℓ . In examining how the laser field interacts with electrons with different orbits, a more instructive choice of variables are the frequencies $\mathbf{w}_r(H_o, \ell)$ and $\mathbf{w}_q(H_o, \ell)$ defined in Eqs. (22) and (23). If an electron is driven by the electric field, we expect electrons with frequencies, \mathbf{w}_r and \mathbf{w}_q , satisfying the resonant condition Eq. (33) to respond strongly to the field. The proper electron orbital frequencies must then exist for the laser to excite a strong response. Figure 2.7 shows contours of $\mathbf{w}_q(H_o, \ell)/\mathbf{w}_p$ and $\mathbf{w}_r(H_o, \ell)/\mathbf{w}_p$ in the energy versus angular momentum plane for $T_e=1.3$ keV and $T_e=26$ keV. A laser wavelength of 800 nm corresponds to a contour level of $\mathbf{w}/\mathbf{w}_p = 0.11$. The equilibrium distribution function is plotted on the left to show at which energies electrons are concentrated.

The electron frequencies plotted, at energies in the bulk of the distribution function, have the same order of magnitude as the frequencies of the structure seen in the polarizabilities. Thus, it is reasonable to assume that resonances with these electrons are responsible for the observed structure in the polarizability.

To identify which order of resonance is responsible for a given frequency, we determine what choice of (H_o, ℓ) makes an electron resonant with the laser field. Figures 2.8(a) and 2.8(b) show the resonant electrons bands in energy-angular momentum space for $T_e=1.3$ keV and corresponding to a wavelength of 800 nm and $p/\sqrt{2}$ respectively. Here we have plotted a point for each electron whose indicated combination of radial and angular frequencies comes within a factor of $\sim .02\omega_p$ the corresponding excitation frequency.

At the laser frequency, Fig. 2.8(a), we see only the $n=1$ bounce resonance contributes, while at the dielectric resonant frequency, Fig. 2.8(b), the $n=2$ and $n=3$ bounce resonances both contribute to the polarizability. The $n=2$ and $n=3$ bounces resonances, however, dephase more rapidly with respect to the electric field than the $n=1$ resonance. For an electron slightly off resonance, with a detuning, δ , the phase difference between the electron and applied electric field grows as δnt . The higher n resonances will then contribute less to the polarizability than the $n=1$ resonance.

To understand the increasing amplitude of the low frequency response as a function of temperature, one must consider the work done by the laser field on the orbiting electrons [see Eqs. (23) and (24)]. The work done by the laser field on an electron (labeled with subscript i) in one cycle can be written

$$W = -\frac{q}{m} \int_{\bar{x}_i(t)}^{\bar{x}_i(t+T_L)} \nabla \mathbf{f}_1 \cdot d\mathbf{l}_i \quad , \quad (37)$$

where T_L is the period of the laser. The value of W is determined by both the profile of the perturbed electric field $(-\nabla \mathbf{f}_1)$ and by the range of the electron orbit. The perturbed electric field tends to be small in the core of the cluster where it is shielded

by the high-density plasma, and larger in the halo region surrounding the cluster. Low energy electrons tend to be confined to the core region where the perturbed field is small, while high energy electrons can visit the halo region. The general tendency is that as temperature increases there is an increase in the RMS radius of the electron cloud (shown in the Appendix) corresponding to an increase in the number of electrons visiting the halo region. These electrons experience a stronger perturbed electric field and thus increase the polarizability of the cluster.

2.4.3 Diffuse Ions with Single Temperature Electrons

The polarizability results for the diffuse ion density profile calculations have markedly different properties than those of the sharp ion profile. Figures 2.9(a) and 9(b) show the imaginary and real components of the dipole spectrum respectively in the case of the diffuse density profile. The zero line of each spectrum is offset by $20(a^2/2)$.

The first thing we notice is that the dielectric resonance predicted by the cold cluster approximation has nearly disappeared. The resonance is present, but much less visible than in the sharp density profile case. The red shift decreases from $.1 \rho_p$ at 5.1 keV, to zero at 9.0 keV, and then increases again to about $.2 \rho_p$ at 26 keV. The large red shift of the standard dielectric peak results from a more diffuse electron profile accompanying the diffuse ion profile. As in the sharp case, the redshift gets reduced as the temperature increases from 5.1 keV to 9 keV due to warm plasma dispersion. The redshift then increases again as the temperature increase also results in a more diffuse equilibrium electron density.

The low frequency feature observed in the sharp profile case is also present in the diffuse profile case. At an electron temperature of 1.3 keV the low frequency resonance has developed two prominent absorption peaks. The low frequency response broadens with increasing temperature. This is explained by the increasing population of energetic electrons that have higher orbital frequencies. The decreasing amplitude is a consequence of the interplay between factors contributing to the work done on the electrons Eq. (32). As temperature increases, the RMS orbit size increases as shown in Appendix. This allows more electrons into the halo region where the perturbed field is stronger. However, with higher temperature the shape of the perturbed field is modified; the amplitude becoming reduced in the halo region. The result is that in the diffuse profile case the second factor is stronger and the amplitude of the response drops.

Figures 2.10(a) and 2.10(b) show the resonant bands at 1.3 keV for corresponding to the laser frequency, $(2pc / 800nm)$, and $p/\sqrt{2}$ respectively. With the diffuse ion profile at 800 nm, there are many more electrons resonant with the laser electric field for $n=1$ compared with the sharp ion profile. The large number of electrons resonant with the field also contributes to the relatively large polarizability at low frequencies for the diffuse ion profile. At $p/\sqrt{2}$ there are far fewer resonant electrons for $n=2$ and $n=3$.

To highlight the differences between the single temperature results for each density profile we examine the imaginary component of the dipole spectrum for the sharp ions and diffuse ions with 1.3 keV and 26 keV electrons respectively. Figure 2.11 shows the low frequency absorption peaks and near absence, due to broadening,

of the traditional dielectric resonance for the diffuse profile at 1.3 keV. The sharp ion profile at 1.3 keV exhibits the traditional dielectric peak, albeit red-shifted. At 26 keV the sharp and diffuse ion profiles yield similar results.

2.4.4 Linear Cluster Polarizability Throughout Evolution

We now examine the linear polarizability of a cluster at different times throughout its evolution with parameters described in the beginning of this section. At each time during our PIC simulation we have found the cold and hot electron temperature, fraction of each species, and equilibrium boundary electric field. Figures 2.12(a) shows the cold and hot electron temperatures, while Figure 2.12(b) shows the fraction of hot electrons and electron RMS radius normalized to the initial RMS radius.

Both the hot and cold temperatures increase as the cluster gains energy from the electric field, until the laser intensity ramps down. The hot electrons gain energy from their strong interaction with the laser electric field; their larger orbital excursions take them outside the cluster core to a region of high electric field. The hot electrons can then undergo the transit time resonance and steadily gain energy [4]. The cold electrons obtain energy through collisions with the ions, which are accelerated outward by the growing halo of hot electrons. As the laser intensity ramps down, the power coupled into the cluster begins to decline, and the hot electrons give up energy via acceleration of the ion core.

Figures 2.13(a) and 2.13(b) show the results of our kinetic calculation, where we have applied a smoothing function to the results in the time domain with a damping constant of $.018 \omega_p$. Each spectrum is offset by $10(\omega^2/2)$. The dielectric resonance at $\omega_p/\sqrt{2}$ starts relatively broad and further broadens throughout the cluster evolution. The dielectric resonance starts red shifted at 54 fs, becomes increasingly red shifted until 188 fs, and then blue shifts from 188 fs to 215 fs. The early red shifting results from the core electrons that contribute the bulk of the plasma density, while maintaining a low temperature (Figure 2.12). The first order thermal correction to the plasma dispersion is thus small, and the redshift continues to increase as the cluster electrons become more diffuse. At 188 fs the number of hot electrons has become appreciable and their temperature is high enough to contribute a thermal correction to the cold plasma dispersion, resulting in the blue shift. The expansion of the cluster and increase in temperature continue to compete throughout the rest of the cluster evolution leading to a non-monotonic spectral shift. For times later than 295 fs the cluster has begun to explode and the plasma frequency of the cluster core begins to drop. The redshift then transitions to an actual change in the dielectric resonant frequency.

At low frequencies we see the enhancement of the polarizability due to the electron bounce resonance. The increase in temperature and number of hot electrons as the cluster evolves provides a stronger interaction of the cluster with the laser field, providing the increased enhancement over time. The hot electrons, having larger orbital excursions, leave the cluster core where they experience the unshielded laser

electric field. The laser field does work on the electrons resulting in the observed enhancement of the polarizability.

2.5 Summary and Conclusions

We have developed a fully kinetic, two temperature, linear model for the cluster polarizability in 2D. The Vlasov-Poisson system of equations was solved for the cluster equilibrium, and linearized with respect to the electric field for determining the cluster dipole response. In a cluster the electron plasma frequency far exceeds the ion plasma frequency, and hence the ions are treated as frozen. Based on this model, we have developed a code to solve for the cluster polarizability. The code uses temperatures, ion densities, and boundary electric fields from a PIC simulation for determination of the cluster equilibrium [4]. In the large radius limit the electric field was matched onto the applied laser field. By applying the laser field as an impulse we have determined the response of the cluster to all frequencies simultaneously.

The first order electron distribution function is found by integrating the equilibrium electron orbits through the first order potential. As a result, this model accounts for the non-local response of individual electrons to an applied laser field. The polarizability is calculated by determining the ratio of the dipole moment, based on the first order electron density, and the applied electric field. The code was validated by comparing the kinetic results of a uniform ion profile with a single electron species at 51 eV to the results of a zero temperature fluid model.

We have calculated cluster polarizabilities for three cases. In the first case we used an essentially uniform ion density, and varied the electron temperature while maintaining a fixed charge imbalance. The second case examined a diffuse ion profile for different electron temperatures. The final case explored the linear cluster response at different times during the cluster evolution. All of these results show a strong cluster response at frequencies much lower than the standard dielectric resonance, $\omega_p / \sqrt{2}$. We have concluded that this response is due to the electron bounce resonance. The electron motion was shown to have two frequencies, a radial bounce frequency, and a rotational frequency. When the proper frequency matching condition between the orbital frequencies and laser frequency is met, $\omega = n\omega_r \pm \omega_q$, the laser field is able to do a large amount of work on the electron. The electrons then have a larger effective orbital radius, and contribute to an enhanced dipole moment. The amplitude and width of response is determined by the first order cluster potential and the RMS radius of electrons in the cluster. Typically the low frequency response is due to the $n=1$ resonance. The bounce resonance also contributes to structure at frequencies close to $\omega_p / \sqrt{2}$ for $n=2$ and 3. The response at these frequencies tends to be lower, however, as the detuning between the frequencies gets amplified by the factor n .

In addition to the structure contributed by the bounce resonance, the standard dielectric response had a temperature dependent spectral shift. This shift was the result of two competing effects: blue shifts from temperature corrections to the cold plasma dispersion and red shifts due to a decrease in the equilibrium electron density

gradient with increasing temperature. The resonance is also substantially broadened by the combined effects of the diffuse ion density profile and electron temperature.

During the evolution of the cluster, the amplitude of the low frequency polarizability follows the heating of the cluster. As the temperature and number of the hot electrons rises the low frequency amplitude increases. At late times, when the cluster has started to cool through expansion, the low frequency response decreases as the hot electron temperature falls. The high frequency dielectric resonance almost disappears at late times when a large number of hot electrons are able to shield the cluster core from the laser field.

2.6 Appendix

To see that the RMS radius increases as a function of temperature consider the integral definition of the RMS radius

$$\langle r^2(T_e) \rangle_{rms} = \int_0^{\infty} r^2 n_o(r, T_e) d^2r. \quad (38)$$

Inserting the density found from the equilibrium Vlasov equation and differentiating with respect to T_e we have

$$\frac{d}{dT_e} \langle r^2(T_e) \rangle = \frac{qn_o}{T_e} \int_0^{\infty} \left[\frac{d\mathbf{f}_o(r)}{dT_e} - \frac{\mathbf{f}_o(r)}{T_e} \right] r^2 e^{q\mathbf{f}_o(r)/T_e} d^2r \quad (39)$$

In order for the RMS radius to increase then we can show that

$d(q\mathbf{f}_o) / dT_e - q\mathbf{f}_o / T_e > 0$ for all radii. We rewrite this condition equivalently

$$\frac{d}{dT_e} \left(\frac{q\mathbf{f}_o}{T_e} \right) > 0. \quad (40)$$

We proceed by considering the Poisson equation in one dimension. We can rewrite the equilibrium as the integral equation

$$\int \frac{d\mathbf{x}}{q\mathbf{x}\sqrt{8\mathbf{p}(n_{ion}\ln[\mathbf{x}]-n_e\mathbf{x})}} = \frac{r}{\sqrt{T_e}} \quad (41)$$

where we have used the substitution of variables $\mathbf{x} = e^{q\mathbf{f}_o/T_e}$. We can then say that the integral above is some function $g(e^{q\mathbf{f}_o/T_e}) = r/\sqrt{T_e}$. Inverting and taking the log we have that $q\mathbf{f}_o/T_e = G(r/\sqrt{T_e})$, where G is the function defined by taking the operations described above. We can now rewrite the temperature derivate in Eq. (40) in terms of a radial derivative. Our condition now becomes

$$-\frac{r}{2T_e} \frac{d}{dr} \left(\frac{q\mathbf{f}_o}{T_e} \right) > 0 \quad (42)$$

This condition holds for all solutions to our equilibrium Poisson equation for all radii so long as the excess of charge is positive [see Eq. (12)]. Therefore the RMS electron radius increases monotonically with temperature.

It is also worth noting that the increase in RMS radius from one temperature to the next becomes smaller and smaller. We can see this by taking the second derivate of the RMS radius, which one can show is less than zero.

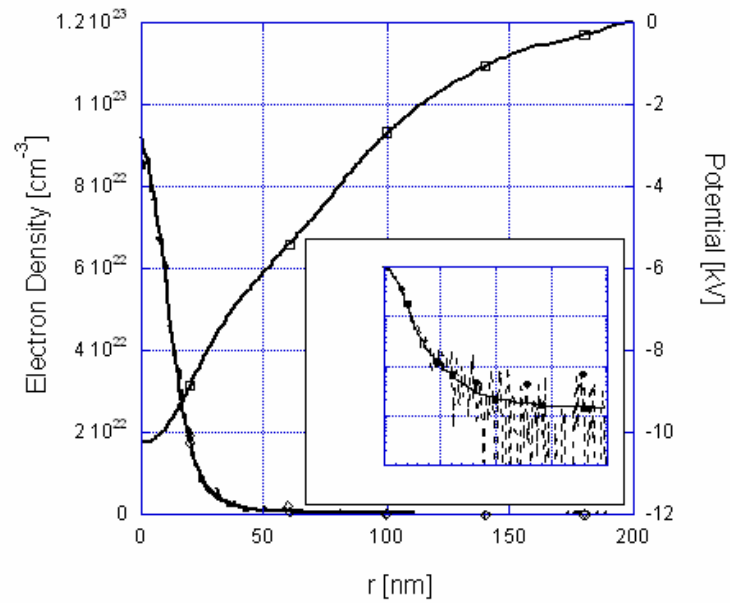


Fig 2.1 Comparison of electron density extracted from the PIC simulation (dotted line) and the result of our equilibrium calculation with parameters (T_c, T_h) and (n_c, n_h) extracted from the PIC simulation (solid line) on the left axis. The inset shows the same comparison on a vertical log-scale. The corresponding electrostatic potential is plotted on the right scale.

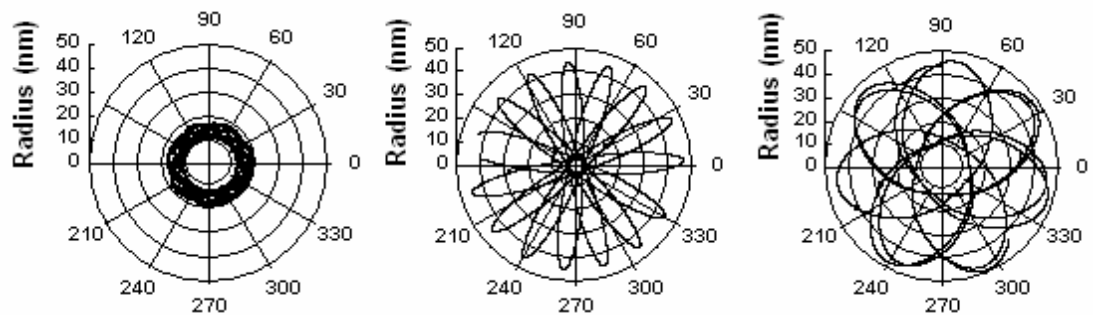


Fig 2.2 Three sample electron trajectories. The cluster radius here is 19 nm.

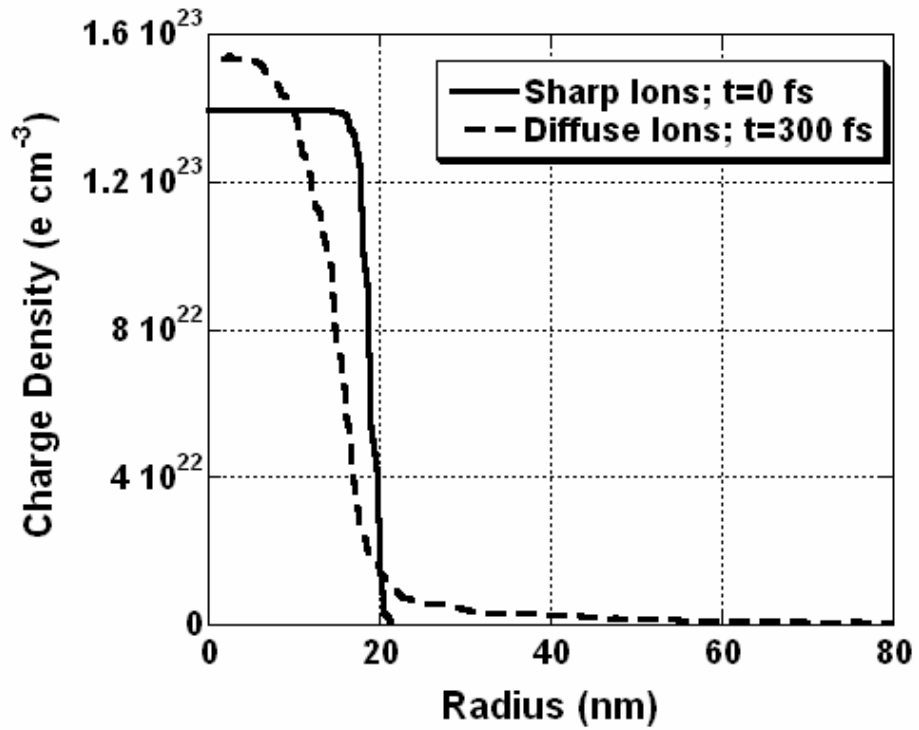


Fig 2.3 The two ion charge density profiles extracted from a PIC code for use in our calculation. The sharp ion density profile (solid) has a very steep gradient at the cluster boundary. The diffuse ion density profile (dotted) trails off smoothly as it approaches the calculation boundary.

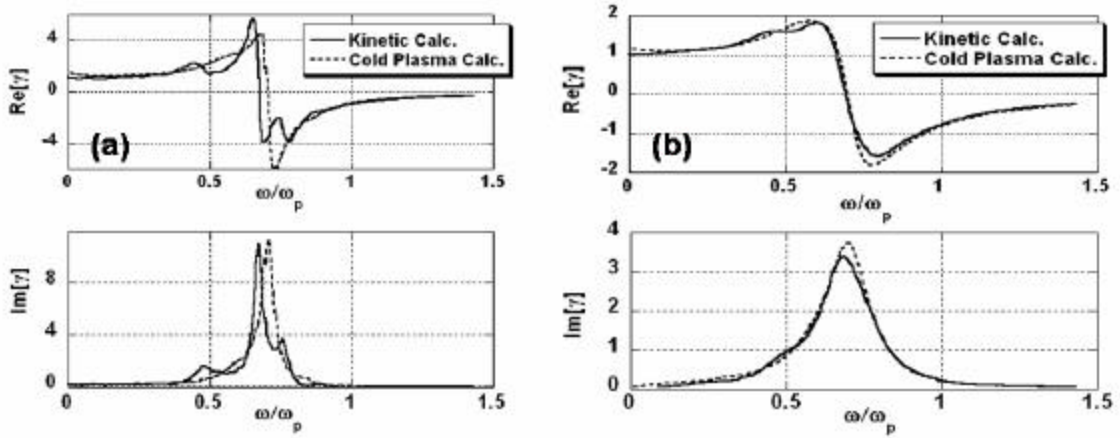


Fig 2.4 Comparison of the real (top graphs) and imaginary (bottom graphs) components of the polarizability spectra from our time-domain kinetic calculation (solid line) and frequency domain fluid calculation (dotted line). A small temperature, $T_e=51$ eV, was used in the kinetic calculation. (a) A smoothing factor of $\mathbf{n} = .0057\mathbf{w}_p(0)$ is used; (b) the smoothing factor is $\mathbf{n} = .057\mathbf{w}_p(0)$.

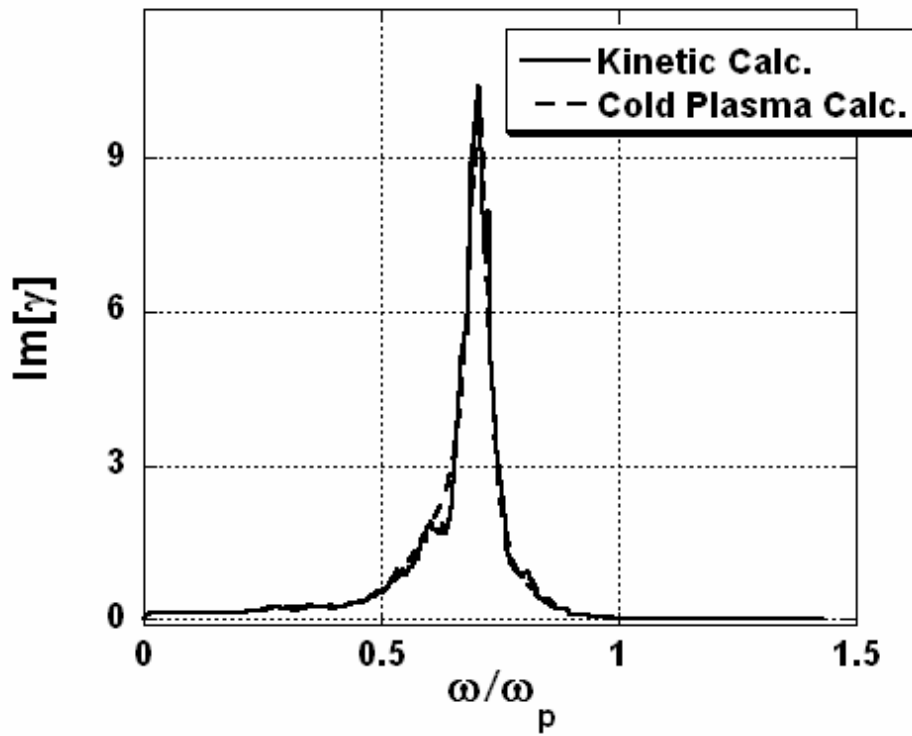


Fig 2.5 Comparison of the imaginary component of the polarizability spectra from our time-domain kinetic calculation with frozen particles (solid line), and frequency domain fluid calculation (dotted line). In both cases a smoothing factor of $n = .0057w_p(0)$ is used. The number of electrons used was 2^7 and the grid spacing was reduced by a factor 5 to eliminate noise associated with fixed particle location.

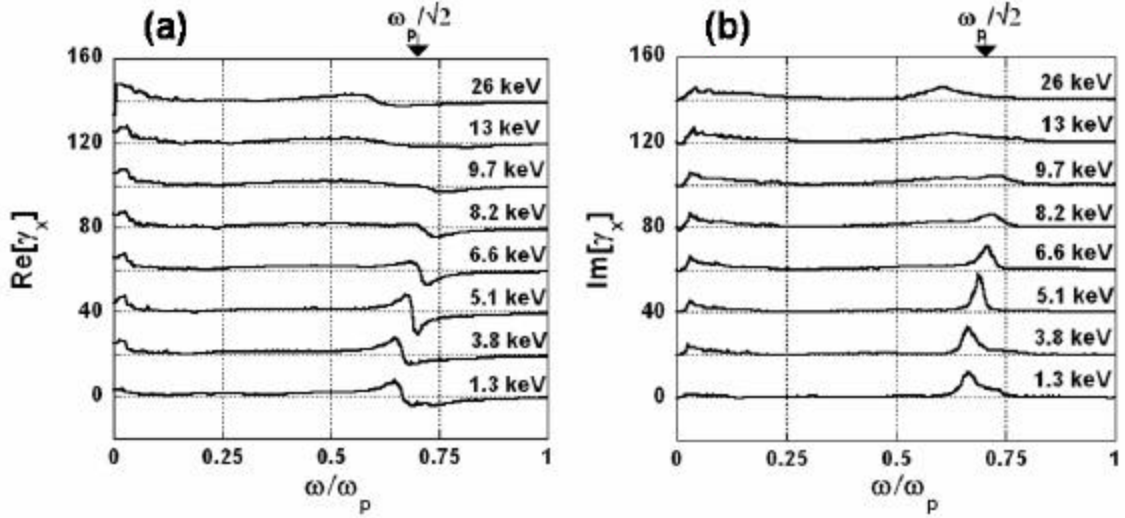


Fig 2.6 Real, Fig. 2.6(a), and imaginary, Fig. 2.6(b), polarizability spectra resulting from the sharp ion profile. Each spectrum has a vertical offset of $20(a^2/2)$ and corresponds to a different electron temperature as labeled on the right. The arrow demarcates where a cold-cluster dielectric resonance would be expected.

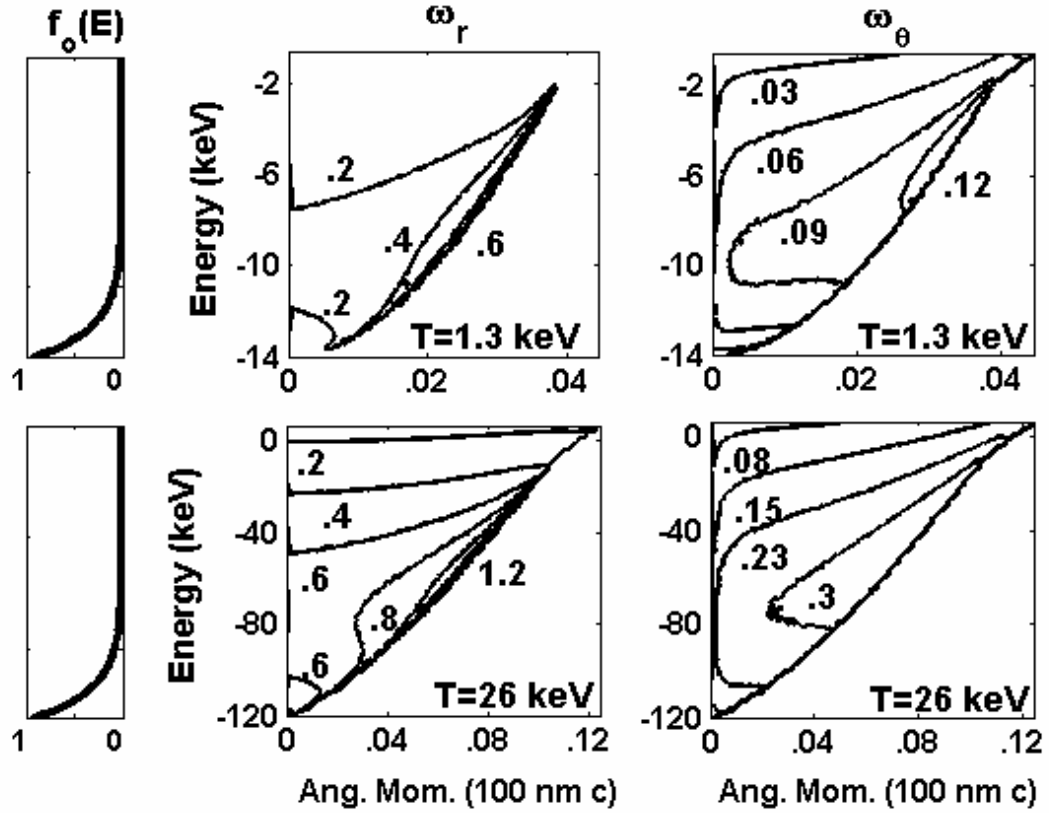


Fig 2.7 Contours of electron radial (left) and angular (right) frequencies in the energy-angular momentum plane. 800 nm represents a contour level of 0.11. The top graphs are at 1.3 keV and the bottom graphs at 26 keV. The equilibrium distribution function is plotted on the left to elucidate where the electrons are concentrated.

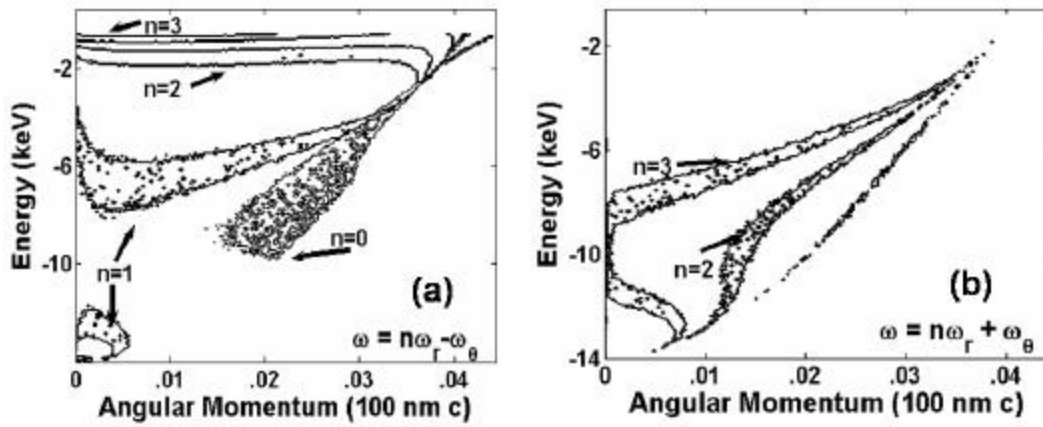


Fig 2.8 Resonant electron bands in the energy-angular momentum plane for the sharp ion profile and $T_e=1.3$ keV. (a) Bands determined by the condition

$\omega = n\omega_r - \omega_\theta \pm .02\omega_p$, where ω_p corresponds to a wavelength of 800 nm. The width $.02\omega_p$ is chosen for illustrative purposes. (b) Bands determined by the condition

$\omega = n\omega_r + \omega_\theta \pm .02\omega_p$, where $\omega_p = \omega_p/\sqrt{2}$. The speckles are a numerical artifact.

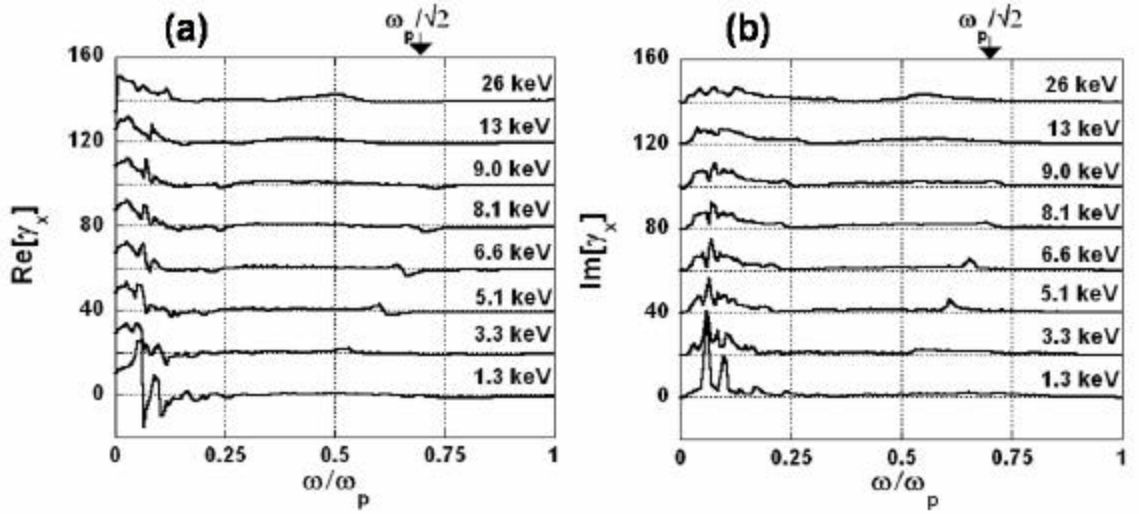


Fig 2.9 Real, Fig. 2.9(a), and imaginary, Fig. 2.9(b), polarizability spectra resulting from the diffuse ion profile. Each spectrum has a vertical offset of $20(a^2/2)$ and corresponds to a different electron temperature as labeled on the right. The arrow demarcates where a cold-cluster dielectric resonance would be expected.

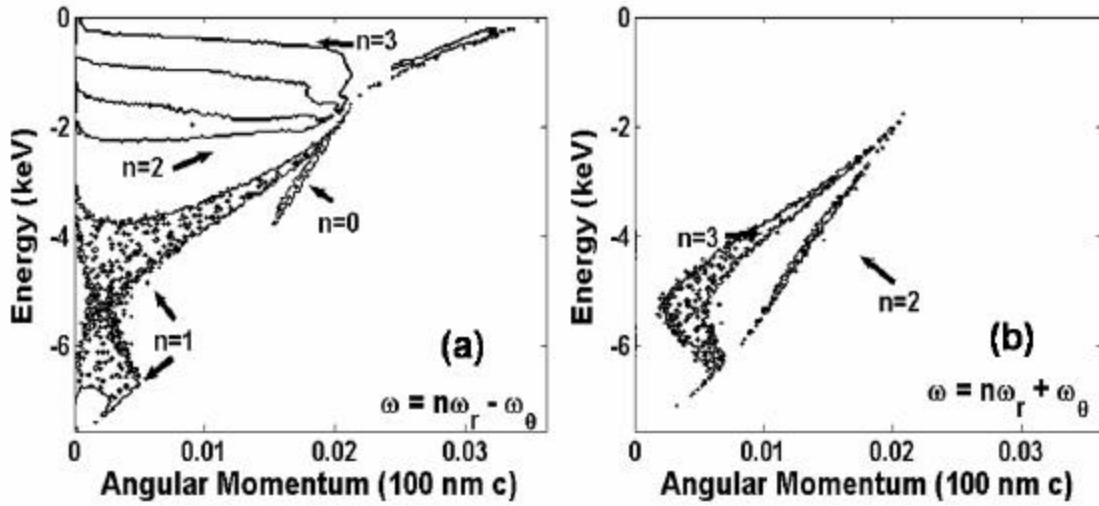


Fig 2.10 Resonant electron bands in the energy-angular momentum plane for the diffuse ion profile with $T_e=1.3$ keV. (a) Bands determined by the condition $\omega = n\omega_r - \omega_\theta \pm .02\omega_p$, where $\lambda = 800$ nm. The width $.02\omega_p$ is chosen for illustrative purposes. (b) Bands determined by the condition $\omega = n\omega_r + \omega_\theta \pm .02\omega_p$, where $\lambda = p/\sqrt{2}$. The speckles are a numerical artifact.

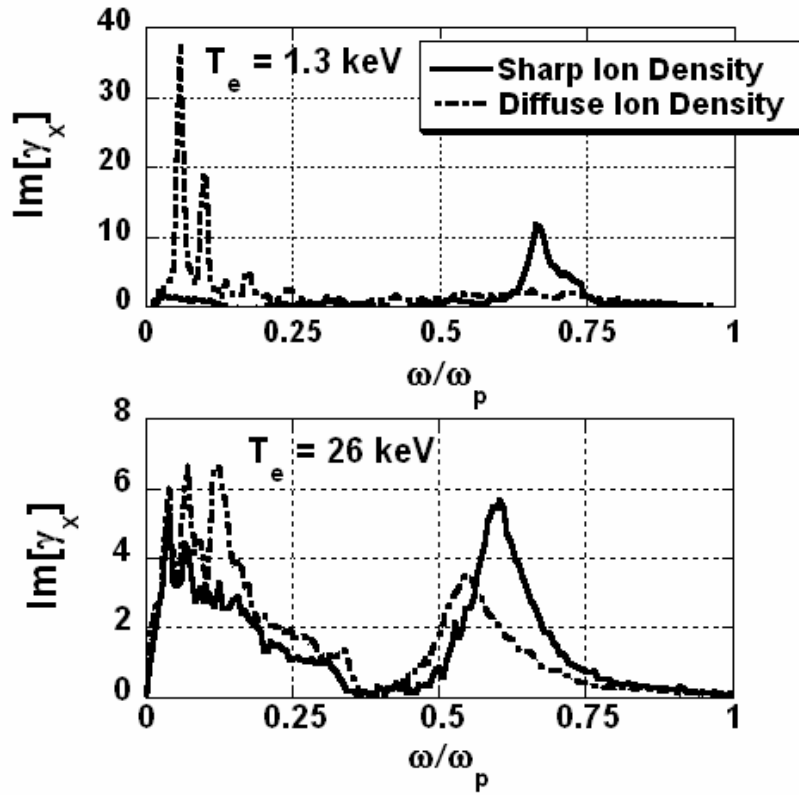


Fig 2.11 Comparison of the imaginary component of the polarizability resulting from the sharp (dotted) and diffuse (solid) ion profile at two different temperatures. The top picture has $T_e=1.3 \text{ keV}$ and the bottom $T_e=26 \text{ keV}$.

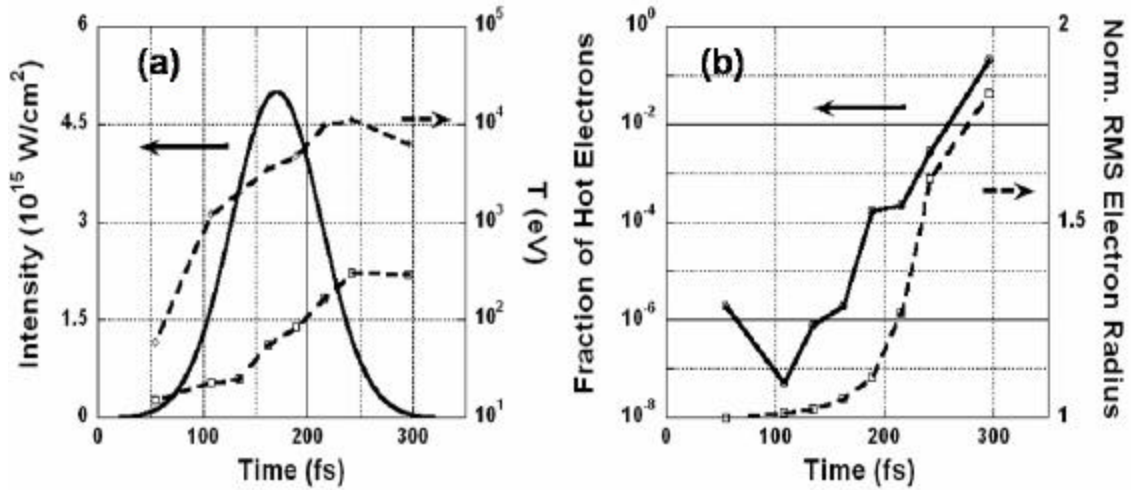


Fig 2.12 (a) On the left axis, the intensity profile (solid) used in irradiating the cluster in the PIC simulation. On the right axis (log scale), hot and cold electron temperatures extracted from the PIC simulation as a function of time (dotted) right axis. (b) On the left axis (log scale), the fraction of hot electrons extracted from the PIC simulation as a function of time (solid). On the right axis, the RMS electron radius of the cluster (dotted).

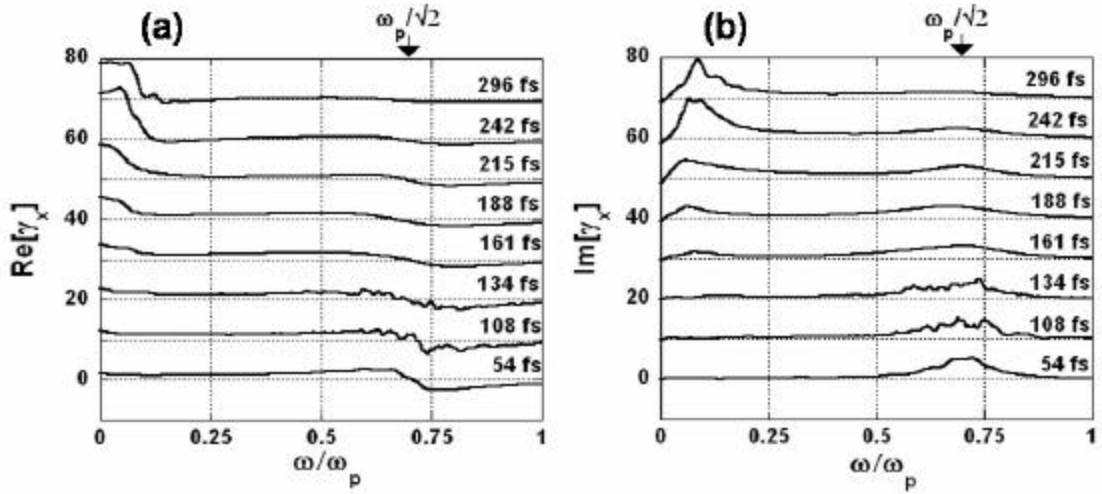


Fig 2.13 Real, Fig. 2.13(a), and imaginary, Fig. 2.13(b), polarizability spectra at different times through the cluster evolution as labeled on the right. Each spectrum has a vertical offset of $10(a^2/2)$. The spectra were smoothed by a factor $n = .018w_p$. The arrow demarcates where a cold-cluster dielectric resonance would be expected.

Pulse Propagation and Electron Acceleration in Corrugated Plasma Channels

3.1 Introduction

Preformed plasma channels allow for the propagation of high intensity short laser pulses over distances unrestrained by vacuum diffraction and intensities unlimited by dielectric breakdown. These properties make the preformed plasma channel ideal for applications that rely on long interaction lengths for efficient operation, including x-ray lasers [37], harmonic generation [55], and laser wakefield accelerators [34-36,56-59]. In particular, laser wakefield acceleration of electrons offers a promising alternative to conventional RF accelerators and has already produced beams of electrons at hundreds of MeV in only several millimeters [60]—a gradient three orders of magnitude higher than SLAC. Wakefield acceleration, however, typically requires very expensive multi-terawatt laser systems. These laser systems fail to fit on conventional laser tables, making wakefield accelerated electron beams inaccessible to smaller labs and unrealistic for use in small scale applications.

Direct laser acceleration of electrons has been proposed as a lower power alternative to laser wakefield acceleration. Laser wakefield acceleration relies on the non-linear ponderomotive force of the laser pulse to generate an electrostatic wave that accelerates the electrons. As a result, the accelerating gradient is quadratic in the laser amplitude. In direct laser acceleration, the laser field itself accelerates the electrons; the accelerating gradient is linear in the laser field amplitude. This linearity allows for a direct laser acceleration scheme that could potentially outperform laser wakefield acceleration.

Direct acceleration is, however, limited by the Lawson-Woodward theorem (LWT) which states: the energy gain of an electron traveling at nearly the speed of light accelerated by a laser pulse in vacuum over an infinite distance is zero [61,62]. Each direct acceleration scheme has thus focused on overcoming one of the underlying assumptions of this theorem to achieve net energy gain. The inverse Cherenkov accelerator was one of the first experiments to demonstrate net energy gain via direct electron acceleration [63]. The observed accelerating gradient of $31 \text{ MeV}/m$ (the maximum energy gain was a few MeV), although modest compared to wakefield gradients, provided proof of principle for direct acceleration. The experiment consisted of radially polarized laser light pulse passed through an axicon lens incident on a gas cell at the Cherenkov angle. The electron beam propagated along the axis of the gas cell. The presence of the gas cell overcomes the vacuum assumption of the LWT. In particular, the presence of the dielectric lowered the phase velocity of the laser light, allowing for phase matching with the electron beam over the length of the gas cell. The dielectric that allows for direct acceleration in the inverse Cherenkov accelerator also presents its limitation. For larger laser intensities ($\sim 1 \times 10^{14} \text{ W}/\text{cm}^2$), which can provide more competitive gradients, dielectric breakdown of the gas occurs. The phase velocity of the laser light in the resulting plasma is superluminal precluding phase matching.

Direct acceleration has also been demonstrated in the semi-infinite vacuum scheme [64]. For a proof of principle experiment, the peak acceleration was found to be $40 \text{ MeV}/m$ comparable to inverse Cherenkov radiation, but maximum energy gains were only on the order of tens of keV. The semi-infinite vacuum accelerator

uses linearly polarized laser light incident at an angle to the propagation axis of a relativistic electron beam. The projection of the electric field onto the electron beam propagation axis provides the accelerating gradient. The interaction length is terminated after a finite length by the presence of a gold plated dielectric. The presence of the terminating boundary allows a population of properly phased electrons to gain energy, breaking the symmetry of equal phasing and dephasing periods over an infinite interaction length predicted by the LWT. Because the electron beam is never properly phase matched to the laser light, extending the interaction length will not result in larger maximum energies as with wakefield and inverse Cherenkov accelerators. Furthermore, in the experiments, the incident angle of the laser beam with the electron beam was small ($\sim 16 \text{ mrad}$). The amplitude of the electric field projected onto the electron propagation is thus significantly lower than its peak value.

The vacuum beat wave accelerator has been proposed as a two laser method for direct electron acceleration [65,66]. The scheme utilizes the laser beams' magnetic forces to achieve acceleration, which are neglected in the LWT. The accelerator involves copropagating two circularly polarized beams each at a different frequency with a relativistic electron beam. The beating of the two laser beams via the $\bar{\mathbf{v}} \times \bar{\mathbf{B}}$ force on the electrons results in an axially directed ponderomotive force that accelerates the electron beam. The phase velocity of the beat wave can be subluminal and hence matched to the electron velocity. Limitations on the interaction length arise, however, due to the vacuum diffraction of the laser light.

The use of plasma waveguides for direct electromagnetic acceleration has been previously suggested by Serafim *et. al.* [40], who proposed guiding a radially polarized laser pulse to accelerate a copropagating relativistic electron beam. For a parabolic plasma density profile, the pulse guides as a transverse magnetic mode. The radial component E_r is a hollow mode with a peak intensity at $r = w_{ch} / \sqrt{2}$, where the channel radius, w_{ch} , is given by $w_{ch} = (2c)^{1/2} (2 / \omega_{p,o}^{\prime\prime 2})^{1/4}$ and $\omega_{p,o}^{\prime\prime 2}$ is the second spatial derivative of the plasma frequency. The accelerating field is the associated axial component E_z , which is smaller by a factor of $\sim \lambda / w_{ch}$, where λ is the laser wavelength. The axial electric field peaks at $r = 0$ and passes through zero at $r = w_{ch}$. The magnetic field, B_θ , is purely in the azimuth and has the same radial profile as E_r . Following reference [40], the peak axial acceleration gradient from hollow mode guiding in a plasma channel is given by

$E_z [GeV / cm] = 0.1 \lambda P^{1/2} / w_{ch}^2 [W^{1/2} m^{-1}]$, where P is the peak laser power in W . For a 1 TW laser pulse with $\lambda = 800 \text{ nm}$ in a channel supporting $w_{ch} = 15 \text{ }\mu\text{m}$, E_z is an impressive $\sim 30 \text{ GeV} / m$. If the interaction length is long enough (which determines the total energy gain), this could compare favorably to laser wakefield accelerators and at much lower power: Malka *et al.* used a 30 TW laser to produce an acceleration gradient of $\sim 70 \text{ GeV} / m$ (200 MeV over 3 mm) [67].

Serafim *et al.*'s scaling also suggests that for long enough interaction lengths direct acceleration in the plasma waveguide could outperform the aforementioned direct acceleration schemes. The plasma waveguide overcomes three limitations of these methods. By using a plasma instead of neutral gas, there is no limitation on the

intensity of the accelerating laser as with the inverse Cherenkov accelerator. The natural axial field arising from the propagation of a radial polarized electric field eliminates the need for using the projection of the linearly polarized field as in the semi-infinite vacuum accelerator. A plasma channel with a negative radial gradient in the index of refraction (positive gradient in the plasma density) provides total internal reflections of the laser, eliminating diffraction—the limitation of the vacuum beat wave accelerator.

Extending the interaction length in the plasma waveguide is, however, a problem. The phase velocity of the laser is superluminal and the axial accelerating electric field cannot be phase matched to an electron beam. An electron traveling at nearly c would slip $2\mathbf{p}$ out of phase with the accelerating field after traveling a dephasing length $L_d = \mathbf{l} (n_o / n_{cr} + 2\mathbf{l}^2 / \mathbf{p}^2 w_{ch}^2)^{-1}$, where n_o is the on-axis electron plasma density of the channel and n_{cr} is the critical plasma electron density for wavelength \mathbf{l} [68]. The electron gains no net energy: it would accelerate for a distance $L_d / 2$, and then decelerate an equal amount over the next $L_d / 2$.

The experimentally created corrugated plasma waveguide shown in Fig. 3.1 could *quasi*-phase match the laser and electron beam [15]. This can be viewed in two ways. The axially periodic plasma density provides a local phase velocity that is faster in regions of high density and slower in regions of low density. If the laser-electron dephasing length L_d and the corrugation period are matched, the symmetry between acceleration and deceleration in a dephasing cycle is broken, and a properly phased electron will gain net energy; this process can be viewed as the inverse of transition radiation [69]. Alternatively, the guided mode can be viewed as a composition of

Fourier spatial harmonics due to the presence of the axially periodic density. For the proper corrugation period, the phase velocity of the spatial harmonics is subluminal, and can be matched to the electron beam velocity. Matching the corrugation period to the laser-electron dephasing length L_d is equivalent to matching the phase velocity of a spatial harmonic to the electron velocity.

The goal of this section is to examine laser pulse propagation and electron beam dynamics in the corrugated plasma waveguide and to demonstrate that large gradients ($\sim 10 \text{ GeV}/m$) over long interaction lengths ($\sim 2 \text{ cm}$) are possible. In section 3.2 we present an analytic model for pulse propagation that provides insight into the field structure inside a corrugated plasma waveguide. The pulse propagation is examined using the slowly varying envelope approximation. The electron density profile used models that shown in Figure 3.1, and allows for an analytic solution to the wave equation. With the field solution, we derive a scaling law for electron energy gain, and compare it to wakefield acceleration and other direct acceleration schemes in section 3.3. Section 3.4 includes calculations and analysis of fully relativistic electron trajectories in the laser electromagnetic field. The calculations are also used to validate the scaling law. Section 3.5 contains the conclusions.

3.2 Laser Pulse Propagation in the Corrugated Plasma Waveguide

We start with the radial component of the laser vector potential:

$$A_{\perp} = \hat{A}_r(r, z, t) \exp[i(k_o z - \mathbf{w}_o t)] + c.c. \quad (43)$$

where k_o and ω_o are the central wave number and frequency of the laser pulse respectively. We assume the pulse remains azimuthally symmetric for all time, and consider corrugated plasma channels that have sufficiently low electron densities such that the plasma frequency satisfies $\omega_p \ll \omega_o$, where $\omega_p^2 = 4\pi e^2 n_e(r, z) / m_e$, e is the electron charge, m_e the electron mass, and n_e is the electron density. In this regime the envelope \hat{A}_r evolves on the time scale ω_o / ω_p^2 which is much longer than the laser period, $2\pi / \omega_o$. The slowly varying envelope equation then determines the evolution of the laser pulse:

$$\left[2ik_o \left(\frac{\partial}{\partial z} + \frac{1}{c} \frac{\partial}{\partial t} \right) + \frac{1}{r} \frac{\partial}{\partial r} r \frac{\partial}{\partial r} - \frac{1}{r^2} \right] \hat{A}_r = \frac{\omega_p^2(r, z)}{c^2} \hat{A}_r \quad (44)$$

where $\omega_o = k_o c$, and we have assumed that the electron plasma responds linearly and as a non-relativistic cold fluid. We will examine the validity of this assumption in Appendix I. The r^{-2} factor in Eq. (44) arises from the cylindrical symmetry of the problem. For solutions of Eq (44) the appropriate boundary condition at the origin is $\hat{A}_r(r=0, z, t) = 0$. To determine the boundary condition at $r = \infty$ we must consider the electron density profile, $n_e(r, z)$. For cases of interest the plasma channel effectively guides the laser pulse and we may consider $\hat{A}_r(r \rightarrow \infty, z, t) = 0$.

Because the laser-electron dephasing length L_d depends on the electron's velocity, acceleration of sub-relativistic electrons would require a structure with a either a graded modulation period or an axial taper of the electron density to ensure that the electron remained phase matched to the laser over the entire interaction length. For mathematical simplicity we consider a fixed modulation period and an

axially uniform background density, suited to acceleration of electrons with $g \gg 1$ for which the relativistic electron velocity depends only weakly on gamma and L_d is nearly constant. We limit our analysis to a periodic electron density profile that models Fig. 3.1,

$$n_e(r, z) = n_o[1 + \mathbf{d} \sin(k_m z)] + n_o'' r^2 / 2, \quad (45)$$

where \mathbf{d} is the relative amplitude of the density modulation, n_o'' determines the radial dependence, and k_m is the wave number describing the axial periodicity of the channel. For large radii the solution to Eq. (44) is evanescent as the local transverse wave number, $(ck_{\perp}) \sim \sqrt{\mathbf{w}^2 - \mathbf{w}_p^2(r, z) - (ck_z)^2}$, necessarily passes through zero at some radius, and becomes purely imaginary. This is consistent with our boundary condition, $\hat{A}_r(r \rightarrow \infty, z, t) = 0$, or equivalently the density profile is taken to be lossless. In Appendix II we examine the loss of pulse power from a leaky channel and provide a condition for which the lossless density profile is valid.

The radial dependence, n_o'' can also be modulated, but can lead to unstable oscillations in the laser spot size as demonstrated in Appendix III and discussed in reference [41]. These oscillations can lead to significant leakage of pulse power from a plasma channel, which cannot be captured by our present analytic model.

Furthermore, exact solutions to Eq. (44) with the density profile in Eq. (45) exist, which will simplify analysis of the electron beam dynamics. In arriving at Eq. (44) we have chosen a gauge in which the electrostatic potential $\Phi = 0$. Using this gauge and the fact that $\bar{\nabla} \cdot \bar{E} \approx 0$ to order $\sim (\mathbf{w}_p / \mathbf{w})^2$, we have that $\bar{\nabla} \cdot \bar{A} \approx 0$. Thus once A_r

has been determined, A_z and the axial electric field can be determined by the condition $\vec{\nabla} \cdot \vec{A} = 0$.

The slowly varying envelope approximation neglects second derivatives in z and t in the wave equation which are responsible for a subluminal group velocity. However, the group velocity can be explicitly restored by replacing $c^{-1}\partial/\partial t$ with $v_g^{-1}\partial/\partial t$ in Eq. (44). Here $v_g/c = 1 - \mathbf{w}_{p,o}^2/2\mathbf{w}^2 - 4/(k_o w_{ch})^2$, and we define $\mathbf{w}_{p,o}^2 = \langle \mathbf{w}_p^2(0, z) \rangle_z$, where the brackets represent an average over z and $w_{ch} = (2c)^{1/2} (2/\mathbf{w}_{p,o}^2)^{1/4}$ is the width of the guided mode. We note that the group velocity is strictly subluminal due to the presence of the background plasma and guiding channel.

The lowest eigenmode solution of Eq. (44) is:

$$\hat{A}_r(r, z, t) = A_o \frac{r}{w_{ch}} e^{-r^2/w_{ch}^2 - (z - v_g t)^2/s_z^2} \sum_n i^n J_n(\mathbf{y}) e^{-i\mathbf{y} \cdot i(\mathbf{d}k + nk_m)z} \quad (46)$$

where $J_n(\mathbf{y})$ is the n^{th} order Bessel function of the first kind, $\mathbf{y} = \mathbf{d}\mathbf{w}_{p,o}^2/2c^2 k_o k_m$, and $\mathbf{d}k = -k_o^{-1}(\mathbf{w}_{p,o}^2/2c^2 + 4/w_{ch}^2)$. We take the pulse to have a Gaussian temporal shape with duration s_z/v_g . In Eq. (46), the laser pulse is written as a sum of spatial harmonics. The harmonics have a relative amplitude given by $J_n(\mathbf{y})$. For our experimental conditions of $(\mathbf{w}_{p,o}/\mathbf{w}_o)^2(k_o/k_m) \ll 1$, $\mathbf{y} \ll 1$, and $J_n(\mathbf{y}) \sim \mathbf{y}^n/2^n n!$. For small \mathbf{y} the relative amplitude drops rapidly with increasing harmonic number. Thus only the first few spatial harmonics contribute to the electromagnetic field

structure in the corrugated plasma waveguide. This is seen in Fig. 3.2(a) which shows the relative amplitude for $n = 0, 1, 2, 3$ spatial harmonics as a function of \mathbf{y} .

By forming the ratio of \mathbf{w}_o to k , and using the fact that $|k_o| \gg |nk_m|, |\mathbf{dk}|$, we obtain the effective phase velocity $v_{p,n}$ for the n^{th} spatial harmonic:

$$\frac{v_{p,n}}{c} \simeq 1 - \frac{nk_m}{k_o} + \frac{\mathbf{w}_{p,o}^2}{2\mathbf{w}^2} + \frac{4}{(k_o w_{ch})^2}. \quad (47)$$

It should be mentioned that for very large values of n , $|k_o| \gg |nk_m|$ is no longer valid, but as demonstrated above the amplitude of these modes is negligible. The last two terms in Eq. (47) are responsible for the superluminal phase velocity in uncorrugated plasma channels. The second term, due to the axial periodicity of plasma, allows for subluminal phase velocities. The condition for subluminal phase velocity can then be expressed in terms of the laser and channel parameters:

$nk_m > k_o[\mathbf{w}_p^2 / 2\mathbf{w}^2 + 4/(k_o w_{ch})^2]$. Figure 3.2(b) depicts the phase velocity of the $n = 0, 1, 2, 3$ spatial harmonics as a function modulation period for experimental parameters used in reference [15]. As expected the fundamental laser mode ($n = 0$) is strictly superluminal. The $n = 1$ spatial harmonic becomes subluminal for modulations periods of ~ 300 nm; modulations of similar period have been created in experiments [15], which is promising for future experiments on direct acceleration.

The local nature of the laser phase velocity is apparent upon rewriting the sum in Eq. (46):

$$\sum_n i^n J_n(\mathbf{y}) \exp[ink_m z] = \exp[i\mathbf{y} \cos(k_m z)]. \quad (48)$$

We find the local wavenumber by taking the gradient of $(k_o + \mathbf{d}k)z - \mathbf{y} + \mathbf{y} \cos(k_m z)$.

The local phase velocity of the guided mode is then

$$\frac{v_p(z)}{c} \simeq 1 + \frac{\mathbf{w}_{p,o}^2}{2\mathbf{w}^2} [1 + \mathbf{d} \sin(k_m z)] + \frac{4}{(k_o w_{ch})^2}. \quad (49)$$

In regions of high density, $k_m z = \mathbf{p}(1/2 + 2\ell)$, where ℓ is an integer, the phase velocity is a maximum, and in regions of low density $k_m z = \mathbf{p}(3/2 + 2\ell)$ the phase velocity is a minimum. The difference in local phase velocity between peak and minimum density is $\Delta v_p = \mathbf{d}(\mathbf{w}_p / \mathbf{w})^2$. Figure 3.2(c) shows the local phase velocity as a function of axial distance. We note that the local phase velocity is always superluminal. Equation (48) also demonstrates that the spatial harmonics of the guided mode are a result of periodic phase modulations in the laser due to the axial periodic plasma density. Furthermore, the relative amplitude of the spatial harmonics is determined by the amplitude of the phase modulation, \mathbf{y} .

3.3 Scaling Law and Comparison to Other Schemes

With an analytic expression for the electromagnetic field in the corrugated plasma waveguide, a scaling law for the electron energy gain via quasi-phase matched direct acceleration can be derived. We start with the expression for the energy gain of an electron in an electric field

$$\Delta \mathbf{g} = -\frac{q}{m_e c^3} \int \bar{\mathbf{v}} \cdot \frac{\partial \bar{\mathbf{A}}}{\partial t} dt, \quad (50)$$

where $\mathbf{g} = \sqrt{1 + |\bar{\mathbf{p}} / m_e c|^2}$. We consider an electron with initial conditions $(r, v_r) = (0, 0)$, and $(z, v_z) = (z_o, v_{z,o})$, where $v_{z,o}$ is assumed to be close enough to c such that $(1 - v_z / c) \omega_o t \ll 1$ over the process of acceleration; the electron energy is high enough such that \mathbf{g} depends weakly on velocity, and phase slippage due to acceleration can be neglected. Recalling that the axial electric field provides the acceleration, we have

$$\Delta \mathbf{g} = -2 \frac{q \mathbf{W}}{m_e c^2} \text{Re} \left[\int i \bar{A}_z dt \right]. \quad (51)$$

The $n = 1$ spatial harmonic is chosen to be phase matched to the electron because it is the largest amplitude mode that also supports a subluminal phase velocity. For phase matching, the phase velocity of the $n = 1$ spatial harmonic is set to c , which can be accomplished experimentally by adjusting the corrugation period: $k_m = k_o [\mathbf{w}_p^2 / 2 \mathbf{w}^2 + 4 / (k_o w_{ch})^2]$. Although the electron has been phase matched to the $n = 1$ spatial harmonic, every spatial harmonic contributes to the energy change of the electron. Upon inserting the axial vector potential into Eq. (51), we find the energy contribution of each spatial harmonic to scale as $\Delta \mathbf{g}_n \sim J_n(\mathbf{y}) \sin[ck_m(n-1)t] / (n-1)$. The contribution from all the harmonics is oscillatory except for the phase matched $n = 1$ harmonic, which provides linear energy gain as a function of time: $\Delta \mathbf{g}_1 \sim J_1(\mathbf{y}) ck_m t$. This is shown in Fig. 3.2(d). Not only do the higher harmonics oscillate in time, their energy contribution is small due to the coefficient $J_n(\mathbf{y})$. Because acceleration will occur over distances much longer than the modulation

period, we can neglect the contribution from the non-phase matched harmonics. The expression for the time-dependent energy gain is then

$$\Delta \mathbf{g} \simeq 2\mathbf{d}a_o \left[1 + \frac{2\mathbf{I}_p^2}{\mathbf{p}^2 w_{ch}^2} \right]^{-1} \left(\frac{ct}{w_{ch}} \right), \quad (52)$$

where $\mathbf{I}_p = 2\mathbf{p}c / w_{p,o}$.

As discussed in the previous section, the group velocity of the guided mode in the channel is subluminal. An electron traveling at approximately c will then outrun the pulse in the pulse length dephasing time, $t \sim \mathbf{s}_z / (c - v_g)$, which places a limit on the interaction time. Upon some algebra, we then obtain an expression for the pulse length limited energy gain in quasi-phase matched direct acceleration:

$$\Delta \mathbf{g}|_{QPM} \simeq 4\mathbf{d}a_o \left(\frac{\mathbf{s}_z}{w_{ch}} \right) \left(\frac{\mathbf{I}_p}{\mathbf{I}} \right)^2 \left(1 + \frac{2\mathbf{I}_p^2}{\mathbf{p}^2 w_{ch}^2} \right)^{-2}. \quad (53)$$

The energy gain scales linearly with both the amplitude of the density modulations, \mathbf{d} , and the field amplitude a_o . Because thinner plasma channels can support higher axial electric fields, the energy gain is inversely proportional to w_{ch} .

The interaction length can be extended by increasing the pulse length, \mathbf{s}_z , or by increasing the group velocity, which is represented by the factor

$$\left(\mathbf{I}_p / \mathbf{I} \right)^2 \left(1 + 2\mathbf{I}_p^2 / \mathbf{p}^2 w_{ch}^2 \right)^{-2} \text{ in Eq. (53).}$$

Eq. (53) can be compared to similar equations predicting the energy gain in other acceleration schemes. For the comparison, we consider parameters similar to those used in reference [15]: a laser wavelength $\mathbf{I} = 800 \text{ nm}$, matched beam width of $w = 15 \text{ }\mu\text{m}$, normalized amplitude $a_o = .25$ (corresponding to a laser power of

2 TW), pulse length $s_t = 300$ fs, on axis plasma density $n_o = 7 \times 10^{18} \text{ cm}^{-3}$, corrugation amplitude $d = .9$, and modulation period of $T_m = .035$ cm (these parameters will be used throughout the rest of the paper unless otherwise stated). A slightly larger density amplitude modulation is used, which may be obtainable upon further experimental exploration. With these parameters, the predicted energy gain for direct acceleration in the corrugated plasma waveguide is $\Delta \mathbf{g}|_{QPM} \sim 1000$.

By comparison, the dephasing-limited energy gain for resonant laser-wakefield acceleration is [70]

$$\Delta \mathbf{g}|_{LWFA} \simeq \frac{a_o^2}{(1 + a_o^2/2)^{1/2}} \left(\frac{I_p}{I} \right)^2 \left(1 + \frac{I_p^2}{\mathbf{p}^2 w_{ch}^2} \right)^{-1}. \quad (54)$$

For the parameters listed, $\Delta \mathbf{g}|_{LWFA} \sim 14$. As expected, direct acceleration produces higher gradients at lower laser powers. In the best case scenario, for semi-infinite vacuum acceleration the energy gain is given by $\Delta \mathbf{g}|_{SVA} \simeq a_o \mathbf{g}_o / 2$ [44], where \mathbf{g}_o is the initial electron energy; this only provides an energy gain of $\Delta \mathbf{g}|_{SVA} \sim 13$. The energy scaling for vacuum beat wave acceleration is given as [45]

$$\mathbf{g}_f^2 = \mathbf{g}_o^2 + 8\mathbf{p}^2 \left(\frac{a_o w_{ch}}{I_1} \right)^2 \left(\frac{I_1}{I_2} - 1 \right). \quad (55)$$

For $I_1 = 2I_2$ the predicted energy gain is $\Delta \mathbf{g}|_{VBWA} \sim 9$. For parameters achievable on an actual table top laser at low power, the scaling laws predict that the energy gain in quasi-phase matched acceleration exceed those of other schemes by at least an order of magnitude. The derived scaling law for quasi-phase matched acceleration will be validated in the next section.

3.4 Beam Dynamics

To study electron beam dynamics and validate the energy scaling, we integrate the fully relativistic electron equations of motion in the laser electromagnetic field determined by Eqs. (44) and (45), and the condition that $\bar{\nabla} \cdot \bar{A} = 0$, while neglecting space-charge effects. After the electromagnetic forces have been found, we provide estimates on the maximum beam density for which neglecting the space charge is valid.

3.4.1 Equations of Motion

We write the generalized electron equation of motion as:

$$\frac{d\bar{p}}{dt} = -\frac{q}{c} \left(\frac{\partial \bar{A}}{\partial t} - \bar{v} \times \bar{\nabla} \times \bar{A} \right) \quad (56)$$

where $\bar{p} = \mathbf{g} m_e \bar{v}$ and $\mathbf{g}^2 = 1 + |\bar{p} / m_e c|^2$. Recalling that $I / w_{ch}, \mathbf{w}_p / \mathbf{w} \ll 1$, we can write the three simplified components of Eq. (56) in terms of A_{\perp} :

$$\frac{dp_r}{dt} = \frac{L^2}{m_e r^3} + q\mathbf{k} \left[1 - \frac{v_z}{c} \left(1 + \mathbf{k}^{-2} \frac{\partial}{\partial r} \bar{\nabla} \cdot \hat{r} \right) \right] A_{\perp} \quad (57)$$

$$L = \text{const.} \quad (58)$$

$$\frac{dp_z}{dt} = -q \left[(\bar{\nabla} \cdot \hat{r}) - \mathbf{k} \frac{v_r}{c} \left(1 + \mathbf{k}^{-2} \frac{\partial}{\partial r} \bar{\nabla} \cdot \hat{r} \right) \right] A_{\perp}, \quad (59)$$

where $L = \mathbf{g} m_e r^2 \dot{\mathbf{q}}$, $\mathbf{k}(z, t) = ik_o - 2(z - ct) / \mathbf{s}_z^2$, and taking twice the real part, $2\text{Re}[\]$, is understood, but not symbolically written.

The first term in Eq. (57) is the force due to the transverse electric field. The last two terms, proportional to v_z , are the contribution from the magnetic field (the $\bar{v} \times \bar{B}$ force). The last term, in particular, is a contribution due to the finite spot size of the laser, which will have important consequences on the transverse dynamics. The constancy of $L = gm_e r^2 \dot{\mathbf{q}}$ is a result of using the azimuthally symmetric, lowest transverse magnetic mode of the channel. The first force in the z direction is simply the z component of the laser electric field which will accelerate the electron to high energies. The second force which is smaller by $\sim (I/w_{ch})(v_{\perp}/c)$ is the contribution to the longitudinal Lorentz force from the magnetic field. For this paper, we consider electron beams with zero initial beam divergence, $\bar{J}_b(r, z, t=0) = J_b(r, z, t=0)\hat{z}$, where J_b is the electron beam current density. In this case, the force from the second term in Eq. (59) is small over the entire interaction length, and the z component of the laser electric field provides the dominant force (even if $v_{\perp} \simeq c$, $I/w_{ch} \ll 1$). We do, however, keep this term in our simulation, but neglect it in our analysis later on. Eqs. (57-59) are integrated over the waveguide-limited interaction time, which is the time it takes an electron going nearly c to travel the length of the waveguide. For our simulations the waveguide length is set to 1.8 cm corresponding to waveguides created in reference [15]. It should be noted that for our case, the waveguide limited interaction time is less than the pulse length dephasing time by a factor of ~ 2 ; the maximum energy gain will thus be limited by the waveguide length.

3.4.2 Scaling Law Validation

To validate the scaling law, the electron trajectories were initiated on axis from $-10 \text{ }\mu\text{m}$ to $-11 \text{ }\mu\text{m}$ behind the peak of pulse (one micron is approximately a wavelength or a percent of the full width half maximum). The initial transverse momentum of the electrons was set to zero, and the initial axial momentum, $p_z / m_e c$, was set to three different values: 30, 100, and 1000. Figure 3.3 shows a comparison of our scaling law from Eq. (53) with simulated electron trajectories that have been phase selected to produce the highest energy gain over the waveguide limited interaction length. In Fig. 3.3(a), the effective phase velocity of the $n = 1$ spatial harmonic is matched to three different initial electron velocities by tuning the modulation period, which could be accomplished experimentally by inserting imaging optics in the radially modulated channel formation beam shown in Fig. 3.1. For an initial energy of $g_o = 30$ the electron begins to accelerate but quickly becomes dephased from the $n = 1$ spatial harmonic as its velocity increases. The electron is then decelerated and again becomes phase matched. For $g_o = 100$ the electron and slow wave remain phase matched longer; the increase in electron energy results in a small change to its velocity. The electron does begin to outrun the slow wave towards the end of the waveguide. As expected, we see the best agreement with the scaling law for an initial energy of $g_o = 1000$. The electron's velocity remains essentially constant, and phase matching is maintained over the entire waveguide.

In Fig. 3.3(b) the phase velocity of the $n = 1$ spatial harmonic was set to c for all three initial electron energies. The $g_o = 30$ trajectory never catches up with the spatial harmonic and experiences alternating regions of acceleration and deceleration

as the slow wave continually sweeps past it. The $g_o = 100$ electron gains more energy than when it started phase matched with the spatial harmonic. Before the electron begins to dephase, it is accelerated up to the slow wave phase velocity. The electron spends more time in the acceleration phase and as a result gains more energy. For $g_o = 1000$ the change is minimal; the phase velocity for the $n = 1$ spatial harmonic in the previous case was essentially c already.

The limitations of our scaling law are apparent in Figs. 3.3(a) and 3.3(b). The scaling law assumed phase matching over the entire interaction length, and cannot be applied to lower energies for the distances considered here, explaining the large discrepancy for $g_o = 30$ and $g_o = 100$. As stated previously, for low initial energies gradients in the modulation period or background density are required to maintain phase matching over longer distances. Furthermore, our scaling law assumes a constant pulse amplitude over the entire pulse length (a flat top pulse), whereas the pulse in the simulation was Gaussian. The discrepancy in the slope of the scaling law and the energy gain of the $g = 1000$ particle is a result of the smaller field amplitude experienced by the electron as it moves through the pulse. The resulting energy gains from the simulations for $g_o = 100$ are still at least an order of magnitude better than the energy gains from both laser wakefield acceleration and other direct acceleration schemes.

A simple Hamiltonian model for the longitudinal dynamics explains the features observed in Fig. 3.3. We start with equations describing the evolution of the energy and phase of an electron:

$$\frac{d\mathbf{g}}{dz} = k_o \hat{a}_o \cos(\mathbf{j}) \quad (60)$$

$$\frac{d\mathbf{j}}{dz} = k - \frac{\mathbf{w}_o}{v_z(\mathbf{g})} \quad (61)$$

where $\mathbf{j} = kz - \mathbf{w}_o t$, $k = k_o + \mathbf{d}k + k_m$, $\hat{a}_o = 4J_1(\mathbf{y}) \mathbf{x}_o / k_o w_{ch}$, and it has been assumed that the electron starts on axis near the peak of the pulse. From Eqs. (60) and (61) we find that the Hamiltonian is given by

$$H = k\mathbf{g} - k_o \left(\hat{a}_o \sin(\mathbf{j}) + \sqrt{\mathbf{g}^2 - 1} \right). \quad (62)$$

We note that $k_o / k = v_{p,1} / c$ where $v_{p,1}$ is the phase velocity of the $n = 1$ spatial harmonic. H contains no explicit dependence on z and thus $dH / dz = 0$ or $H(\mathbf{g}_o, \mathbf{j}_o) = H(\mathbf{g}, \mathbf{j})$, where \mathbf{g}_o and \mathbf{j}_o are the initial relativistic factor and phase of the electron respectively.

For mathematical simplicity, we first consider the case when $k_o / k = 1$ or $v_{p,1} = c$, corresponding to Fig. 3.3(b). The electron velocity is then less than the $n = 1$ phase velocity. Eq. (62) then has one solution for $\mathbf{g}(\mathbf{j})$:

$$\mathbf{g}(\mathbf{j}) = \frac{1 + [k_o^{-1} H + \hat{a}_o \sin(\mathbf{j})]^2}{2[k_o^{-1} H + \hat{a}_o \sin(\mathbf{j})]}. \quad (63)$$

Setting $d\mathbf{g} / d\mathbf{j}_o = 0$ and solving for \mathbf{j}_o , we determine what initial phase results in the maximum energy gain: $\mathbf{j}_{o,\max} = \mathbf{p} / 2$. As expected, the maximum energy occurs when the electron starts at a zero of the accelerating field and experiences the entire accelerating phase as the slow wave passes by. We will consider the motion of the maximum accelerated electron and thus set $H = H(\mathbf{g}_o, \mathbf{p} / 2)$.

The denominator of Eq. (63) shows that there is a critical initial energy,

$\mathbf{g}_{ocrit} = (1 + 4\hat{a}_o) / 4\hat{a}_o$, which we rewrite for our parameters using the fact that $\hat{a}_o \ll 1$

$$\mathbf{g}_{ocrit} \simeq \left(\frac{k_m w_{ch}}{4d a_o} \right) \left(\frac{\mathbf{w}}{w_{p,o}} \right)^2. \quad (64)$$

Above \mathbf{g}_{ocrit} , the electron will continually gain energy as it phase slips with respect to the field. Furthermore, for energies above \mathbf{g}_{ocrit} , the electron phase slippage is limited; the electron can phase slip by at most $\mathbf{j}_{max} = \sin^{-1}[H(\mathbf{g}_o \mathbf{j}_o) / \hat{a}_o]$. For energies below \mathbf{g}_{ocrit} , electrons can phase slip by $2\mathbf{p}$ radians and, as a result, undergo energy oscillations as the slow wave fronts continually move past them. The maximum energy for $\mathbf{g}_o < \mathbf{g}_{ocrit}$ is $\mathbf{g}(-\mathbf{p}/2)$. For our parameters $\mathbf{g}_{ocrit} \simeq 81$; both the $\mathbf{g}_o = 100$ and $\mathbf{g}_o = 1000$ cases are above \mathbf{g}_{ocrit} , explaining their steady increase in energy. $\mathbf{g}_o = 30$ is below \mathbf{g}_{ocrit} which explains the energy oscillations. Equation (64) also shows that the critical energy can be reduced by increasing the modulation period; for accelerating low energy electrons, longer modulation periods are preferable.

We now consider the case where the initial electron velocity is matched to the $n = 1$ phase velocity, $v_{p,1} = v_{z,o}$. The Hamiltonian constant is given by

$H(\mathbf{g}_o \mathbf{j}_o) = k / \mathbf{g}_o - k_o \hat{a}_o$, and because we are interested in relativistic electrons

$k_o / k \simeq 1 - 1/2\mathbf{g}_o^2$. Solving Eq. (62) for \mathbf{g} , we have for large electron energies,

$\hat{a}_o \mathbf{g}_o / 2 \gg 1$, that

$$\frac{\mathbf{g}(\mathbf{j})}{\mathbf{g}_o} \simeq 1 + 2\mathbf{g}_o \hat{a}_o [1 - \sin(\mathbf{j})], \quad (65)$$

where the maximum energy gain is given by $\Delta \mathbf{g}_{\max} = (\mathbf{g}_o / \mathbf{g}_{ocrit}) \mathbf{g}_o$. The large energy limit corresponds to our $\mathbf{g}_o = 1000$ case in Fig. 3.3(a). When the electron velocity and $n = 1$ phase velocity are initially matched there is a limit on the maximum energy gain due to the electron outrunning the slow wave. Our parameters give $\Delta \mathbf{g}_{\max} \approx 1.2 \times 10^4$, which explains the similarity between Figs. 3.3(a) and 3.3(b); the $\mathbf{g}_o = 1000$ electron had not yet approached its maximum energy. For lower electron energies $\hat{\mathbf{g}}_o / 2 \ll 1$, we have that

$$\frac{\mathbf{g}(\mathbf{j})}{\mathbf{g}_o} \approx 1 + \sqrt{2\mathbf{g}_o \hat{\mathbf{a}} [1 - \sin(\mathbf{j})]} + \mathbf{g}_o \hat{\mathbf{a}} [1 - \sin(\mathbf{j})], \quad (66)$$

where the maximum energy gain is given by $\Delta \mathbf{g}_{\max} = [(\mathbf{g}_o / \mathbf{g}_{ocrit})^{1/2} + (\mathbf{g}_o / 2\mathbf{g}_{ocrit})] \mathbf{g}_o$, and we have retained an extra order in $(\mathbf{g}_o / \mathbf{g}_{ocrit})^{1/2}$ to better match our results. When $\mathbf{g}_o = 100$, we find that $\Delta \mathbf{g}_{\max} \approx 210$ similar to the value found in Fig. 3.3(a). The energy gain for the $\mathbf{g}_o = 100$ electron is limited when $v_{p,1} = v_{z,o}$, explaining the higher yields in Fig. 3.3(b).

Figures 3.3(a) and 3.3(b) also show a rapid oscillations due to the longitudinal force of the fundamental $n = 0$ laser mode, with the oscillation frequency determined by the difference between the laser fundamental phase velocity and the electron phase velocity, cL_d . Although not visible, the electron also undergoes rapid oscillations due to all other spatial harmonics at a frequency $(n-1)ck_m$, but the amplitude of these oscillations becomes diminishingly small as n is increased $\sim \mathbf{y}^n / 2^n n(n!)$. The rapid oscillations due to $n = 0$ will become important when considering the transverse electron motion.

3.4.3 Transverse Dynamics

For examining the transverse dynamics of the electron beam, electrons were distributed uniformly in the axial direction from -1 mm to -11 mm behind the peak of the pulse and as a Gaussian in the radial direction with varying width, s_b . The initial electron momentum was set to $p_z/m_e c = 100$ and the phase velocity of the $n = 1$ spatial harmonic was set to c .

Figure 3.4 shows the final electron distribution functions as a function of momentum on a log scale after 60 ps , the waveguide limited interaction time. When all the electrons start on axis ($s_b = 0$), the distribution function contains a quasi-mono energetic peak at $p_z/m_e c \approx 400$. The distribution function is also asymmetric about the initial momentum. For larger initial energies, we would expect a distribution function symmetric about the initial momentum; dephasing over the interaction length would be negligible, and an equal number of electrons would start in the accelerating phase as in the decelerating phase. Here some electrons have the proper z_o (initial phase) to be accelerated up to the slow wave, which, as discussed above, can result in higher energies. The remaining electrons are initially accelerated or decelerated based on their phase. These electrons are never properly phase matched and their phase slippage results in a slow spreading of the distribution function about the initial momentum.

As the width of the electron beam is increased from $s_b = 0$ to $s_b = 9 \text{ mm}$ the quasi-monoenergetic peak is lost. The increased electron beam radius places more electrons in the low amplitude periphery of the accelerating field, which decreases as

a function of radius, $A_z \propto 1 - 2r^2 / w_{ch}^2$. Figure 3.5, which shows a comparison of the Gaussian widths of the electron beam to the axial field profile, suggests, however, that for $s_b = 1 \text{ mm}$ and 3 mm most of the electrons still experience the peak of the accelerating field. The loss in the high energy peak is then a result of the transverse motion of the beam electrons.

Some of the features of the transverse dynamics are depicted in the multimedia file linked in reference [71]. The movie shows a subset of electrons distributed uniformly in z from -10 mm to -11 mm behind the peak of the laser with $s_b = 6 \text{ mm}$. The vertical scale is radius and the horizontal scale is $z - ct$, following the movement of the electron beam; both scales are in microns. The color scale is in units of energy normalized to rest mass and changes as the beam propagates. The electrons in the decelerating phase experience a large transverse force and are expelled from the center of the electron beam. The accelerated electrons remain mostly collimated towards the center of the beam, but undergo a slow transverse spreading. The collimation of the higher energy electrons can be used for spatial filtering of the electron beam if quasi-mono energetic peaks are desired. To examine the transverse dynamics in detail, we turn to the transverse equations of motion.

An electron displaced from the axis will experience two types of transverse force in the absence of space charge. For an electron close to the axis, near the peak of the laser pulse, we can write the transverse equation of motion as

$$\frac{dp_r}{dt} = \frac{q}{c} \left[\frac{\partial}{\partial t} + v_z \frac{\partial}{\partial z} - v_z \left(\frac{2}{w_{ch}} \right)^2 \frac{2}{ik_o} \right] A_{\perp}. \quad (67)$$

Inserting the solution for A_{\perp} , and using the phase matching condition for the $n = 1$ spatial harmonic, we obtain an expression for the quasi-phase matched focusing/defocusing force due to the slow wave:

$$F_r^{qpm} = \frac{m_e c^2 k_0 \mathbf{d}a_o}{\left[1 + 2\mathbf{I}_p^2 / (\mathbf{p}^2 w_{ch}^2)\right]} \frac{r}{w_{ch}} \left[1 - \frac{v_z}{c} \left(1 + \frac{8}{k_0^2 w_{ch}^2}\right)\right] \cos(k_0 z - \mathbf{w}_o t). \quad (68)$$

This is the transverse force associated with the phase matched axial accelerating force. The axial and transverse forces are 90° out of phase. As observed in the multimedia file, electrons in the maximum axial accelerating phase experience no quasi-phase matched focusing or defocusing. The force is either focusing or defocusing depending on the phase of the electron, z . In particular, for an axial uniform distribution of highly relativistic electrons for which $\mathbf{j} = k_0 z - \mathbf{w}_o t$ is constant over the entire interaction length an equal number of electrons experience focusing as defocusing. From Eq. (68) we can estimate the shortest time scale for the growth of the focusing/defocusing for orbits slightly off axis as

$$t \sim \left(\frac{2\mathbf{p}}{\mathbf{w}_o}\right) \left(\frac{c}{c - v_z}\right)^{5/6} \left[\frac{(k_o w_{ch})(k_o \mathbf{I}_p)(k_m \mathbf{I}_p)}{16\sqrt{2}\mathbf{p}^5 \mathbf{d}a_o}\right]^{1/3} \quad (69)$$

For our parameters we find that $t \sim 12$ ps for $g_o = 100$, consistent with simulated electron trajectories shown in the reference [71].

The terms proportional to v_z in Eq. (68) result from the $\bar{\mathbf{v}} \times \bar{\mathbf{B}}$ contribution to the Lorentz force. For plane waves as the axial velocity approaches c the quasi-phase matched transverse force becomes diminishingly small. Because the pulse has a finite spot size, we obtain a correction, $8/k_0^2 w_{ch}^2$, that reduces the velocity where the transverse force vanishes. Specifically, we find that the transverse force vanishes

when $\mathbf{g} = k_0 w_{ch} / 2\sqrt{2}$, which for our parameters is $\mathbf{g}_o \simeq 42$. By matching the injection energy to $k_0 w_{ch} / 2\sqrt{2}$, deflection of the electron beam can be limited in the early stages of acceleration. Furthermore, this suggests that by adiabatically changing the channel radius over the interaction length, $w_{ch}(z) = 2\sqrt{2}\mathbf{g}(z) / k_o$, it may be possible to maintain a collimated beam, which will be a topic of future research.

The forces due to the other spatial harmonics ($n \neq 1$) also contribute to the transverse motion of the electron beam. As discussed earlier, the electron moves through the phase fronts of these harmonics and undergoes rapid oscillatory motion, $\mathbf{w}_{osc} \sim (n-1)ck_m$. Over the entire interaction length the oscillations undergo many cycles, $k_o \mathbf{s}_z$ (for our parameters $k_o \mathbf{s}_z \sim 700$). The oscillations themselves thus contribute little to the long term directed motion of the electron beam. However, because of the spatial variation of the field envelope the oscillations can beat and give rise to directed motion through the ir ponderomotive force on the electron beam. The $n=0$ spatial harmonic provides the dominant contribution to this motion on account of its large relative amplitude.

Expanding around the initial electron velocity $\bar{\mathbf{v}} = v_o \hat{\mathbf{z}}$ and averaging over the fast time scale $k_m v_z$, we have to lowest order in \mathbf{I} / w_{ch}

$$F_r^{pm} = -\frac{1}{2m_e \mathbf{g}_o} \nabla \langle p_{1,r}^2 \rangle \quad (70)$$

where the angled brackets denote the time averaging. The contribution to the ponderomotive force from the first order axial momentum $p_{1,z}$, which accounts for corrections to the initial momentum $p_{o,z} = m\mathbf{g}_o v_o$, provides corrections to Eq. (70) of

order $(I/w_{ch})^2$ and has been neglected. Inserting our expression for the axial field, we obtain the ponderomotive force due to the fundamental $n=0$ laser mode for small radii near the peak of the laser pulse:

$$F_r^{pm} = -\frac{2m_e c^2}{\mathbf{g}_0} \frac{r}{w_{ch}^2} a_0^2 \left[1 - \frac{4}{\mathbf{p}^2} \frac{v_o}{c} \left(\frac{\mathbf{I}_p}{w_{ch}} \right)^2 \left(1 + \frac{2\mathbf{I}_p^2}{\mathbf{p}^2 w_{ch}^2} \right)^{-1} \right]^2. \quad (71)$$

The force is independent of the electron's phase. In addition, the hollow profile of the transverse field results in an inward force. The ponderomotive force thus provides a focusing over the entire electron beam. Higher energy electrons will experience a smaller ponderomotive focusing due to the inverse dependence on \mathbf{g}_o , further explaining the small transverse excursions observed in the multimedia file [71]. The second term in the brackets, which results from the finite spot size, reduces the focusing effect of the ponderomotive force. The finite spot size correction is not necessarily negligible, and for our case is $\sim .25$.

The ponderomotive force when taken in addition to the quasi-phase matched focusing/defocusing force provides an overall focusing of the electron beam for small radii as seen schematically in Fig. 3.6. The overall focusing is limited by the amplitude of the ponderomotive force, which is typically smaller than the quasi-phase matched focusing/defocusing force except near the maximum accelerating phase.

The phase independent ratio of the forces is

$$F_r^{pm} / F_r^{qpm} \sim \frac{1}{4\mathbf{g}_o} a_o \left(\frac{k_o w_{ch}}{\mathbf{d}} \right) \left(1 + \frac{\mathbf{I}_p^2}{\mathbf{p}^2 w_{ch}^2} \right)^{-1}, \quad (72)$$

which for our parameters $F_r^{pm} / F_r^{sw} \sim .08$.

Figures 3.7 and 3.8 show the number-averaged final z momentum in units of $m_e c$ as a function of initial and final position respectively for an initial electron beam radius of $s_b = 9 \text{ mm}$. The accelerated electrons started in buckets one half of a slow wavelength long. Buckets are limited in the transverse direction by the laser spot size. After acceleration the momentum is concentrated in z as the high energy electrons move towards the front of the slow wave, but is spread transversely as some of the electrons in the accelerating phase are initially defocused. Figure 3.9 shows the final electron beam density as a function of position; the beam has acquired a significant transverse spread which peaks off axis. Comparing Figs. 3.8 and 3.9 we see that these peaks are mostly composed of lower energy electrons that have been expelled from the center of the electron beam. As seen in the multimedia file and predicted by our analysis the high energy electrons remain collimated at the center of the beam. They see little to no focusing or defocusing quasi-matched force, and only the small focusing ponderomotive force.

The electron beam experiences a net outward density flow as seen in Fig 3.9. At radii greater than $w_{ch}/\sqrt{2}$, electrons that were initially defocused move outside the peak of the hollow mode fields and experience a larger defocusing force due to the ponderomotive force switching sign. These electrons are expelled from the beam. Eventually electrons initially in a focusing phase begin to phase slip and enter the defocusing phase where they undergo the same process.

Many of the transverse effects on the electron beam can be managed by increasing the radius of the plasma channel (matched laser spot size). Increasing the spot size increases the defocusing time in Eq. (69) as $t \sim w_{ch}^{1/3}$. Furthermore, for

highly relativistic injection energies the quasi-phase matched defocusing can be reduced by decreasing the finite spot size correction to the Lorentz force. At the same time, the ponderomotive focusing force would be increased due to the reduction in the spot-size correction. The outward flow of beam electrons can also be minimized by using electron beams with widths less than $w_{ch}/\sqrt{2}$ (for our case $\sqrt{2}\mathbf{s}_r/w_{ch} \sim .85$). Due to limitations on injection beams, it may be easier to increase the channel radius than decrease the electron beam radius. Unfortunately, by increasing the channel radius the predicted energy gain of the electrons decreases, $\Delta g \sim w_{ch}^{-1}$. This can be overcome by maintaining the ratio of the field amplitude to the spot size, $a_o/w_{ch} = \text{const}$. This, however, greatly increases the laser power requirements for quasi-phase matched direct acceleration, $P \sim (a_o w_{ch})^2 \sim w_{ch}^4$. In instances where power is not a limiting factor, larger spot sizes can greatly improve the quality of the accelerated electron beam

3.4.4 Space Charge Estimation

For a simple estimate of the magnitude of the transverse space charge force we consider a uniform cylindrical electron beam. We suppose the electron beam is infinitely long so that we may ignore longitudinal edge effects and thus ignore any axial electric field due to the beam. Noting that the electrons themselves give rise to a radial electric field and that their motion gives rise to an azimuthal magnetic field, we find the space charge force to be

$$F_r^{sc} = \frac{1}{2} m_e w_{p,b}^2 \left(1 - \frac{v_z^2}{c^2} \right) r, \quad (73)$$

where $w_{p,b}$ is the plasma density of the electron beam. The first term in parenthesis is the result of the beam's electric field, and the second term due to the beam's magnetic field. We note that for highly relativistic beams the transverse space-charge force can be neglected altogether.

The maximum allowable charge density can be estimated by forming the ratio of the transverse space-charge force to the quasi-phase matched focusing/defocusing force, F_r^{sc} / F_r^{qpm} :

$$n_{e,b} [cm^{-3}] < \frac{2.3 \times 10^{12}}{(1 + 2I_p^2 / p^2 w_{ch}^2)} \left(\frac{da_o}{k_o w_{ch}} \right) \frac{w_{ch}^{-2} [cm^{-2}]}{(1 - v_z / c)}, \quad (74)$$

where $n_{e,b}$ is the electron beam density, and we have assumed $v_z \simeq c$. Eq. (74) uses the maximum focusing phase of the quasi-phase matched force and as a result is phase independent; the actual maximum charge will be lower by approximately order of magnitude. For our parameters with v_z corresponding to $g_o = 100$ and including an order of magnitude for phases where the transverse force may be smaller, we find that $n_{e,b} < 3 \times 10^{18} cm^{-3}$. For a uniform cylindrical beam with a length and radius of 10 mm , $n_{e,b} = 3 \times 10^{18} cm^{-3}$ corresponds to 10^{10} electrons.

To estimate the longitudinal space charge force, we consider the electron beam after acceleration when the electrons have accumulated at the slow wave fronts as shown in Fig 3.9. If the electron bunch spacing is much smaller than the beam length, the force on one bunch due to adjacent bunches can be neglected. The local Poisson equation for an electron bunch is then

$$\bar{\nabla} \cdot \bar{E} = 4\pi q n_{e,b} \left(\frac{l_b}{2p} \right) d(z), \quad (75)$$

where $\mathbf{l}_b = 2\mathbf{p} / (k_o + \mathbf{d}k + k_m)$ is the spacing between bunches. Integrating over the axial coordinate we obtain the local longitudinal space charge force

$$F_z^{sc} = 2q\mathbf{l}_b n_{e,b}. \quad (76)$$

Forming the ratio F_z^{sc} / F_z^{qpm} , we find an expression for the maximum allowable beam density:

$$n_b [cm^{-3}] < \frac{3.6 \times 10^{12}}{\left[1 + \mathbf{l}_p^2 / \mathbf{p}^2 w_{ch}^2\right]} \mathbf{d}a_o (w_{ch} \mathbf{l}_o)^{-1} [cm^{-2}]. \quad (77)$$

For the parameters used in our simulations we find that $n_{e,b} < 6.3 \times 10^{18} cm^{-3}$ similar to the value obtained for the transverse space-charge force. Unlike the longitudinal space-charge force, the expression is naturally phase independent due to the axial bunching of the electrons. Also, the allowable density does not increase as the electron's axial momentum increases; for highly relativistic electron beams the actual bound on the density is provided by the expression for the longitudinal space charge force, Eq. (77).

3.5 Summary and Conclusions

We have developed an analytic model for laser pulse propagation in a corrugated plasma waveguide, using the slowly varying envelope approximation. The background plasma was assumed to be a cold non-relativistic fluid that responded linearly to the laser field. The plasma density profile was chosen to model the density profiles created in experiments [15], while at the same time providing an analytic solution, facilitating analysis of the electron beam dynamics. The field structure of the laser was examined. It was shown that as a result of the axial periodic density

profile, the guided mode is composed of spatial harmonics. For a small enough plasma corrugation period the phase velocity of the spatial harmonics could be subluminal—a requirement for electron acceleration. The contribution of each spatial harmonic was determined by its relative amplitude, which, for parameters of interest, was shown to decrease significantly with increasing harmonic number. Only the first few spatial harmonics contributed to the field structure in the plasma channel. The spatial harmonics can also be viewed as a periodic phase modulation of the guided mode. The spatially local phase velocity of the guided mode was shown to oscillate at the modulation period.

With the solution for the electromagnetic field, a scaling law for the energy gain via quasi-phase matched direct acceleration was derived. The term quasi-phase matched refers to matching the electron velocity to the phase velocity of a spatial harmonic. The fundamental laser mode is strictly superluminal, thus quasi-phase matching requires the presence of subluminal spatial harmonics. Due to the drop off in amplitude of spatial harmonics with increasing harmonic number, the first spatial harmonic was chosen as the phase matched mode. The scaling law compared favorably to both laser wakefield acceleration and other direct laser acceleration schemes, predicting energy gains in excess of an order of magnitude higher for actual table top laser parameters.

To validate the scaling law and examine the transverse dynamics, simulations of electron trajectories in presence of the laser's electromagnetic field were conducted. Space charge forces were ignored, and estimates of the validity of this omission were later provided in terms of allowable electron beam densities. Scaling

law validations showed close agreement for an initial electron energy of $g_o = 1000$. A discrepancy in the slope of the energy gain as a function of time was a result of using a Gaussian pulse in the simulations and a flat top pulse when calculating the scaling law. For initial energies of $g_o = 100$, it was shown that allowing the electron to catch up to the spatial harmonic phase velocity yielded higher energy gains than starting the two perfectly phase matched; the electron acceleration resulted in phase slippage with respect to the spatial harmonic. For lower energies, $g_o = 30$, phase slippage occurs rapidly, and graded modulation periods or tapered axial densities are required for acceleration over waveguide limited distances. These results were explained using a simple Hamiltonian model for the longitudinal dynamics.

Two forces were responsible for the transverse dynamics of the electron beam: the quasi-phase matched focusing/defocusing force, and the ponderomotive force due to the fundamental laser mode. The quasi-phase matched force focuses or defocuses based on the electron's phase, whereas the ponderomotive force focuses regardless of phase for small radii. Both forces contained a correction due to the finite spot size of the laser. The quasi-phase matched transverse force is 90° out of phase with the quasi-phase matched axial force; electrons in the maximum accelerating phase only experience a ponderomotive transverse force. As a result, highly accelerated electrons remain collimated in the electron beam, while the remaining electrons are expelled from the beam. A net outward flow of electrons resulted from initially focused electrons slipping into the defocusing phase, and the ponderomotive force causing defocusing at large radii.

3.6 Appendix

3.6.1 Appendix I: Non-Linear and Relativistic Plasma Effects

The assumption of linear plasma response is not always valid in the regime of high intensity lasers where the effect of the ponderomotive force on the background plasma becomes important. We seek to find an estimate of the relative density fluctuations due to the ponderomotive force and show that for the laser intensities considered these fluctuations are small. We start with the equation for the first order motion of the density in the presence of the laser field:

$$\frac{\partial^2 n_1}{\partial t^2} + \mathbf{w}_{p,o}^2 n_1 = \frac{1}{4} n_o c^2 \nabla^2 \langle \hat{a}_r^2 \rangle \quad (78)$$

where $\mathbf{w}_{p,o}$ is the plasma frequency for the background density, the brackets represent an average over the laser frequency, $\hat{a}_r = e\hat{A}_r / m_e c^2$, and only the largest amplitude fundamental laser harmonic is considered. By replacing the Laplacian with its peak value, $4a_o^2 / w_{ch}^2$, which occurs at $r=0$, we obtain an estimate on the magnitude of the density perturbation due to the transverse ponderomotive force:

$$\frac{n_1}{n_o} \sim \frac{1}{4\mathbf{p}^2} a_o^2 \left(\frac{\mathbf{I}_p}{w_{ch}} \right)^2, \quad (79)$$

which for the parameters considered here gives $n_1 / n_o \sim .001$. This ratio seems to justify ignoring the ponderomotive current in Eq. (44). It should be noted that $\partial^2 \langle \hat{a}_r^2 \rangle / \partial z^2 = 0$ at $r=0$, the peak of the Laplacian. However, the density perturbation is excited by the maximum of ∇^2 , wherever it occurs. In addition the

pulse length considered is much longer than the spot size, making the longitudinal contribution to the displaced charge negligible.

By including a correction to Eq. (44) corresponding to a ponderomotive driven modulation of the electron density, but maintaining the slowly varying envelope approximation we can describe Raman side scattering (RSS) of the laser pulse. RSS can cause rapidly growing perturbations in the plasma density and pulse profile which can severely limit the accelerating gradient of the laser electric field. Antonsen and Mora have suggested, however, that the unstable growth due to RSS can be suppressed by utilizing leaky density profiles, allowing for the stable propagation of the lowest radial eigenmode of the plasma channel [42]. The remaining eigenmodes are not confined to the channel and are damped, preventing their growth.

In order to neglect the generation of higher order eigenmodes, we must stipulate that our density profile given in Eq. (45) is meant to model a leaky channel with one well confined quasi-bound mode. In addition, the actual mode profile for the leaky channel must be accurately represented by our solution to Eq. (44). From WKB theory we obtain the condition for modes:

$$\int_{r_{i,\ell}}^{r_{o,\ell}} k_{\perp,\ell} dr = \frac{\mathbf{p}}{2} \left(\ell + \frac{1}{2} \right) \quad (80)$$

where $ck_{\perp,\ell} = [2c^2k_o^2 | \mathbf{d}k_{\ell} | - \langle \mathbf{w}_p^2(r) \rangle_z - 3c^2/4r^2]^{1/2}$ which has roots at the inner and outer classical turning points, $r_{i,\ell}$ and $r_{o,\ell}$ respectively. We note that for different values of ℓ there are different k_{\perp} 's and different turning points. The r^{-2} term in Eq. (44) provides an effective potential that appears in our expression for k_{\perp} and provides

an inner turning point. For one quasi-bound mode we need to ensure that Eq. (80) is only satisfied for $\ell = 0$ by setting the radius where the density profile is a maximum. For our model density profile, we find that

$$\mathbf{d}k_\ell = -k_o \left[\frac{\mathbf{w}_{p,o}^2}{2\mathbf{w}^2} + \frac{4\ell + 2 + \sqrt{3}}{k_o^2 w_{ch}^2} \right], \text{ and} \quad (81)$$

$$r_{o,\ell}^2 = \frac{1}{2} w_{ch}^2 \left[\left(2\ell + 1 + \frac{\sqrt{3}}{2} \right) + \sqrt{\left(2\ell + 1 + \frac{\sqrt{3}}{2} \right)^2 - \frac{3}{4}} \right]. \quad (82)$$

The outer turning point is a monotonically increasing function of ℓ . We can then ensure one quasi-bound mode by choosing the density to be a maximum between $r_{o,0}$ and $r_{o,1}$.

As pointed out in reference [42], extending the maximum density past the outer turning point, $r_{o,0}$, allows for a more confined mode due to k_\perp becoming evanescent. Furthermore, it allows for consistency with our lossless model density profile and boundary condition, $\hat{A}_r(r \rightarrow \infty, z, t) = 0$, via the condition

$$\text{Im} \left[\int_{r_{o,0} + \mathbf{h}}^{\infty} k_\perp dr \right] \gg 1, \quad (83)$$

where the density profile peaks at $r_{o,0} + \mathbf{h} < r_{o,1}$. If $\mathbf{h} = 0$ the integral in Eq. (83) would be strictly real, allowing for outgoing waves, and our model boundary condition would no longer be adequate. Thus our analytic model provides a good representation of a radial density profile of the form:

$$n_e(r) = \begin{cases} n_o + n_o'' r^2 / 2 & 0 < r \leq r_{o,0} + \mathbf{h} \\ n_1(r) & r_{o,0} + \mathbf{h} < r < \infty \end{cases}, \quad (84)$$

where $n_1(r)$ should satisfy Eq. (83) and ensure that $n_e(r)$ is continuous. If we restrict ourselves to modeling radial plasma density profiles shown in Eq. (84), our analytic model provides a good representation of laser propagation, while at the same time stabilizing the effect of RSS. Figure 3.11(a) shows a plasma density profile that is consistent with our requirements including only one quasi-bound mode; figure 3.11(b) shows the corresponding k_{\perp}^2 .

In addition to RSS, we have neglected Raman forward scattering (RFS) by assuming linear non-relativistic plasma response and dropping mixed derivatives in Eq. (44). The growth rate for RFS perturbations to the laser is smaller than the growth rate for RSS by $\sim w_p / w_o$ [72]. However, over propagation distances required for desired interaction lengths in direct electron acceleration, these perturbations may become non-negligible. The pulse lengths required for extending the interaction length in direct acceleration also makes the laser more susceptible to Raman instabilities [72]. To test the effect of RFS on the pulse we conducted simulations of radially polarized laser propagation in a corrugated plasma channel with WAKE [73] for our parameters of interest. Figure 3.10 shows the envelope of the transverse vector potential for the radially polarized laser pulse at different Rayleigh times, where a Rayleigh time is defined as $t_R = \mathbf{p} w_{ch}^2 / I c$ (the waveguide limited time is $20 t_R$). The results show stable propagation over 20 Rayleigh lengths with no fragmentation or distortion of the laser pulse. The stable propagation is consistent with our estimate on the density fluctuations due to the presence of the ponderomotive force. Propagation was also tested in an uncorrugated channel and showed similar behavior; the underlying mechanism allowing for stable propagation

of the radially polarized laser is not an artifact of the corrugated channel. The WAKE simulations and preceding analysis indicate that our assumptions of the plasma response are valid for the parameters and propagation distances considered.

3.6.2 Appendix II: Pulse Power Leakage from Plasma Channel

Our choice of model density profile given by Eq. (45) continues to increase as $r \rightarrow \infty$, providing zero vector potential as $r \rightarrow \infty$. As a result, our model pulse propagates down the length of the plasma channel without any loss due to radially outgoing waves. Actual experimental plasma density profiles peak at some finite radius and decay to zero for large radii (as seen in the density contours of Fig 3.1). Depending on the density profile, the loss of pulse power to outgoing waves may be significant, and the accelerating gradient can be reduced as the pulse propagates. Here we want to examine the loss of pulse power due to more realistic leaky plasma channels like the one shown in Fig 3.11(a) and obtain a condition for which our lossless profile is valid. In the following analysis we will neglect the axial corrugations for mathematical simplicity. The modulations will result in a modulation of the power loss that will average out when integrating over the length of the waveguide.

We start by writing an expression for the differential radial power flow:

$$\frac{1}{r} \frac{dP}{dz} = \frac{c}{2} \text{Re} \left[\vec{E} \times \vec{B}^* \right] \cdot \hat{r}, \quad (85)$$

or equivalently

$$\frac{1}{r} \frac{dP}{dz} = \frac{c}{2} \text{Re} \left[E_z B_q^* \right]. \quad (86)$$

With an expression for \hat{A}_r , and thus A_z using $\nabla \cdot \bar{A} \approx 0$, we can find E_z from $\bar{E} = -\partial \bar{A} / \partial ct$, and B_ϕ from Faraday's law. We proceed by using the WKB approximation for finding an expression for \hat{A}_r outside of the channel. As stated in Appendix I, $ck_{\perp 0} = [2c^2k_o |dk_0| - \langle w_p^2(r) \rangle_z - 3c^2 / 4r^2]^{1/2}$, where dk_0 is given by Eq. (81) with $\ell = 0$. Figure 3.11(b) shows $k_{\perp 0}^2$ for a typical leaky channel and shows schematically how we define our turning points. Our approximate solution for \hat{A}_r outside the channel ($r > R_{o,0}$) is given by

$$\hat{A}_r(r, z, t) = \left(\Theta + \frac{1}{4\Theta} \right)^{-1} \frac{A_o}{\sqrt{k_{\perp}(r)r}} \exp \left[i \int_{R_{o,0}}^r k_{\perp}(r) dr - \frac{(z - v_g t)^2}{\mathbf{s}_z^2} + i \mathbf{d} k z \right], \quad (87)$$

where A_o is the amplitude of the mode at the center of the channel and

$$\Theta = \exp \left[i \int_{r_{o,0}}^{R_{o,0}} k_{\perp}(r) dr \right]. \quad (88)$$

The amplitude outside the channel has fallen by a factor of $\Theta + 1/4\Theta$. As expected, by extending the evanescent region between $r_{o,0}$ and $R_{o,0}$, Θ becomes larger, limiting the amplitude of outgoing waves. Our expression for the differential radial power loss is then

$$\frac{dP}{dz} = -ck_o \left| \Theta + \frac{1}{4\Theta} \right|^{-2} A_o^2 \exp \left[-\frac{2(z - v_g t)^2}{\mathbf{s}_z^2} \right]. \quad (89)$$

The amplitude of the guided mode, A_o , will decay as energy leaks out of the channel; in particular we have that

$$P(z) \approx \frac{c}{16} (k_o w_{ch})^2 A_o^2(z). \quad (90)$$

Inserting Eq. (90) into Eq. (89) gives

$$\frac{1}{P} \frac{dP}{dz} = -\frac{16}{k_o w_{ch}^2} \left| \Theta + \frac{1}{4\Theta} \right|^{-2} \exp \left[-\frac{2(z - v_g t)^2}{\mathbf{s}_z^2} \right]. \quad (91)$$

For simplicity we continue by considering the peak of the pulse and find that

$P = P_o \exp[-z/\mathbf{z}]$, where

$$\mathbf{z} = \frac{k_o w_{ch}}{16} \left| \Theta + \frac{1}{4\Theta} \right|^2 w_{ch}. \quad (92)$$

The leaky channel results in an exponential decay of the guided pulse's power. This decay can be limited by making Θ as large as possible, which is accomplished by using a long flat density profile as shown in Fig 3.11(a). Extending the maximum density to a larger radius would also increase the value of Θ , but allows for higher order quasi-bound modes and may make the guided pulse susceptible to instability as discussed in Appendix I.

3.6.3 Appendix III: Unstable Spot Size Oscillations

We start by considering solutions to Eq. (44) for a background electron density profile of the form

$$n_e(r, z) = n_o [1 + \mathbf{d} \sin(k_m z)] + n_o'' r^2 / 2 [1 + \mathbf{x} \sin(k_m z)], \quad (93)$$

which adds a radial profile modulation to Eq. (45). We write the envelope of the transverse vector potential as

$$\hat{A}_r(r, z, t) = A_o(z - v_g t) \frac{r}{w_{ch}} \mathbf{a}(z) \exp[-\mathbf{b}(z) r^2] \quad (94)$$

where we have used the explicit group velocity approximation explained in the main text, $A_o(z - v_g t)$ determines the pulse shape, $\mathbf{a}(z)$ determines axially dependent phase and amplitude and $\mathbf{b}(z)$ determines the axial dependence of the laser spot size. Upon inserting Eq. (86) into the slowly varying envelope equation we obtain an equation for $\mathbf{b}(z)$:

$$\frac{d\mathbf{b}}{dz} + \frac{2i}{k_o} \mathbf{b}^2 = \frac{i}{4k_o} \left(\frac{w_{p,o}^2}{c^2} \right) [1 + \mathbf{x} \sin(k_m z)]. \quad (95)$$

We expand $\mathbf{b} = \mathbf{b}_o + \mathbf{b}_1 + \dots$, and set the equilibrium value to the matched spot size, $\mathbf{b}_o = 1/w_{ch}^2$. Plugging the expansion into Eq. (87), we find that \mathbf{b}_1 satisfies the equation for a forced harmonic oscillator:

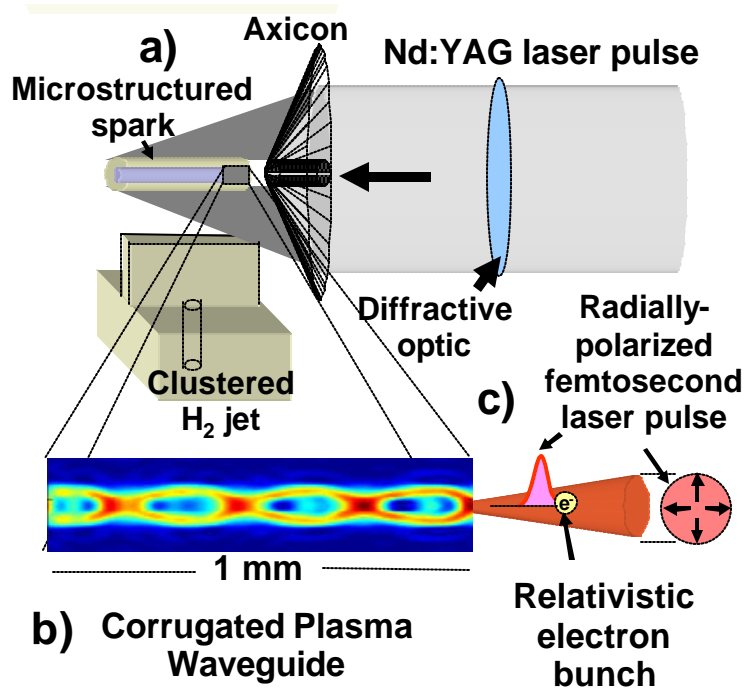
$$\frac{d\mathbf{b}_1}{dz} + 2i\mathbf{k}\mathbf{b}_1 = \frac{1}{2} i\mathbf{x}k_o \mathbf{k}^2 \sin(k_m z), \quad (96)$$

where $\mathbf{k} = 2/k_o w_{ch}^2$. When $k_m = 2\mathbf{k}$, the amplitude of $\mathbf{b}_1(z)$, will undergo secular growth. In the absence of radial profile modulations, the pulse would undergo spot size oscillations if it were not matched to the plasma channel, $\mathbf{b} \neq 1/w_{ch}^2$. The presence of the density modulations drives the oscillations resulting in the secular growth. In particular the solution for $\mathbf{b}_1(z)$ when $k_m = 4/k_o w_{ch}^2$ is

$$\mathbf{b}_1(z) = -\frac{\mathbf{x}}{k_o w_{ch}^4} z \exp[ik_m z]. \quad (97)$$

Unstable spot size oscillations are also possible at higher orders of \mathbf{b} due to harmonics of k_m . In general growth can be expected when $k_m = 4/\ell k_o w_{ch}^2$, where ℓ is an integer. For our parameters, the unstable modulation wavelength is

$l_m = (\mathbf{p} / 2) k_o w_{ch}^2 \sim .3 \text{ cm}$, an order of magnitude higher than the modulation wavelength used. These modulations may be detrimental by spoiling the guiding of a desired mode, or beneficial by spoiling the guiding of an undesired mode.



1. Fig 3.1 Proposed setup for direct acceleration of electrons by a femtosecond laser pulse in a corrugated plasma waveguide. 3.1(a) A radially-modulated Nd:YAG laser pulse focused by an axicon onto a gas jet creates a spark several centimeters long with micron-scale structure. The spark expands into Fig 3.1(b) a plasma waveguide with axial modulations, allowing fine velocity control of guided radiation [15]. Fig 3.1(c) A radially polarized femtosecond laser pulse and a relativistic electron beam are injected into this waveguide.

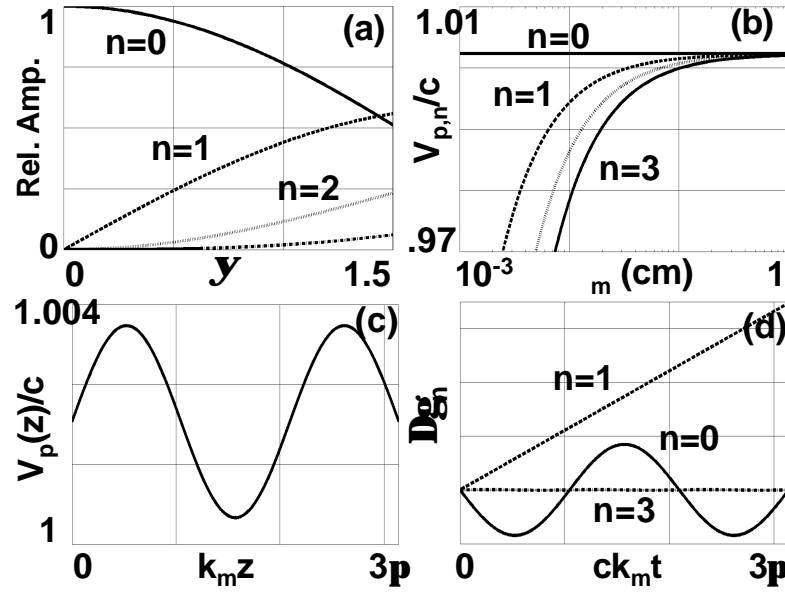


Fig 3.2(a) The relative amplitude of the spatial harmonics as a function of the phase modulation amplitude. Fig 3.2(b) The phase velocity for different spatial harmonics as a function of modulation wavelength. Fig3.2(c) The local laser phase velocity as a function of axial distance. Fig3.2(d) Energy contribution of different spatial harmonics for an electron initially phase matched to the $n = 1$ spatial harmonic.

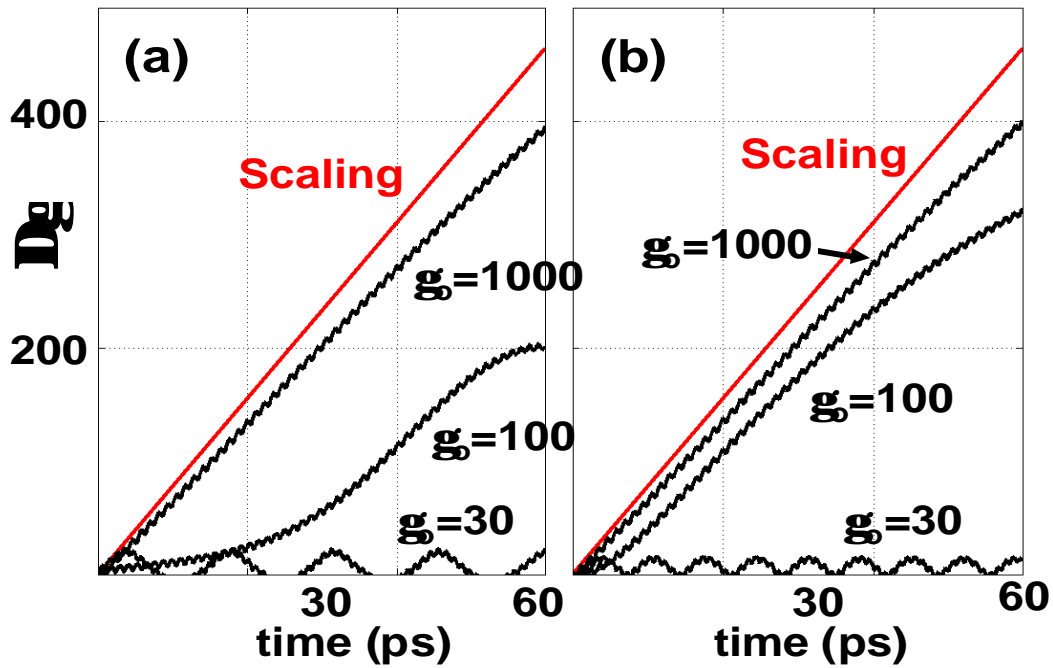


Fig 3.3 Comparison of energy gain predicted by our scaling law with numerical results obtained by integrating the fully relativistic electron equations of motion.

Fig3.3(a) The slow wave phase velocity is matched to the initial electron velocity;

Fig3.3(b) the slow wave velocity is set to c .

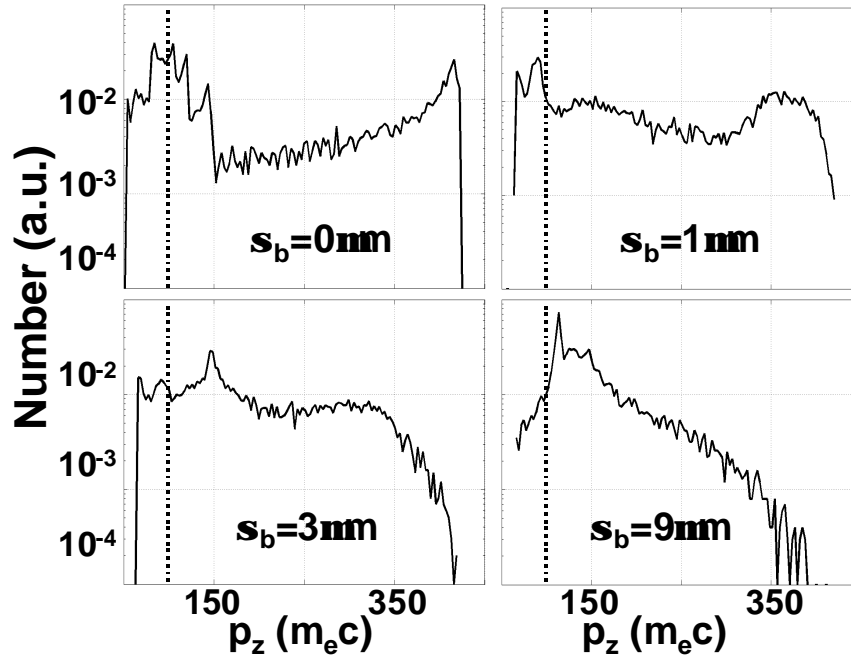


Fig 3.4 Electron axial momentum distributions for different initial electron beam widths after 1.8 cm of propagation (the extent of a physical plasma waveguide).

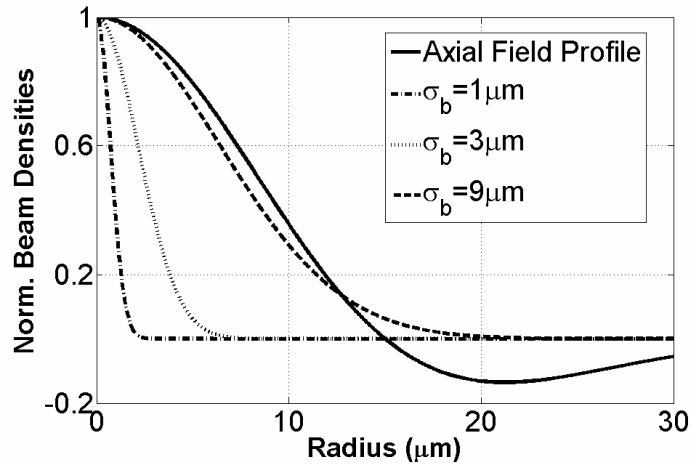


Fig 3.5 Comparison of electron beam Gaussian widths with axial field profile.

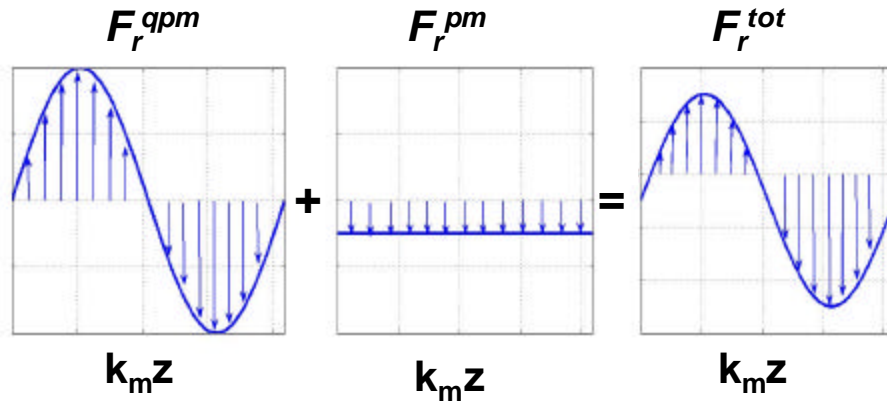


Fig 3.6 Schematic of the transverse forces for small radii as a function of axial distance. The arrows represent the magnitude of the radial force. Because electrons are distributed uniformly in the axial direction, the quasi-phase matched force and ponderomotive force add to provide an overall focusing of the electron beam for small radii.

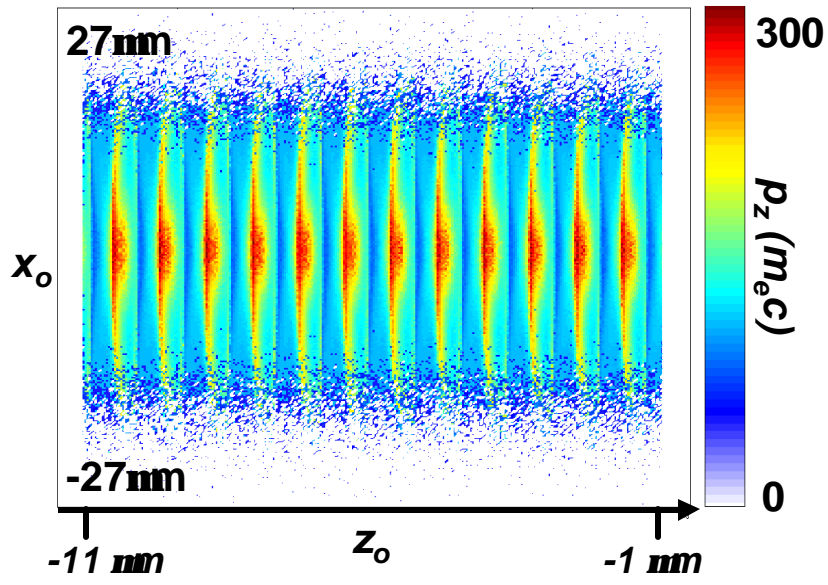


Fig 3.7 Averaged final (after 1.8 cm of propagation) axial momentum (color scale) as a function of initial position (x_o, z_o) .

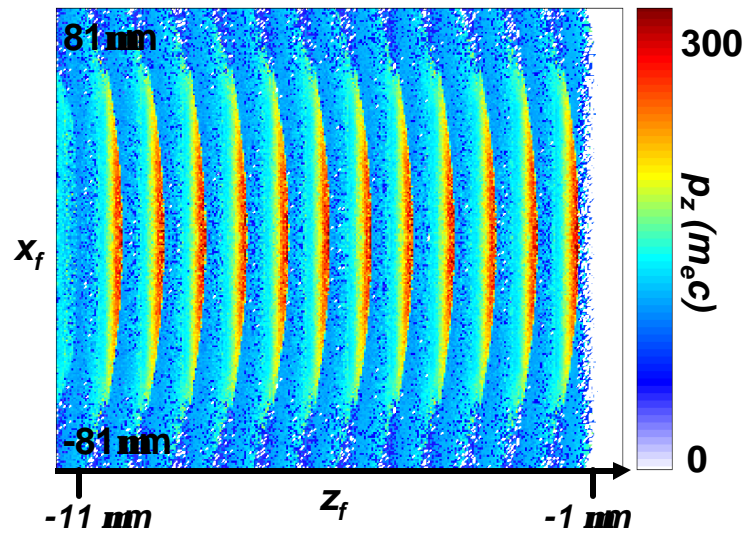


Fig 3.8 Averaged final (after 1.8 cm of propagation) axial momentum (color scale) as a function of final position (z_f, x_f) , (the axial distance traveled by the leading electron has been subtracted out).

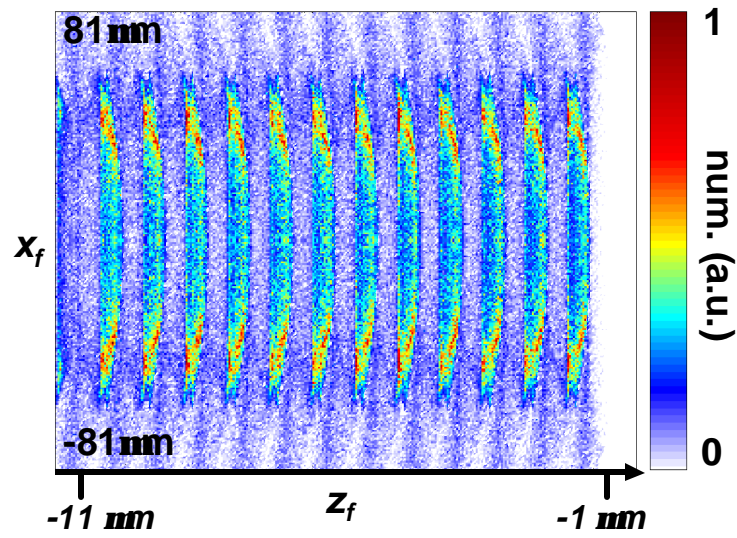


Fig 3.9 Final electron density as a function of final position (z_f, x_f) . The electrons are accelerated into the slow wave fronts resulting in bunching.

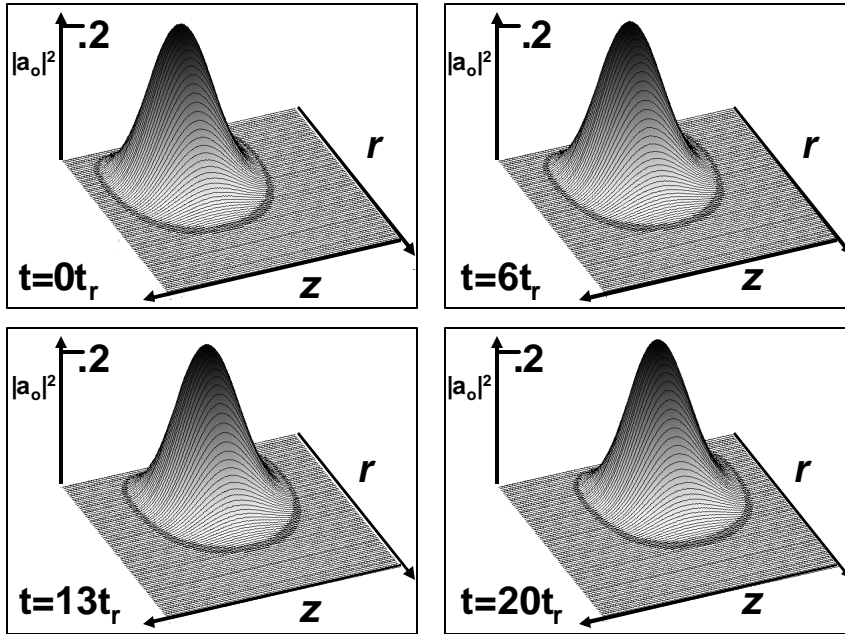


Fig 3.10 The envelope of the transverse vector potential propagating in the axially modulated channel at different times in a frame moving at c . Results were obtained using the WAKE simulation [74].

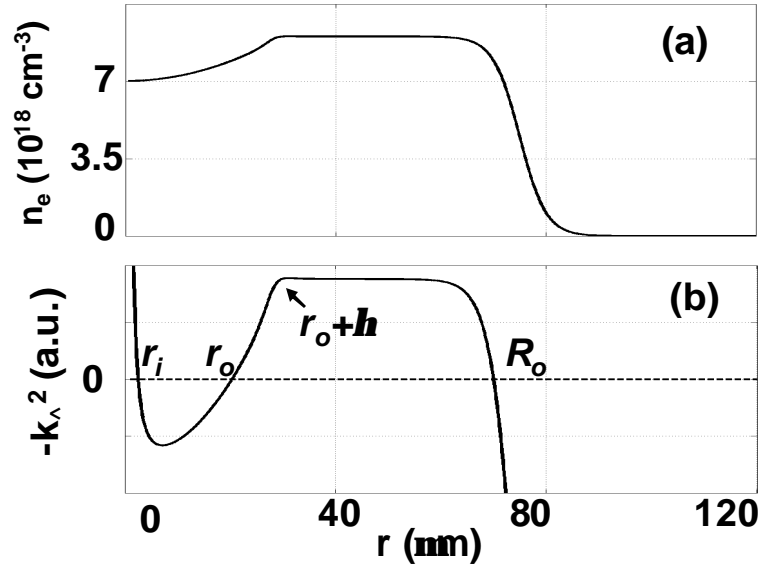


Fig 3.11(a) A sample density profile allowing for one quasi-bound mode and also limiting the loss of pulse power to outgoing waves. Solutions to Eq. (44) for our model density profile in Eq. (45) accurately represent the show density profile. Fig 3.11(b) k_{\perp}^2 corresponding to the density profile shown in Fig 3.11(a).

Summary and Conclusions

We have examined two laser-plasma systems: the laser-cluster interaction and the propagation of lasers in corrugated plasma waveguides as applied to electron acceleration. These systems are fundamentally different in two aspects. The ionized cluster has near solid electron density and thus the plasma frequency is much higher than the laser frequency. Furthermore the size of the cluster is much smaller than the laser wavelength. In corrugated plasma channels, the plasma is tenuous and thus the plasma frequency is much lower than the laser frequency, and the plasma structure extends over the entire extent of the laser. These fundamental differences necessitated two different approaches for modeling the laser-plasma interaction. The two systems are, however, linked in that clusters, apart from having their own applications, provide an ideal medium for the creation of plasma channels.

In the section entitled Dielectric Properties of Laser Exploded Clusters, we developed a fully kinetic, two temperature, linear model for the cluster polarizability in 2D. Determination of the polarizability for an individual cluster provides the dielectric constant for a clustered gas through the relation $\epsilon_{bulk} = 1 + 4\pi n_{cl} \mathbf{g}(\mathbf{w})$, allowing for further studies of laser propagation. Knowledge of the polarizability also provides insight into how the dielectric properties of clusters can best be used for applications.

The Vlasov-Poisson system of equations was solved for the cluster equilibrium, and linearized with respect to the electric field for determining the cluster dipole response. Based on this model, a code was developed to determine the

linear polarizability spectrum of the cluster. The code uses temperatures, ion densities, and boundary electric fields from a PIC simulation for determination of the cluster equilibrium [4]. The cluster responds to the presence of an applied laser electric field through changes in the electron density and electrostatic potential. The response of the electron density provided the cluster polarizability spectrum.

The cluster was shown to have a low frequency dipole response not predicted by cold plasma theory. The response was the result of a beating between electron orbital motion and the applied laser electric field. The amplitude and width of the response is determined by the first order cluster potential and the RMS radius of electrons in the cluster. Additional structure was also observed near the standard cold plasma dielectric resonance at $\omega = \omega_p / \sqrt{2}$. The resonance had a temperature dependent spectral shift: blue shifts due to warm plasma dispersion and red shifts due to an increasingly diffuse density profile at higher temperatures. These effects also caused a temperature dependent width of the resonance.

In Pulse Propagation and Electron Acceleration in Corrugated Plasma Channels an analytic model for laser pulse propagation in the corrugated plasma channel was developed. In addition, simulations were conducted to examine the acceleration and dynamics of relativistic beam electron copropagating with the laser. Direct acceleration of electrons in corrugated plasma waveguides has several advantages over other direct acceleration schemes as well as laser wakefield accelerators. In particular, it provides higher accelerating gradients at lower laser powers.

The slowly varying envelope equation was solved for the vector potential of the guided mode. While retaining the guiding properties of standard plasma channels, the guided mode was also shown to consist of spatial harmonics due to the presence of the plasma corrugations. Under the right conditions, these spatial harmonics can have subluminal phase velocities, allowing for phase matching with copropagating relativistic electrons.

Scaling laws derived with the field solution predicted energy gains in excess of an order of magnitude higher than other laser acceleration schemes. The scaling law was validated with simulations, and a simple Hamiltonian model was presented for explaining the longitudinal dynamics of the electron beam. In particular, it was shown that above a critical energy, allowing the electrons to catch up to the spatial harmonic phase velocity yields higher energy gains than starting the two phase matched.

Two forces were responsible for the transverse dynamics of the electron beam: the quasi-phase matched focusing/defocusing force, and the ponderomotive force due to the fundamental laser mode. For small radii these forces provide an overall focusing of the electron beam. The quasi-phase matched transverse force is 90° out of phase with the quasi-phase matched axial force; electrons in the maximum accelerating phase only experience a ponderomotive transverse force. Simulations demonstrated this effect; the highly accelerated electrons remained collimated towards the center of the electron beam, while low energy electrons were expelled.

Bibliography

- 1 O. F. Hagena and W. Obert, *J. Chem. Phys.* **56**, 1793 (1972).
- 2 T. Ditmire, R. A. Smith, J. W. G. Tisch, and M. H. R. Hutchinson, *Phys. Rev. Lett.* **78**, 3121 (1997).
- 3 A. Gupta, T. M. Antonsen, and H. M. Milchberg, *Phys. Rev. E* **70**, 046410 (2004).
- 4 T. Taguchi, T. M. Antonsen, and H. M. Milchberg, *Phys. Rev. Lett.* **92**, 205003 (2004).
- 5 T. M. Antonsen, T. Taguchi, A. Gupta, J. P. Palastro, and H. M. Milchberg, *Phys. Plasmas* **12**, 056703 (2005).
- 6 A. Gupta, T. M. Antonsen, T. Taguchi, and J. P. Palastro, *Phys. Rev. E* **74**, 046408 (2006).
- 7 J.P. Palastro, T.M. Antonsen, A. Gupta, *Phys. Plasmas* **14**, 033105 (2007).
- 8 V. Kumarappan, K. Y. Kim, and H. M. Milchberg, *Phys. Rev. Lett.* **94**, 205004 (2005).
- 9 J. Wu and T.M. Antonsen, *Physics of Plasmas* **10**, 2254, (2003).
- 10 H. Sheng, K.Y. Kim, V. Kumarappan, B.D. Layer, and H.M. Milchberg, *Phys. Rev. E* **72**, 036411 (2005)
- 11 C.G. Durfee III and H.M. Milchberg, *Phys. Rev. Lett.* **71**, 2409 (1993).
- 12 T.R. Clark and H.M. Milchberg, *Phys. Rev. Lett.* **78**, 2373 (1997).
- 13 T.R. Clark and H.M. Milchberg, *Phys. Rev. E* **61**, 1954 (2000).
- 14 T.R. Clark and H.M. Milchberg, *Phys. Rev. E* **57**, 3417 (1998).
- 15 B.D. Layer, A. York, T.M. Antonsen, S.Varma, Y.-H. Chen, Y. Leng, and H. M. Milchberg, *Phys. Rev. Lett.* **99**, 035001 (2007).
- 16 K. Y. Kim, I. Alexeev, V. Kumarappan, E. Parra, T. Antonsen, T. Taguchi, A. Gupta and H. M. Milchberg *Phys. Plasmas* **11**, 2882 (2004).
- 17 T. D. Donnelly, T. Ditmire, K. Neuman, M. D. Perry, and R. W. Falcone, *Phys. Rev. Lett.* **76**, 2472 (1996).
- 18 B. Shim, G. Hays, R. Zgadzaj, T. Ditmire, and M. Downer, *Bull. Am. Phys. Soc.* **51**, 229, (2006).
- 19 M.B. Smirnov and W. Becker, *Phys. Rev. A* **69**, 013201 (2004).
- 20 M.B. Smirnov and W. Becker, *Phys. Rev. A* **74**, 013201 (2006).
- 21 NRL Plasma Formulary, J.D. Huba, (2002).
- 22 J. Zweiback, R. A. Smith, T. E. Cowan, G. Hays, K. B. Wharton, V. P. Yanovsky, and T. Ditmire, *Phys. Rev. Lett.* **84**, 2634 (200).
- 23 J. Zweiback, T. E. Cowan, J. H. Hartley, R. Howell, K. B. Wharton, J. K. Crane, V. P. Yanovsky, G. Hays, R. A. Smith, and T. Ditmire, *Phys. Plasmas* **9**, 3108 (2002).
- 24 K. Ishikawa and T. Blenski, *Phys. Rev. A* **62**, 063204 (2000).
- 25 M. Eloy, R. Azambuja, J. T. Mendonca, and R. Bingham, *Physica Scripta* **T89**, 60 (2001).
- 26 K. Kim, I. Alexeev, T. M. Antonsen, A. Gupta, V. Kumarappan, and H. M. Milchberg *Phys. Rev. A* **71**, 011201 (2005).
- 27 I. Alexeev, T. M. Antonsen, K. Y. Kim, and H. M. Milchberg *Phys. Rev. Lett.* **90**, 103402 (2003).

- 28 T. Ditmire, R. A. Smith, R. S. Marjoribanks, G. Kulcsar, and M. H. R. Hutchinson, *Appl. Phys. Lett.* **71**, 166 (1997).
- 29 K.W. Madison, P.K. Patel, M. Allen, D. Price, R. Fitzpatrick, and T. Ditmire, *Phys. Rev. A* **70**, 053201 (2004).
- 30 T. Ditmire, J. Zweiback, V.P. Yanovsky *et al.*, *Nature (London)* **398**, 489 (1999).
- 31 P. Sprangle, B. Hafizi, J. R. Peñano, R. F. Hubbard, A. Ting, A. Zigler, and T. M. Antonsen, *Phys. Rev. Lett.* **85**, 5110 (2000).
- 32 G. Shvets and N. J. Fisch, *Phys. Rev. E*, **55** 6297 (1997).
- 33 N. Barov, J. B. Rosenzweig, M. E. Conde, W. Gai, and J. G. Power, *Phys. Rev. ST Accel Beams* **3**, 011301 (2000).
- 34 S.P.D Mangles *et al.* *Nature* **431** 535-538 (2004).
- 35 C.G.R Geddes *et al.* *Nature* **431** 538-541 (2004).
- 36 J. Faure *et al.* *Nature* **431** 541-544 (2004).
- 37 H. M. Milchberg, T.R. Clark, C.G. Durfee III, T.M. Antonsen Jr., and P. Mora, *Phys. Plasmas* **3**, 2149 (1996).
- 38 T.M. Antonsen Jr., J.P. Palastro, and H.M. Milchberg, *Phys. Plasmas* **14** 033107 (2007).
- 39 R. E. Denton and M. Kotschenreuther, *J. Comp. Phys.* **119**, 283 (1995).
- 40 P. Serafim, P. Sprangle, and B. Hafizi, *IEEE Trans. Plasma Sci* **28**, 1190 (2000).
- 41 M.D. Feit and D.E. Maiden, *App. Phys. Lett.* **28**, 331 (1976).
- 42 T.M. Antonsen Jr. and P. Mora, *Phys. Rev. Lett.* **74**, 4440 (1995).
- 43 T. Tajima and J. M. Dawson, *Phys. Rev. Lett.* **43**, 267 (1979).
- 44 T. Plettner, R. L. Byer, E. Colby, B. Cowan, C. M. S. Sears, J. E. Spencer, and R. H. Siemann, *Phys. Rev. ST Accel. Beams* **8**, 121301 (2005).
- 45 Eric Esarey, Phillip Sprangle, and Jonathan Krall, *Phys. Rev. E* **52**, 5443 (1995).
- 46 E. Parra, I. Alexeev, J. Fan, K. Kim, S. J. McNaught, and H. M. Milchberg, *Phys. Rev. E* **62**, R5931 (2000).
- 47 T. Ditmire, T. Donnelly, R. W. Falcone, and M. D. Perry, *Phys. Rev. Lett.* **75**, 3122 (1995).
- 48 T. Ditmire, T. Donnelly, A. M. Rubenchik, R. W. Falcone, and M. D. Perry, *Phys. Rev. A* **53**, 3379 (1996).
- 49 J. D. Jackson, *Classical Electrodynamics* (John Wiley & Sons, Inc., New York, (1962) 113.
- 50 M. V. Fomyts'kyi, B. N. Breizman, A. V. Arefiev, and C. Chiu, *Phys. Plasmas* **11**, 3349 (2004).
- 51 T. Tajima, Y. Kishimoto, and M. C. Downer, *Phys. Plasmas* **6**, 3759 (1999).
- 52 H. M. Milchberg, S. J. McNaught, and E. Parra, *Phys. Rev. E* **64**, 056402 (2001).
- 53 F. Brunel, *Phys. Rev. Lett.* **59**, 52 (1987).
- 54 H. Goldstein, C. Poole, and J. Safko, *Classical Mechanics*, (Addison Wesley, New York, 2002) 70.
- 55 H.M. Milchberg, C.G. Durfee III, and T.J. McIlarth, *Phys. Rev. Lett.* **75**, 2494 (1995).
- 56 T. Tajima and J. M. Dawson, *Phys. Rev. Lett.* **43**, 267 (1979).
- 57 E. Esarey, P. Sprangle, J. Krall, A. Ting, and G. Joyce, *Phys. Fluids B* **5**, 2690 (1993).
- 58 T. C. Chiou, T. Katsouleas, C. Decker, W. B. Mori, J. S. Wurtele, G. Shvets, and

- J. J. Su, Phys. Plasmas **2**, 310 (1995)
- 59 P. Sprangle, E. Esarey, J. Krall, and G. Joyce, Phys. Rev. Lett. **69**, 2200 (1992).
- 60 T. Katsouleas, Nature **431**, 515 (2004).
- 61 J.D. Lawson, IEEE Trans. Nucl. Sci. **NS-26**, 4217 (1979); P.M. Woodward, J. IEE **93**, 1554 (1947).
- 62 P. Sprangle, E. Esarey, and J. Krall, Phys. Plasmas **3**, 2183 (1996).
- 63 W. D. Kimura, G. H. Kim, R. D. Romea, L. C. Steinhauer, I. V. Pogorelsky, K. P. Kusche, R. C. Fernow, X. Wang, and Y. Liu, Phys. Rev. Lett. **74**, 546 (1995).
- 64 T. Plettner, R.L. Byer, E.Colby, B.Cowan, C. M. Sears, J. E. Spencer, and R. H. Siemann, Phys. Rev. Lett. **95**, 134801 (2005).
- 65 E. Esarey, P. Sprangle, and J. Krall, Phys. Rev. E **52** 5443, (1995).
- 66 B. Hafizi, A. Ting, E. Esarey, P. Sprangle, and J. Krall, Phys. Rev. E **55**, 5924 (1997).
- 67 V. Malka, S. Fritzler, E. Lefebvre, M.-M. Aeonard, F. Burgy, J.-P. Chambaret, J.-F. Chemin, K. Krushelnick, G. Malka, S. P. D. Mangles, Z. Najmudin, M. Pittman, J.-P. Rousseau, J.-N. Scheurer, B. Walton, and A. E. Dangor., Science **298**, 1596 (2002).
- 68 A. York, B.D. Layer, and H.M. Milchberg, in *Advanced Accelerator Concepts*, AIP Conf. Proc. **877**, 807 (2006).
- 69 M. Xie, LBNL-48236, "Plasma inverse transition acceleration", (2001).
- 70 Richard F. Hubbard, Phillip Sprangle, and Bahman Hafizi, IEEE Transactions on Plasma Science **28**, 1159 (2000).
- 71 www.glue.umd.edu/~palastro/scatter.mpg
- 72 T.M. Antonsen Jr and P. Mora, Phys. Fluids B **5**, 1440 (1993).
- 73 P. Mora and T.M. Antonsen Jr., Phys. Plasmas **4**, 217 (1997).